Nano-Processing with Gas Cluster Ion Beams

Noriaki Toyoda

February 1999

Abstract

In this thesis, fundamental properties of gas cluster ion beams and their non-linear irradiation effects are studied. Applications in the fabrication of nano-structures (nano-processes) are demonstrated, as based on knowledge of the interactions between clusters and solid surfaces.

In chapter 2, a cluster source which provides an intense neutral cluster beam by supersonic expansion from a Laval nozzle is described, and the high current cluster ion beam equipment is explained. By optimization of both ionization and transport conditions of the cluster beam, a high cluster ion current density of a few μA/cm^2 was achieved.

The detailed cluster size distribution following a supersonic expansion and the characteristics of the cluster beams are discussed in chapter 3 based on data obtained with a high resolution time of flight mass spectrometer. The formation of inert, reactive and complex gas clusters was verified, and their average cluster size was 2000atoms/cluster. With increasing cluster size, the ionization and collision cross-section increased, however, the kinetic energy of the impact was compensated by the cohesive energy of a large cluster.

In chapter 4, interactions of cluster and target atoms in an energetic cluster ion impact are discussed. Most of the kinetic energy of cluster ions was deposited with high density on the surface regions of the targets, and subsequently, multiple collisions between targets and clusters occurred. This dense energy deposition resulted in intrinsic non-linear sputtering effects, such as high yield sputtering and crater formation, which could not be explained by the summation of the irradiation effects induced by the same number of monomer ions. The lateral sputtering effect, which is explained in that many sputtered atoms with cluster ions are emitted in the horizontal direction on the surface plane, was clarified experimentally for the first time, and this was verified by STM observations of single traces of cluster ion impacts.

In chapter 5, an enhancement of the sputtering effects with reactive

cluster ion beams and their applications are discussed. Since the impact area of the target by a cluster ion occurred under high temperature and high pressure conditions, chemical reactions on the target surface were enhanced. In the case of reactive cluster ion irradiation, dissociation of reactive molecules and clusters occurred simultaneously, and subsequently, enhancement of the etching rate was observed as a consequence of the production of volatile materials. Reactive cluster ion etching could be applied for Si fine pattern etching, and it provided solutions for charging up, isotropic etching, microloading and radiation damage problems.

In chapter 6, the surface smoothing effect and mechanisms with cluster ions are discussed. The cluster ion exhibited marked surface smoothing effects and it was made clear from both experimental and simulation results that the lateral sputtering effect was significant for surface smoothing. Very smooth surfaces of CVD diamond films and SiC single crystal substrates were obtained using the gas cluster ion beam processing; these materials are difficult to etch using conventional processes.

From these results, it can be summarized that gas cluster ion beam processing is effective in the fabrication of nano-structures and applications in the industrial field are expected.

Acknowledgments

The author would like to express his deep gratitude to Professor Isao Yamada of Kyoto University for his continuous guidance and encouragement throughout this study. The author also would like to thank Professor Kunihide Tachibana and Professor Nobutsugu Imanishi of Kyoto University for their comments, advice and helpful discussions on the manuscript.

The author is very grateful to Assistant Professor Gikan Takaoka for many helpful comments. He also would like to express deep gratitude to Research Associate Jiro Matsuo for significant discussions and experimental advices. He is also grateful to Visiting Professor Zinetulla Insepov for stimulating discussion and comments in this study.

This research was made possible by the many cooperation and assistance of many students and research fellows at Kyoto University. The author would like to thank Dr. Daisuke Takeuchi and Dr. Makoto Akizuki for kind discussions and encouragement. He also would like to thank to Mr. Takaaki Aoki and Mr. Toshio Seki for their contributions and discussions in this study.

The assistance of Mr. Hiroaki Kitani, Mr. Norihisa Hagiwara and Mr. Masahiro Saito made this study possible and the author would like to thank them for their quite valuable contributions. He is also thankful to all the members of the Ion Beam Engineering Laboratory at Kyoto University during his doctoral course studies.

The author wishes to thank to Professor Wei Kan Chu of University of Houston and Mr. Akio Nishiyama of Mitsubishi Material Co. for their helpful discussions and supply of YBCO and CVD diamond films. He is also grateful for the helpful supports of all the member of Epion Co. at Massachusetts for the development of the cluster ion beam equipment.

The Rutherford backscattering measurements were carried out with great help of the department of nuclear engineering at Kyoto University. The author would like to thank Research Associate Kouji Yoshida for

the operation of the accelerator.

Finally, he especially thanks his parents for their continuous care, support and encouragement.

Contents

Chapter 1

Introduction

1.1 What is a Cluster?

Cluster

In the time of ancient Greece, the concept of an 'element' had already arisen, and the systematic atomic theories were constructed in the 18th century by Boyle, Dalton, Lavoisier, Avogadro et al. From that time on, there have been two streams of study about 'How does a matter behave?'. One stream is concerned with the properties of the individual atoms or molecules. This has led to the nuclear physics and particle physics beginning in the early 20th century. The other stream is the study of bulk materials containing enormous numbers of atoms.

Here arises the question, where does the property of matter change from the bulk to individual atoms? Is there an additional phase between the bulk and individual atoms? To answer these questions, the study of the clusters with a size of a few to several thousands atoms was begun from the 1970's. The significant differences of the cluster from the bulk arise from quantum size effects. Clusters are aggregates of atoms a few nm in diameter so that the quantum states and the band structure of clusters become different from those of the bulk. For example, the visible light emission from porous Si and Si nanoclusters in SiO_2 have been reported[1)], although the band structure of bulk Si is indirect transition and the band gap is 1.1eV, which is equivalent to infrared light. The wavelength and the intensity are expected to be changed by the cluster size, and enthusiastic study of nanoclusters has been carried out for optical and magnetic devices.

Further, the discovery of the Buckminster fullerene (C_{60}) by Kroto and Smally[2] created a sensation and has attracted much interest from various fields. They were awarded the Nobel Prize for physics in 1996. The molecular C_{60} is a new state of carbon in addition to the ordinary states of diamond, graphite and amorphous material. The study of C_{60} advanced suddenly in 1990's because the method of the mass synthesis of C_{60} was discovered by Kraetschmer and Huffman[3]. As well as C_{60}, carbon nanotube[4], carbon onion[5] and the metal doped C_{60}[6] have been proposed.

As well as the physical and chemical properties of the cluster itself, the impact process of an energetic cluster ion is very attractive[7]. Since the thousands of atoms impact the target at almost precisely the same time, multiple collisions between target and cluster atoms induced by dense energy deposition become significant.

Impact Process of an Energetic Cluster

The initial concept of the impact process of an object was presented by Galileo and Newton[8, 9]. This classical theory is adequate for the collisions of a macroscopic object with a large rigid mass. However, in the case of high velocity impact processes, both the deformations at the contact point and the energy conversion to internal degrees of freedom cannot be neglected. With an impact velocity in excess of the hypervelocity region of more than a few km/s, fusion or vaporization of both target and projectile materials takes place with crater or hole formation. For example, Fig.1.1(a) shows a photograph of the meteor crater in northern Arizona[10]. This crater has a diameter of 1.2km and was generated by a metallic meteor about 30m in diameter some 50,000 years ago. It deposited an enormous amount of energy on the earth and the impact region experienced high temperature and high pressure. The energy transfer process under these circumstances can be interpreted with the aid of a hydrodynamic model[11].

From the microscopic point of view, similar crater formation has been reported using a high energy heavy atom[12] and cluster ions[13]. Fig.1.1(b) shows a single crater image of 150keV Ar_{3000} cluster impact on a gold surface observed with a Scanning Tunneling Microscope (STM)[14]. A crater 30nm in diameter is clearly observed, which is 2.5×10^{-11} times smaller than the meteor crater. The motion of the atoms induced by a cluster impact can be estimated using molecular dynamics simulations

which indicate that the impacted region is subjected to transient temperatures and pressures of both ten thousands of degrees and tens of GPa[15]. As the impinging energy of a heavy atom or a cluster is deposited in a local area, a crater and shockwave are generated. These phenomena are not observed in the monomer ion impact which can be well described by binary collisions. Therefore, distinctive irradiation effects with cluster ions are expected, and industrial applications which utilize the cluster ions are being investigated.

1.2 Nano-Processing with Gas Cluster Ion Beams

Problems of Nano-processing

With the progress of electronic devices to below submicron level ($<$ 100nm), the fabrication process of fine structure becomes more important. In addition to the electronic devices, optical and magnetic devices or sensors and mechanical devices mounted on IC chips also require such a nano-scale fabrication. The fabrication process of the nano-structure is termed 'nano-technology'. The ion beam process is one of the basic technologies in nano-structure fabrications such as etching or implantation of impurities, and a low energy ion beam process is required to be compatible with the shrinking device scale.

However, it is difficult in principle to attain both low energy and high ion current with an atomic ion beam because of dispersion by the space charge effects. To avoid the space charge effect, the acceleration-deceleration technique which extracts an ion with high energy at the beginning and decelerates it in front of the target is proposed. Even with this process, neutralized particles with high energy cause damage, which is termed 'energy contamination'.

In the Reactive Ion Etching (RIE) process which uses plasma as a source, there are the following problems; damage formation caused by high energy particles in the plasma, and the breakdown of the device by charging up. Thus, development of the low energy and low charge ion beam process is required.

In addition, surface polishing at an atomic level is required to fabricate a nano-structure, and Chemical Mechanical Polishing (CMP) is applied for this purpose. However, the surface smoothing with CMP is

(a) The meteor crater at northern Arizona[10].
(1.2km in diameter)

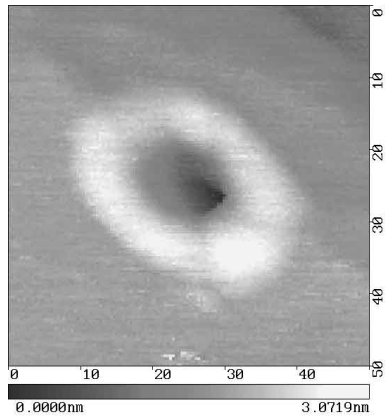

(b) STM images of a crater on Au with Ar cluster ion impact[14].
(30nm in diameter, 150keV Ar_{3000} cluster ion)

Figure 1.1: Macroscopic and microscopic view of craters

difficult for samples which have fine patterns, 3-dimensional structure and a weak mechanical strength, such as thin films, because the CMP process uses a large polisher which contacts directly on the target surface. Also, since the CMP is a wet process, the control of the polishing condition on the surface is difficult compared with a dry process. Thus, ion beam polishing with oblique incidence has been proposed, but the problems of the radiation damage to the target and ripple formation on the surface are not resolved yet.

The gas cluster ion beam process has been developed by Yamada and co-workers at Kyoto University[16, 17, 18] to give solutions to these problems which are facing conventional ion beam processing. As the impact processes are completely different from those of atomic (monomer) ions, cluster ions provide a new surface processing technique which cannot be obtained with any conventional method.

Characteristics of the Cluster Ion Beam Process

A cluster is an aggregate of a few to several thousands of atoms, and it can be accelerated to a desired energy after ionization so that it has intrinsic characteristics compared with monomer ion beams. Since the number of charges in the cluster is much smaller than the number of atoms, a cluster ion can transport thousands of times larger numbers of atoms at the same ion current compared with a monomer ion. For example, if the cluster ion current with cluster size of 1000 is 1μA, it can transport the same number of atoms as a 1mA monomer ion beam.

Another feature of the cluster ion beam is a low-energy irradiation. Since the kinetic energy of the atom in the cluster is equal to the total energy divided by the cluster size, a cluster with 2000 atoms, accelerated up to 20keV carries an energy per atom of only 10eV. Although it is difficult to obtain 10eV monomer ion beams due to the space charge effect, equivalently low energy ion beams can be realized by using cluster ion beams at relatively high acceleration voltages.

Not only the low charge and low energy feature but also the dense energy depositions at a local area are important characteristics in the irradiation by cluster ions. The diameter of a cluster with a cluster size of several thousands is only a few nanometers so that thousands of atoms penetrate the target in an area only a few nanometers in diameter which causes multiple collisions between target and cluster atoms. Therefore, all of the impinging energy of a cluster ion is deposited at the surface

region, and this dense energy deposition is the origin of enhanced sputtering yields, crater formation, shockwave generation and other non-linear effects.

This laboratory has been carrying out the study of the cluster ion beam process for a decade, and has revealed that the cluster ion beam has very valuable properties such as low energy implantation[19], high yield sputtering[20], surface smoothing[21] and thin film formation[22] at low temperatures. Specifically, shallow junction formation with $B_{10}H_{14}$ polyatomic clusters was successfully demonstrated in the fabrication of a PMOS device with a gate length of 0.04μm[23].

As to the sputtering phenomena with cluster ions, it is predicted from molecular dynamics simulations that large numbers of atoms will be sputtered into horizontal directions after a cluster ion impact, and this is termed 'lateral sputtering'[24]. This sputtering effect is assumed to give a surface smoothing effect, and application for fabrication of nanostructures is expected. However, there is no experimental confirmation for the surface smoothing effect with cluster ions and the impact process is still in the 'blackbox'. In order to propose the cluster ion beam process for a practical application, adequate information about the interaction between cluster and target atoms is necessary.

1.3 Purpose of the Study

This thesis aims to reveal the fundamental properties of gas cluster ion beams and the interactions between clusters and target atoms. Applications of the gas cluster ion beam process in the industrial field are also proposed based on the knowledge of these impact processes.

In chapter 2, cluster beam formation from a supersonic nozzle is introduced and development of high current cluster ion beam equipment is discussed. Several mass spectrometers used to measure masses of huge clusters are introduced.

In chapter 3, properties of gas cluster beams are discussed based on the precise cluster size distributions measured with high resolution time of flight mass spectrometer. In addition to the inert cluster ions, formations of reactive and complex gas clusters are discussed. Fragmentation and multiply charged ionization of clusters are also studied.

In chapter 4, sputtering phenomena with Ar cluster ions are investigated in terms of the sputtering yield, single track of the impact and the

angular distribution of the sputtered particles. The lateral sputtering effect which is intrinsic to cluster ions is discussed here.

In chapter 5, enhancement of chemical reactions using reactive cluster ions is discussed. Chemical products and their angular distributions as a consequence of the chemical reactions with reactive cluster ions are discussed. Also, etching of a Si fine pattern with the reactive cluster ions is performed, and application of reactive cluster ion etching is proposed.

In chapter 6, the surface smoothing effect and mechanisms with cluster ions are discussed. The surface smoothing effect is modeled and simulated numerically. Applications of surface smoothing with cluster ions are demonstrated on various materials, and utilizations of the cluster ion beams as nano-processing tools are discussed.

Finally, the results of this study are summarized in chapter 7.

Chapter 2

Cluster Beam Formation and Equipment

2.1 Neutral Cluster Source

2.1.1 Supersonic Expansion

Cluster Source

A Knudsen cell is generally used to obtain a molecular beam. A solid or liquid is heated sufficiently low so that the mean free path of the evaporated particles is larger than the diameter of the hole through which the particles effuse. The hole is so small that it does not perturb the thermodynamic equilibrium between the gaseous and condensed phases in the cell. Therefore, only a small number of clusters is contained in the beam, and the beam intensity is usually too low for practical experimental use. Today, intense cluster sources have been developed and they are categorized into following types.

- *Supersonic Expansion :*
  A gas is allowed to expand from a high pressure into a vacuum chamber through a small hole. This adiabatic expansion reduces the relative velocity of the gas atoms and clusters are formed. Clusters of gaseous elements and compounds with high vapor pressure are generated with this source. Since a cryogenic beam that is less than 10K is easily realized, van der Waals clusters with low binding forces can be generated.

- *Laser ablation :*
  This type of cluster source was developed by Smalley and co-workers[25], and it is applicable for the formation of clusters from any solid materials. The target metal or compound is irradiated by an intense laser beam, resulting in the emission of a high temperature plasma[26, 27] which contains atoms, ions, electrons and bunches of atoms from the surface. By cooling with He gas, metallic vapor condenses and clusters of various sizes are formed.

- *Sputter Source :*
  A dense cluster can be generated with a laser ablation source. However, the amount of clusters is relatively low. For thin film formation with clusters, the laser pulse is replaced by a sputtering source with heavy ions. Xe ions with energies of 10 to 30keV are mainly used as primary ions.

- *Discharge Source :*
  Electrons are injected near the nozzle. An ionized particle acts as a condensation nucleus and, as a result, the ionized cluster grows.

- *Gas Aggregation :*
  Atoms or molecules are injected into a stagnation gas chamber, and their velocity is slowed down by the collisions with inert gas clouds. Clusters are generated by this cooling effect[28].

Among these cluster sources, the supersonic expansion makes it possible to obtain a cryogenic beam with a large amount of clusters[29, 30]. Although it is difficult to apply to solid materials, supersonic expansion is the best cluster source for gaseous materials. In this study, supersonic expansion from a nozzle is used as a cluster source except for carbon clusters.

Supersonic Jet

Fig. 2.1 shows a schematic of the supersonic expansion from a nozzle. A gas is allowed to expand from a stagnation region in a high pressure (P_0) into a vacuum through a small orifice of diameter D. The random velocity in the stagnation region is nearly cancelled out by the adiabatic expansion, which means that all the atoms are moving at nearly same speed. Thus, a low translational temperature is realized.

The enthalpy in the stagnation region (H_0) is converted into kinetic energy of the directed mass flow and a rest enthalpy (H). The conservation law of energy gives[31]:

$$H_0 = H + \frac{1}{2}mv^2 = c_pT + \frac{1}{2}mv^2 = c_pT_0 \tag{2.1}$$

where c_p is the specific heat at constant pressure which is $\frac{5}{2}k$ for an atomic beam, T_0 and T are the temperatures before and after expansion, respectively. As the Boltzmann constant $k = c_p - c_v$, where c_v is the specific heat at constant volume, Eq. 2.1 can be rearranged as follows.

$$T = T_0 \left[1 + \frac{1}{2}(\gamma - 1)M^2\right]^{-1} \tag{2.2}$$

where M is a Mach number defined as the ratio of stream velocity v to the local sound speed $c = \sqrt{\gamma kT/m}$. The ratio of specific heat $\gamma = c_p/c_v$ at constant temperature and volume is independent of the temperature. The Mach number M increases along the downstream of the beam, and it is described as[32]:

$$M = A\left(\frac{x}{D}\right)^{\gamma-1} \tag{2.3}$$

where A is 3.26 in the case of an atomic beam[32] and x is a position from the nozzle. For example, T is less than 1K at x=30mm with the orifice diameter of 0.1mm at room temperature. At the point where the hydrodynamic flow condition is no longer satisfied, there is a terminal velocity. In general, it is about a few degrees K.

Cluster Formation

If the local temperature is less than the binding energy of the dimer, cluster formation can be stabilized by a 3-body collision expressed as[33]:

$$\mathrm{Ar} + \mathrm{Ar} + \mathrm{Ar} \rightarrow \mathrm{Ar} + \mathrm{Ar}_2 \tag{2.4}$$

To keep the energy conservation law, the kinetic energy of the monomer on the right hand side of Eq. 2.4 is higher than that of the left hand side ones. Once dimers are formed, they act as condensation nuclei for cluster growth. If the ratio of atoms to clusters is large, a cluster grows by monomer additions. If the number of clusters is high, cluster-cluster aggregation becomes dominant. This cluster formation occurs in the

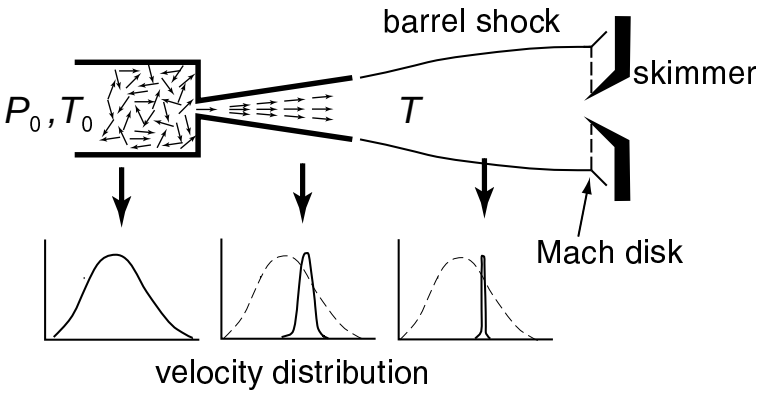

Figure 2.1: Schematic of the supersonic expansion and the velocity distribution of the particles.

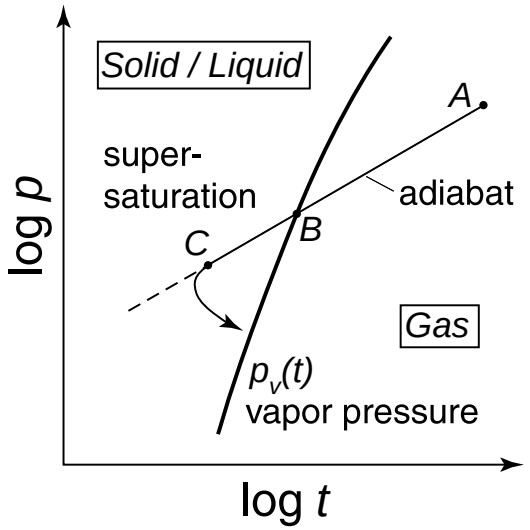

Figure 2.2: Phase diagram under supersaturation.

transition region from hydrodynamic flow to molecular flow, and no collision occurs in the molecular flow region. Thus, an intense cluster beam can be obtained by extracting it in the molecular flow region.

Cluster formation can be treated as a gas-fluid phase transition. Fig.2.2 gives a schematic phase diagram of the gas flow in the expansion. The point A represents the stagnation condition. During the expansion, the expanding gas follows the adiabatic line up to the point B, where it meets the vapor pressure curve $p_v(t)$.

In the thermal equilibrium condition, the subsequent expansion proceeds along the $p_v(t)$ curve where gaseous and solid/liquid states coexist. However, this equilibrium expansion is not observed for the nozzle expansion, instead, the expansion continues along the adiabatic line. The gas state in this region is not stable, and is termed supersaturated. Soon the expanding gas departs from the adiabatic line at point C and tends to approach the vapor pressure curve $p_v(t)$. This transition from the supersaturated state is initiated by the formation and growth of clusters.

A small particle or cluster of radius r has a larger vapor pressure P_r compared with that of a plane surface P_0[33]:

$$\ln \frac{P_r}{P_0} = \frac{2\sigma m}{kT\rho}\frac{1}{r} \tag{2.5}$$

where σ and ρ are the surface tension of small particle and the density, respectively. With the increase of r, the vapor pressure decreases. A cluster having larger radius than critical value r^* grows while a smaller one evaporates. Therefore, there are two peaks in the mass spectrum of the cluster beam; one is the exponential decay distribution of small clusters and the other is wide distribution at large cluster size region. Details of the mass spectra are discussed in chapter 3 with time of flight mass spectrometer results.

2.1.2 Experimental Equipment

Nozzle

The nozzle is a most significant component of a cluster beam source. Its geometry determines flow, cluster size, beam divergence and temperature of the beam. Unlike the sources for molecular beams that use sonic nozzles, a variety of nozzles has been used for the cluster beams. In Fig. 2.3, three types of nozzles are shown, sonic nozzle, conical nozzle and Laval nozzle. The sonic nozzle is preferred for the study of small

clusters of less than ten atoms. On the other hand, the conical and Laval nozzles are converging-diverging supersonic nozzles, and are more efficient than a sonic nozzle for forming an intense cluster beam[34]. The Laval nozzle used in this study was made of glass with a throat diameter of 0.1mm and a diffuser length of 30mm. The flow rate of Ar gas was 600sccm at a pressure of 4000Torr.

The cluster beam intensity (I) generated by supersonic expansion depends on the source pressure P_0, nozzle diameter D and temperature of the source gas T_0. It is described as follows[34];

$$I \propto P_0 \cdot D \left(\frac{T_b}{T_0}\right)^{\frac{\gamma}{\gamma-1}} \tag{2.6}$$

where γ and T_b are the specific heat ratio and the boiling point of the source gas, respectively. From Eq. 2.6, the neutral beam intensity I increases with P_0 and $1/T_0$ when D and T_b are fixed.

Fig. 2.4 shows the dependence of the neutral beam intensity on the source gas pressure and temperature. The neutral beam intensity was obtained from the difference of the vacuum pressure at the target chamber when the shutter was opened or closed. The neutral beam intensity started to increase from P_0 of 1000Torr and increased monotonically with P_0. When the source gas temperature was decreased to 220K, the neutral beam intensity at the same P_0 was twice as high as that at room temperature. Higher pressures and lower temperatures are significant to obtain an intense cluster beam.

Skimmer

The skimmer which extracts the core of the cluster beam flow has the shape of a truncated cone. The outer and inner angles of the orifice are 25° and 30°, respectively. The skimmer (Beam Dynamics Inc.) is made from Ni and its lip is made as sharp as possible to avoid collisional distortion in it. The distance between a skimmer and a nozzle x_{n-s} is important to get an intense cluster beam. In the case of a short x_{n-s}, distortion of the flow downstream of the skimmer is probable. When a skimmer is located far from a nozzle, the neutral cluster beam collides with the residual gases and a shock wave called a Mach disk is generated upstream of the skimmer. From numerical studies, the position of the

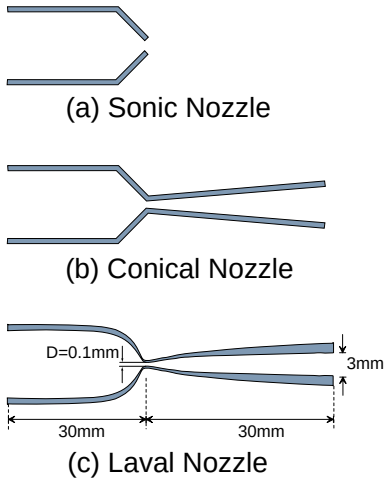

Figure 2.3: Schematic diagrams of the nozzle shapes.
(a) sonic nozzle, (b) conical nozzle, (c) Laval nozzle.

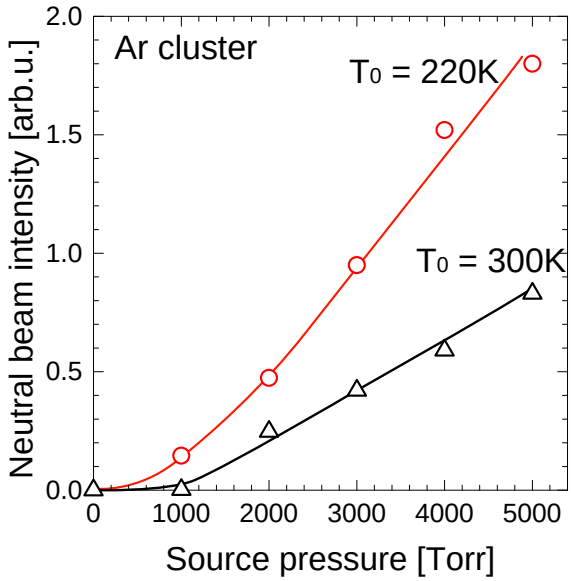

Figure 2.4: Source pressure and temperature dependence of neutral beam intensity.

shock wave x_m is approximated as follows[35].

$$x_m = 0.67D\sqrt{\frac{P_0}{P_s}} \tag{2.7}$$

where D, P_0 and P_s are nozzle diameter, source gas pressure and pressure in the vacuum chamber, respectively. When a shock wave is generated, the intensity of neutral beam decreases suddenly. Therefore, an optimum position exists which was 30mm in the apparatus used in this study. Eq. 2.7 indicates that the position of the Mach disk is determined by the pumping speed of the source chamber. To keep a good vacuum condition in the source chamber, a vacuum pump with high pumping speed is required.

Pumping System

As the flow rate of a cluster beam is several orders of magnitude higher than in a molecular beam system, a high pumping capability is required in the source chamber to avoid shockwave generation. For an basic study, the cluster beam is operated in a pulsed mode, which yields equivalent high pumping speed. However, for use in practical applications such as thin film formation and sputtering, a continuous and intense cluster ion beam is required. Fig. 2.5 shows a schematic diagram of the 30keV gas cluster ion beam apparatus[36]. The source chamber was evacuated with a mechanical booster pump (ULVAC, PMB012C), which reaches an efficient pumping speed ($330l$/s) at around 10^{-1} Torr at which pressure the pumping speed of a rotary pump is low.

The high gas flow rate may result in a large amount of residual gas remaining in the ionizing chamber. When residual gases are ionized and accelerated, dissociation or fragmentation of the cluster beam is probable because the velocities of the ionized particles and the neutral beam are quite different. To avoid poor vacuum pressure in the ionizing chamber, a differential pumping chamber was installed between the source and ionizing chambers with an aperture of 5mm diameter. The differential pumping chamber was evacuated with a 10 inch diffusion pump (ULVAC, ULK-10A, $3500l$/s), so that the pressure was kept below 1×10^{-4}Torr during gas expansion from 4000Torr.

The ionizing and target chamber were evacuated by oil-free turbo molecular pumps (Mitsubishi heavy industry, PT500 and FT2000W). The pumping speeds of the turbo pumps were $500l$/s and $2000l$/s, respectively. Since the mean free path of a cluster is much less than that of

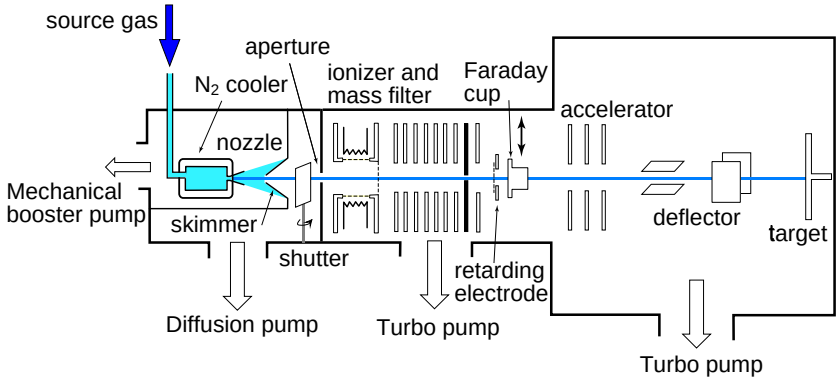

Figure 2.5: Schematic diagram of the 30keV gas cluster ion beam apparatus.

monomer, the vacuum pressure must be kept below 5×10^{-5}Torr to obtain intense cluster ion beams. The vacuum pressures in the ionizing and target chambers were kept below 1×10^{-5} and 5×10^{-6} Torr, respectively, during irradiation.

2.2 Cluster Ion Source and Accelerator

2.2.1 Ionizer

The ionization of the neutral cluster is necessary in mass analysis of cluster beams and energy deposition on the target. In general, ionization is performed with electrons or photons. When a photon is used, the energy balance is quite clear, therefore, photo ionization is convenient for a fundamental study of cluster beams. However, the ion beam intensity with photo ionization is usually lower than that with electron bombardment. In this study, a high ion current is needed because high fluences are required for applications such as surface smoothing. Therefore, hot electron emission from a filament was used.

The schematic diagram of the ionizer is shown in Fig. 2.6. Electrons were emitted from a hot filament of thoriated tungsten wire and were accelerated by a voltage applied between the filament and cylindrical anode (V_e). The anode was surrounded by three filaments 0.3mm in diameter and 40mm in length, and the diameter of the cylindrical anode was 25mm. The neutral cluster beam passed inside the cylindrical anode and was ionized by electron bombardment. When the filament current

I_f and ionization bias V_e were set at 21A and 150V, respectively, the emission current I_e was 70mA. The exit side of the anode was covered with a grid with high transmittance (90%), which avoided the distortion of the electrostatic potential inside the anode.

Ionized particles were accelerated by two-stage extraction voltages. As the velocity of all neutral particles is the same, the initial kinetic energy of a monomer is much lower than that of a cluster. Thus, the fraction of monomer ions can be reduced by means of space charge effects by applying a low voltage ($\sim$ 10V) on the first extraction electrode (V_{ext}). As a result, only cluster ions with large initial kinetic energy are extracted. If the electrostatic potential inside of the anode is not uniform, it causes both a reduction of mass resolution with retarding potential method and an additional extraction of monomer ions. The stainless steel grid on the exit side of the anode avoided these effects.

After extraction with a low voltage, the cluster ion was accelerated by a high voltage ($\sim$ 2kV). Fig. 2.7 shows cluster size distributions with high (500V) and low (12V) extraction voltages V_{ext}. The ionization electron bias V_e, ionization electron current I_e and total acceleration voltage V_a were 150V, 70mA and 2kV, respectively. In the case of V_{ext}=500V: large amounts of monomer ions were extracted, whereas little monomer ion beam was extracted in the case of V_{ext}=12V. The combination of the two-stage extraction with the fine grid on the exit side of the anode resulted in the fraction of monomer ions being reduced to less than a few percent.

Subsequently, cluster ions were focused by three electrostatic lenses. The difference of the initial energy between cluster and monomer caused chromatic aberration of the electrostatic lens. The separation of monomer ions from the cluster beam was possible with this electrostatic lens assembly and small aperture. However, mass separation with chromatic aberration was not used in the experiment because the small aperture caused a decrease of ion current.

A retarding electrode was located downstream from the lens assembly, and the cluster size distribution could be measured approximately. The retarding potential method is explained in the section 2.3.3 below. The cluster ion current was measured with a Faraday cup. Both the retarding electrode and the Faraday cup could be removed from the beam axis by linear motion during irradiation studies.

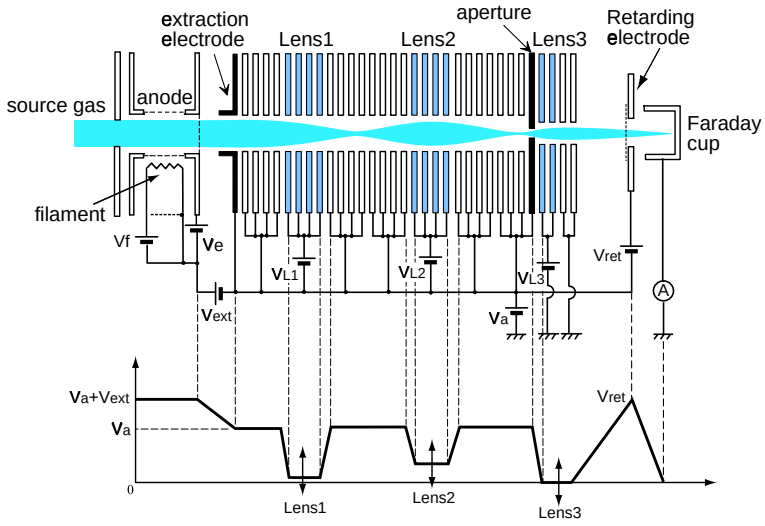

Figure 2.6: Schematic diagram of the ionizer and the associated electric potential.

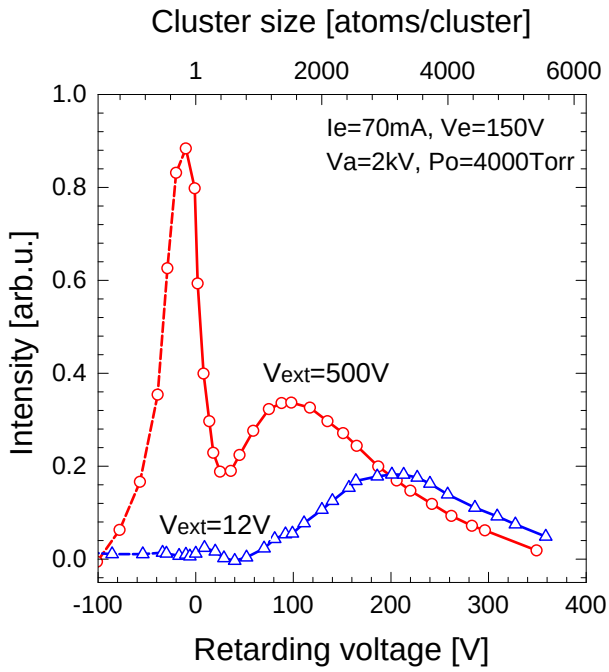

Figure 2.7: Ar cluster size distribution at low (12V) and high (500V) extraction voltages measured with the retarding potential method.

2.2.2 Accelerator

Clusters ionized in the ionizing chamber were accelerated up to 30keV by an acceleration column in the target chamber. As the target was biased at -30kV below ground potential, the entire component assembly in this chamber was shielded by a stainless steel cage. The acceleration column had three electrodes and equally divided acceleration voltages were supplied between each electrode.

There were two pairs of deflectors on both horizontal and vertical axes. Triangular waves with different frequencies were applied on each deflector which enables uniform irradiation of the target. The maximum wafer diameter is 6 inches. Uniformity of the irradiation was evaluated from the damaged layer thickness on a Si substrate as measured with an ellipsometer, and it was found to be better than 2%.

The ion dose was measured with a current integrator, and when the desired ion dose was attained, a shutter stopped irradiation automatically. As the target was floating at -30keV, the ion current value was transferred through an optical cable to a display at ground potential. The irradiation area was defined by a mask on the target. The cluster ion current at the target was $2.6\mu A/cm^2$ at an acceleration energy of 20keV.

When a cluster ion impacts a target, large numbers of secondary electrons are emitted, resulting in an increase of the observed ion current. Since the ion dose was counted by ion current, secondary electron emission caused a difference between actual and observed ion doses. To suppress secondary electron emission, a voltage of -90V below the target voltage was applied to the mask. Secondary electrons emitted from the target return to it and an accurate ion current can be measured.

Fig. 2.8 shows the diameter of cluster ion beams at the target. The cluster beam current was measured with two wires located with 40mm spacing, and the cluster ion beam was scanned by a deflector. The cluster ion beam diameter was measured from the full width at half maximum of the ion current. With a decrease of the acceleration voltage, the cluster ion beam became dispersed by the space charge effect. When the acceleration voltage was 20kV, the beam diameter was 3.6mm.

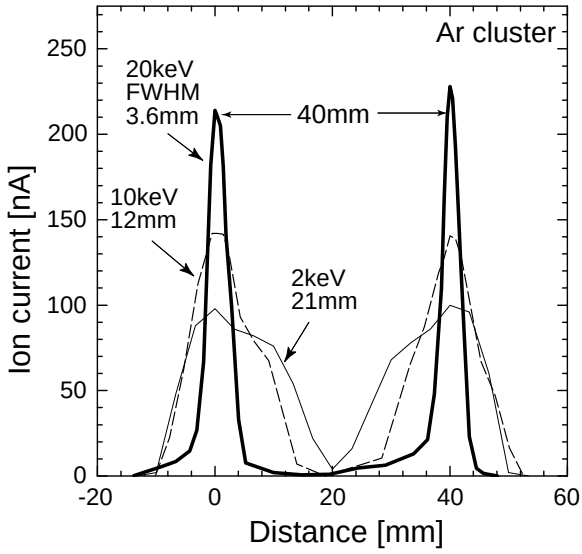

Figure 2.8: Diameters of Ar cluster ion beams at the target accelerated from 2 to 20keV.

2.3 Mass Spectrometer

As the cluster size defines its physical properties, it is important to measure the cluster size distributions accurately. However, the most obvious peculiarity of the clusters is their unusually large mass. To detect Ar clusters with size of 1000, an instrument with a mass range of 40,000 atomic mass units is required.

The mass spectrometric method is roughly classified in two modes. One uses a static electromagnetic field that does not depend on the time, and the another uses a dynamic field. The former method is used for continuous cluster beams, while the latter one is used for pulsed cluster beams. There are several kinds of mass spectrometers suitable for large clusters. In this section, the principle of the time of flight mass spectrometer, Wien filter, retarding potential method and quadrupole mass spectrometer, which were used in this study, are described.

2.3.1 Time of Flight (TOF) Mass Spectrometer

Typical construction of a TOF mass spectrometer is shown in Fig. 2.9. The principle of TOF mass spectrometry is to measure the flight time of

ions with various masses but with the same energy. Since the flight time is proportional to the square root of the mass, the masses of the ions are obtained directly from the flight time.

Neutral particles with atomic mass of m are ionized by an electron or photo ionization pulse with a short duration time, and then accelerated by the same acceleration voltage V. Subsequently, ions drift in a field-free region of length l and, finally, reach an ion detector. The flight time t from the ionizer to the detector is expressed as follows.

$$t = l\sqrt{\frac{m}{2eV}} \tag{2.8}$$

where e is a charge of the ion. As l and V are fixed, an accurate mass to charge ratio m/e can be measured.

Time of Flight (TOF) mass spectrometers have become popular in cluster physics and chemistry. There are many advantages to a TOF mass spectrometer compared with other mass spectrometers. First, there is no limitation on the size of the mass to be measured. In cluster science, the cluster size exceeds 1000, which corresponds to atomic mass of greater than 40,000 in case of Ar. Other mass spectrometers cannot be applied for such large cluster ions. Second, the mass spectra of all particles can be measured within a short time and, in the typical experimental setup, this ranges from a few to several hundred μsec. The transmittance of the ion with TOF is relatively high, and this is important because the fraction of cluster ions in the cryogenic beam is less than a few percent. Finally, the construction of a TOF system is very simple, and it is possible to construct it in the laboratory at low cost.

The mass resolution is determined by the energy distribution of the ions with the same mass. To improve the energy distribution, the two-stage acceleration method and the reflectron type of TOF mass analyzer were developed. With the reflectron TOF mass analyzer, the mass resolution of 10,000 was realized[37]. Details of the TOF measurements are also discussed in chapter 3 below.

2.3.2 Wien Filter

A Wien filter is a mass spectrometer which uses both electric and magnetic fields. The ion transmittance of this filter is high and its construction is very simple. Cluster beam axis, electric field (E) and magnetic field (B) are all mutually perpendicular. Ions in the Wien filter are in-

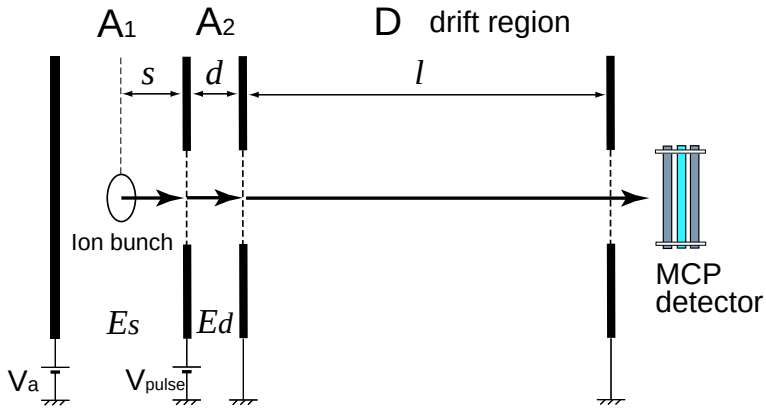

Figure 2.9: Schematic of a Time of Flight (TOF) mass spectrometer under the linear mode operation.

fluenced both by an electric force and Lorenz force with magnetic fields. As the electric and Lorenz forces work in opposite directions, only appropriately sized clusters go straight through along the center of the beam axis. The cycloid motion of an ion in the electromagnetic field depends on its initial velocity (v) and it becomes linear motion when v equals to E/B.

As a cluster has a kinetic energy which is proportional to its size, a cluster with size of N accelerated by an acceleration voltage V_a has a total energy which amounts to $eV_a + \alpha n$ (where α is a constant). Therefore, the cluster size n selected by Wien filter is described as follows.

$$n = \frac{2eV_aB^2}{mE^2 - 2\alpha B^2} \tag{2.9}$$

where, m is the mass of one atom in a cluster. Fig. 2.10 shows the cluster size distribution at several source pressures measured with a Wien filter. The acceleration voltage and magnetic field were 2kV and 0.4T, respectively. With increasing source gas pressure P_0, the beam intensity increased and the average cluster size was about 3000 atoms/cluster at 3000Torr. Mass resolution of a Wien filter is degraded at high cluster size. For example, when the desired cluster size is 2000atoms/cluster, the cluster size which can pass through the Wien filter ranges from 1000 to 3000 (V_a=2kV, B=0.4T). A high magnetic field is required for high mass resolution at large cluster size with a Wien filter.

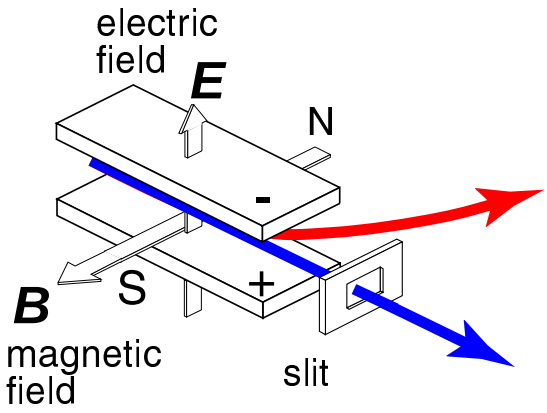

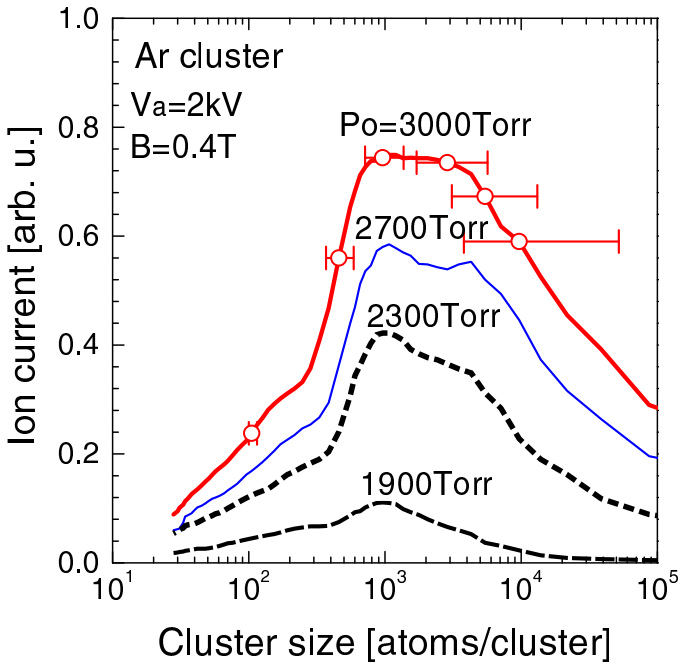

Figure 2.10: Ar cluster size distribution measured with a Wien filter at several source presssures. (V_a=2kV, B=0.4T)

2.3.3 Retarding Potential Method

The principle of the retarding potential method is based on the fact that the kinetic energy of a neutral cluster is proportional to its size. Though the mass resolution with this method is quite low, it is the most simple and the easiest way to measure the approximate cluster size distribution.

During a supersonic expansion, atoms collide with each other and exchange their energy. Subsequently, the translational velocity of all particles becomes the same. As all particles, from monomers to clusters, have the same velocity, the kinetic energy is proportional to the cluster size n. The velocity (v) and kinetic energy (K) are described as follows.

$$v = \sqrt{\frac{\gamma}{\gamma-1}\frac{2kT_0}{m}} \tag{2.10}$$

$$K = \frac{1}{2}mv^2 \cdot n = \frac{\gamma}{\gamma-1}kT_0 \cdot n \tag{2.11}$$

where m, γ, k and T_0 are the atomic mass of the monomer, the ratio of the specific heats, Boltzman constant and the temperature of the source gas, respectively. In the case of Ar ($\gamma = 5/2$), the velocity is 560m/s at room temperature, which corresponds to energy per atom of 64.6meV.

The cluster size distribution is obtained from the energy distribution of the beam. In this method, a cluster ion which overcomes the retarding potential is measured as an ion current. When the retarding potential is lower than the acceleration voltage, all of the ions reach the Faraday cup. However, when the retarding potential exceeds the acceleration voltage, low energy particles such as monomers and small clusters are repelled by it, and large cluster ions with high energy pass through it. Therefore, the retarding potential works as a high-pass energy filter, and the energy distribution can be obtained from the negative derivative of the retarding spectrum.

Fig 2.11 shows a retarding spectrum and its energy distribution for an Ar cluster beam. The source pressure P_0 was 4000Torr and the extraction voltage V_{ext} was 500V. As a cluster ion beam contained many monomer ions under high extraction voltage, the retarding spectrum showed a sudden decrease at a retarding voltage of 0V. The energy can be converted to cluster size using the fact that each atom has an energy of 64.6meV.

To evaluate the accuracy of the retarding potential method, the mass distributions of cluster ions that overcome the retarding electrode was also measured with time of flight mass spectrometer. Fig. 2.3.3 shows

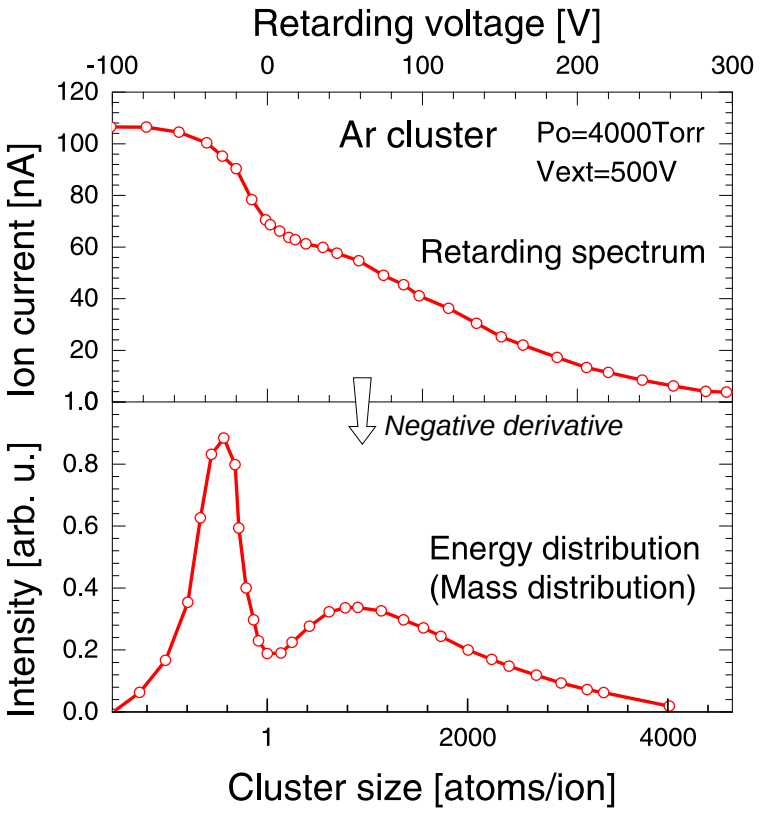

Figure 2.11: Retarding spectrum (upper) and cluster size distribution (bottom) obtained from the negative derivative of the retarding spectrum.

TOF spectra of Ar cluster beams overcoming the retarding electrode. The retarding voltages (V_{ret}) were increased from 0V to 150V. The retarding voltages of 50, 100 and 150V corresponded to cluster sizes of 775, 1550 and 2325, respectively. From Fig. 2.3.3, with increasing V_{ret}, the minimum size of cluster shifted to larger values, and they were almost equal to the cluster size corresponding to eV_{ret}/64.6meV, where e is a charge of the cluster ion.

The mass resolution of the retarding potential method is defined principally by the uniformity of the potential at the ionizing point and the retarding electrode. The energy resolution of a typical retarding electrode is about 10eV which corresponds to a size of 150. Therefore, the mass resolution of this method is quite low compared with that of other mass spectrometers. The retarding potential method only requires locating an electrode in the ion beam axis, and is easiest way to do a rough measurement of the cluster size distribution.

2.3.4 Quadrupole Mass Spectrometer

The quadrupole mass spectrometer was developed in 1950's by Paul and co-workers[38]. Four rods with length of 20 to 30cm are mounted symmetrically, and both DC bias (U) and a radio frequency (f) with several kV bias (V) are applied to the diagonal pairs of rods. Thus, the electrostatic potential Ψ in the quadrupole is described as follows[39].

$$\Psi = \{U + V\cos(2\pi ft)\}\frac{x^2 - y^2}{r_0^2} \tag{2.12}$$

where r_0 is the distance between the beam center and each rod. While ions stay in the quadrupole, they oscillate in both horizontal and vertical directions. The trajectory of ions in the quadrupole is described by Mathieu's equation. Whether the ion trajectory becomes stable or unstable depends on their mass M, f and U/V. Ions with a particular mass reach the detector, and the ion signal is amplified with an electron multiplier. In practical use, the frequency is fixed and the U/V ratio is changed to obtain mass spectra. Since the mass resolution increases according to the number of oscillation in the quadrupole, high frequency and a low impinging ion energy are necessary. The mass measurements of cluster beams using a quadrupole mass spectrometer are discussed in Chapter 3 below.

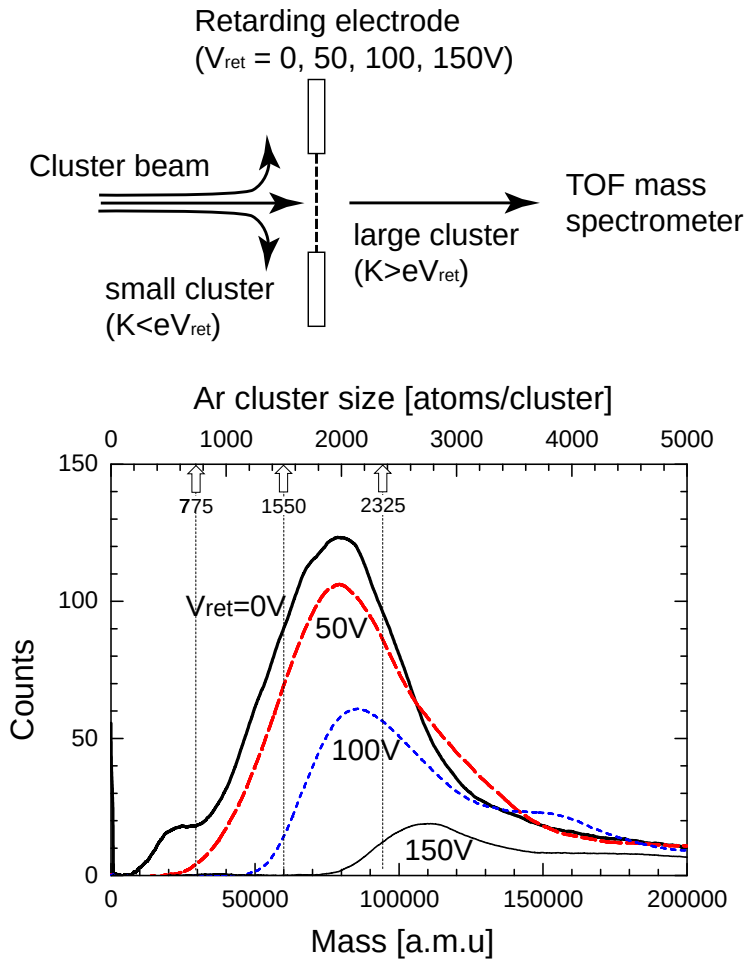

Figure 2.12: Ar cluster size distribution after filtering with the retarding potential method. The retarding voltages V_{ret} of 50, 100 and 150 correspond to the cluster sizes of 775, 1550 and 2325, respectively.

2.4 Summary

In this chapter, the theoretical view of cluster beam formation was described with flow dynamics theory. The experimental cluster ion beam equipment including cluster source, ionizer and accelerator, was presented. In addition, various methods of cluster size measurement were described. The following are summarizing remarks of this chapter.

1. Supersonic expansion through a nozzle is the most suitable method for the formation of clusters from gaseous material. A cryogenic beam with a temperature of a few degree K can be realized with supersonic expansion. Neutral clusters grow by monomer-cluster and cluster-cluster collisions.

2. Cluster beam intensity is proportional to both the source pressure (P_0) and the inverse of source temperature ($1/T_0$). To avoid the decrease of neutral beam intensity due to the shock wave, a cone shaped skimmer was mounted on the downstream side of the nozzle at a distance of 30mm. The skimmer rim is made as sharp as possible to avoid the formation of collisional distortion.

3. Neutral clusters are ionized by electron bombardment from a hot filament. The fraction of monomer ions in the cluster beam is reduced to less than a few % through the use of a low extraction voltage and an uniform potential inside the anode. Only ionized clusters with high initial kinetic energy are extracted.

4. The diameter of a cluster ion beam at the target was 3.6mm at an acceleration energy of 20kV. The uniformity on the target was better than 2% with scanning of the cluster beam by deflectors. By optimizing extraction and transport conditions, a high cluster ion current density of $2.6\mu\mathrm{A/cm}^2$ was obtained at an acceleration voltage of 20keV.

5. Time of Flight, Wien filter, retarding potential method and quadrupole mass spectrometers were used for the measurement of cluster size distributions. Clusters with several thousands of atoms were generated with the supersonic expansion.

Chapter 3

Properties of Cluster Beams

3.1 Time of Flight Mass Spectrometer

3.1.1 General Characteristics

As described in section 2.3.1, a Time of Flight (TOF) mass spectrometer is necessary for the cluster beam study because of its many advantages to deal with the huge mass. However, the mass resolution of a simple TOF mass spectrometer is relatively low and many improvements have been reported[40, 41]. As the mass resolution of a TOF is limited by the energy distribution of the ion bunch[42, 43], these improvements concentrated on the time-focusing of the ion bunches at an ion detector. There are two main time-focusing methods used in TOF mass spectrometers. One uses two-stage extraction, and the other uses a reflection electric field (reflectron).

Linear (Wiley-McLaren) type of TOF

In the case of one-stage acceleration, the mass resolution is extremely low. Wiley and McLaren showed that the mass resolution was improved drastically with the two-stage acceleration[40] which realized first order focusing at the ion detector. A schematic diagram of a linear TOF mass spectrometer was shown in Fig. 2.9, above.

When a neutral particle with atomic mass m is ionized at position s, it is pre-accelerated by the electric field (E_s) in the A_1 region, and it gains an energy of sE_s. Then, the ion is post-accelerated in the A_2 region with a spacing d by the electric field E_d and, as a result, it gains the energy

of dE_d. Then ions transit in the drift region D with length l and, finally reach an ion detector. If the ion has an energy of U ($U = sE_s + dE_d$), the flight time $t(s)$ is expressed as follows.

$$\begin{aligned} t(s) &= t_{A_1} + t_{A_2} + t_D \\ &= \sqrt{\frac{2m}{e}} \cdot \left\{ \sqrt{\frac{s}{E_s}} + \frac{1}{E_d} \left[\sqrt{U} - \sqrt{sE_s} \right] + \frac{l}{2\sqrt{U}} \right\} \end{aligned} \tag{3.1}$$

where, t_{A1}, t_{A2} and t_D are the flight times in the region A_1, A_2 and the drift region D, respectively.

As expressed in Eq. 3.1, the flight time depends on the ionization position s. Focusing is based on the fact that if the ionization position is closer to the detector (short s), an ion acquires lower energy. Therefore, at a certain position, it is overtaken by ions which were ionized upstream (long s) and have higher energy. If the center of the ionization position is defined as s_0, the position where these ions pass each other can be obtained by taking $(dt/ds)_{s=s_0} = 0$ in Eq.3.1. It becomes,

$$l = 2s_0 k_0^{\frac{3}{2}} \left\{ 1 - \frac{d}{s_0(k_0 + k_0^{\frac{1}{2}})} \right\} \tag{3.2}$$

$$k_0 = \frac{s_0 E_s + dE_d}{s_0 E_s} \tag{3.3}$$

This focusing condition is the same for all kind of ions and also independent of the total energy U. If s_0, d and l are fixed, E_d/E_s is determined uniquely from Eqs.3.2 and 3.3. Thus the time focusing condition of a linear TOF is optimized by the ratio of E_d/E_s.

Reflectron type of TOF

The reflectron type of TOF compensates the energy distribution by an ion reflector[41]. A schematic diagram of a reflectron type of TOF mass analyzer is shown in Fig. 3.1. Shown are the retarding field with length d_T and the reflection field with length d_K in the reflectron. The trajectory of the high-energy ion is deeper than that of the low energy ion and the former one stays longer in the reflectron than the latter one. Consequently, both of the ions reach the detector at the same time. The time focusing at the ion detector results in an improvement of mass resolution. A reflectron is usually constructed with a few tens of electrodes with high

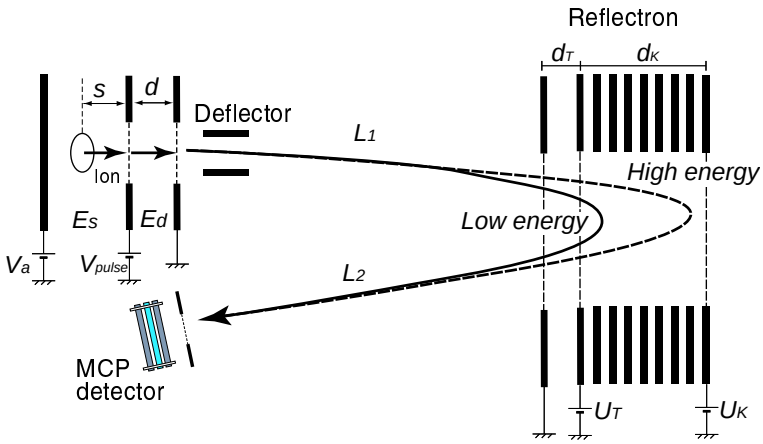

Figure 3.1: Schematic diagram of the reflectron type of TOF.

transparency mesh, and an uniform electric potential is supplied with dividing resistors. The uniformity of the electric field is necessary for high mass resolution.

If the energy of each ion, the average energy and their ratio are defined as eU, eU_0 and $k = U/U_0$, respectively, the total flight time t is expressed as follows[41].

$$\begin{aligned} t &= t_D + t_T + t_K \\ &= \frac{l}{\sqrt{2eU_0/m}}\frac{1}{\sqrt{k}} + \frac{4d_T}{\sqrt{2eU_0/m}}\frac{U_0}{U_T}\cdot\left(\sqrt{k} - \sqrt{k - \frac{U_T}{U_0}}\right) \\ &= +\frac{4d_K}{\sqrt{2eU_0/m}}\frac{U_0}{U_K}\cdot\sqrt{k - \frac{U_T}{U_0}} \end{aligned} \tag{3.4}$$

where, t_D, t_T and t_K are the flight time of the drift, the retarding and the reflection regions, respectively. U_T and U_K are the electric potential of the retarding and reflection regions, respectively. The focusing condition is expressed as;

$$\left(\frac{dt}{dU}\right)_{U=U_0} = 0 \quad , \quad \left(\frac{d^2t}{dU^2}\right)_{U=U_0} = 0 \tag{3.5}$$

From the Eqs.3.4 and 3.5, the relation under the focusing condition is obtained, which is approximated as follows[41].

$$\frac{L}{4d_K}\frac{U_K}{U_0} \simeq \sqrt{3} \quad , \quad \frac{U_T}{U_0} \simeq \frac{2}{3} \tag{3.6}$$

Therefore, the focusing is optimized by adjusting U_T and U_K. In the case of the linear TOF mass spectrometer, the maximum mass resolution $m/\Delta m$ was 500∼800[43, 44], however, $m/\Delta m$ values of 1000∼3000 were obtained with the reflectron TOF[45]. Development of a reflectron TOF with $m/\Delta m$ of 30,000 was reported by Martin et al.[46].

3.1.2 Construction of TOF Mass Spectrometer

Ionizer

The schematic diagram of the time of flight spectrometer used in this study is shown in Fig. 3.2. Neutral cluster beams are injected into the TOF chamber in direction perpendicular or parallel to the flight axis. These neutral clusters are ionized by electron bombardment.

Ionization of the neutral particles is performed between two electrodes. The electron gun is mounted on the XY-table and the ionization position can be changed according to the direction of the impinging beam. Typical ionization energy and the electron emission current from a hot filament are 70eV and 0.5mA, respectively. The ionization energy can be changed from 40 to 100eV.

Ion Optics

Ionized clusters are extracted by the electric field between the two electrodes (A and B) indicated in Fig. 3.2. A fixed acceleration voltage V_a is applied on (A), and a pulsed extraction voltage $V_a - V_{pulse}$ is applied on (B). The duration time and the repetition rate of V_{pulse} are 10μsec and 200Hz, respectively. V_{pulse} is changed from 150 to 300V according to the acceleration voltage to realize time-focusing at the detector.

As described in the previous section, two-stage acceleration is performed to improve the mass resolution. The time focusing condition is optimized by the ratio of V_a/V_{pulse}. A deflector and an Einzel lens assembly are located downstream from the accelerator. The ionized cluster subsequently enters a flight tube 120cm in length which is grounded and where the inside is field-free.

Under linear TOF operation, the flight ions are detected by a Micro Channel Plate (MCP) mounted on the end of the TOF chamber. In the case of reflectron TOF operation, ions are decelerated and reflected by the reflection field. The reflectron consists of a column of electrodes with high transmittance mesh (90%). The reflected ions drift in the field-free

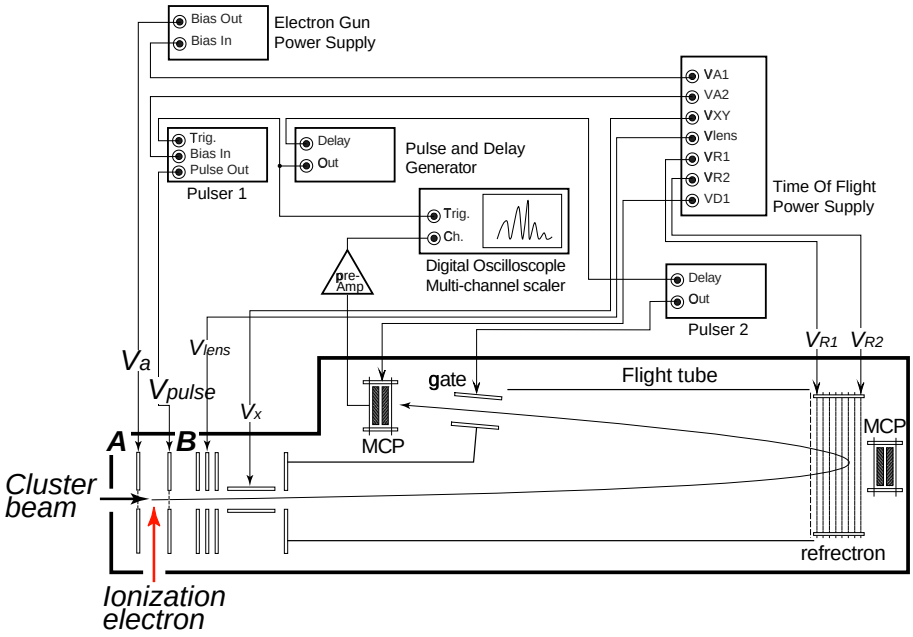

Figure 3.2: Experimental construction of a Time of Flight mass spectrometer.

region again and reach another MCP detector mounted on the opposite side of the reflectron. When energetic ions reach the top plate of the MCP, secondary electrons are emitted and are amplified exponentially in the channel plate biased with 900V between each plate. The detection of large clusters with MCP is discussed in section 3.1.4 below.

Acquisition of Mass Spectra

A trigger signal that defines the beginning of TOF is generated by a function generator (Iwatsu, FG-330). This signal is supplied to all equipment, and in some cases a digital delay (Stanford Research System, DG-535) is used to adjust the slight difference in the timing. The secondary electron current from the MCP is amplified 100 times with a pre-amplifier (NF electronic, BX-31A) terminated by a 50Ω impedance. The time dependent signal is recorded on a digital oscilloscope (Lecroy, 9310A) or a multi-channel scaler (Stanford Research System, SR-430). The multi-channel scaler is used with a pulse counting operation.

The multi-channel scaler is equipped with a discriminator and 16,000 counters (scaler). The discriminator outputs a TTL pulse only when the

signal exceeds a certain voltage (V_{disc}), and the output pulses are counted with a certain scaler corresponding to the flight time. The mass range and time resolution are defined by the duration time of the scaler (called 'bin width'). The counts of each scaler are integrated over several ten thousands of sweeps and the final spectrum is stored in a computer. By the pulse counting technique with a multi-channel scaler, the signal to noise ratio is drastically improved over that obtained by direct measurement with a digital oscilloscope.

Mass Resolution

To measure the mass resolution of both linear and reflectron TOF mass spectrometers, Xe was fed into the TOF chamber as an ambient gas. Xe has a large mass and there are many isotopes between the atomic masses of 124 and 136. The major isotopes of xenon are ^{128}Xe(1.9%), ^{129}Xe(26.4%), ^{130}Xe(4.1%), ^{131}Xe(21.2%), ^{132}Xe(26.9%), ^{134}Xe(10.4%) and ^{136}Xe(8.9%)[47].

Fig.3.3 shows mass spectra of Xe under the linear TOF operations. The acceleration voltage V_a was 1.5kV and the extraction voltage V_{pulse} was changed from 150 to 220V. The time focusing condition was fulfilled by the ratio of V_a/V_{pulse} in the linear TOF mode. When V_{pulse} was 170eV, each peak from the Xe isotopes was very sharp and the ratio of the existing isotopes showed good agreement with the reference values. However, the peaks became less intense and broader when V_{pulse} was 150V or 220V. This result indicates that the time focusing with two-stage acceleration was realized when V_{pulse} was 170V. From the full width at half maximum (FWHM) of the Xe peaks, the mass resolution $m/\Delta m$ was about 500 with the linear TOF mode.

Also, Fig. 3.4 shows mass spectra of Xe with a reflectron TOF operation. The acceleration voltage was 1.5kV, and the voltage of entrance (V_T) and exit (V_K) of the reflectron were 895V and 2000V, respectively. Compared with the linear mode, each isotope peak became sharp and narrow. From the FWHM of the Xe peak, $m/\Delta m$ was 1500 with this reflectron TOF mass spectrometer.

3.1.3 Extraction of Large Clusters

There are two directions for feeding the neutral cluster beam into a TOF analyzer, i.e., parallel or perpendicular to the beam axis of the TOF.

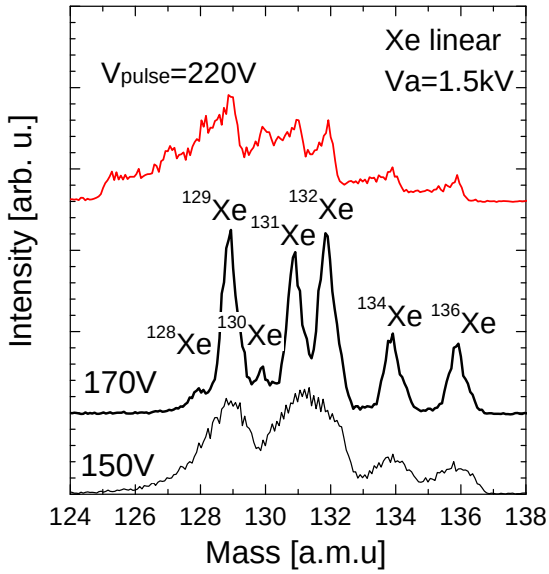

Figure 3.3: TOF mass spectra of Xe under the linear mode operation. (Mass resolution $m/\Delta m$=500 at V_{ext} = 170V)

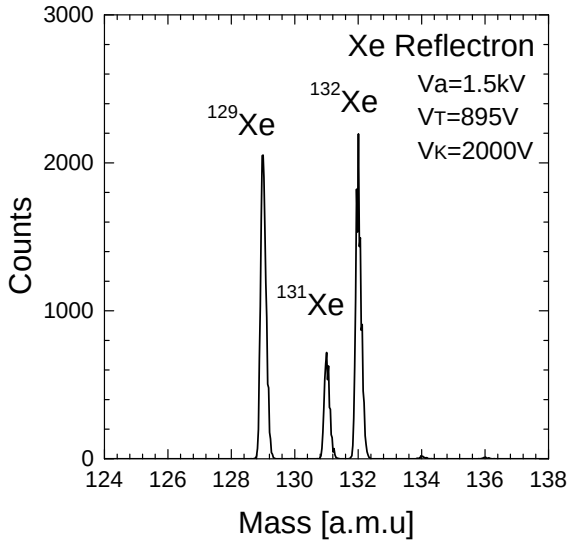

Figure 3.4: TOF mass spectrum of Xe under the reflectron mode operation. (Mass resolution $m/\Delta m$=1500)

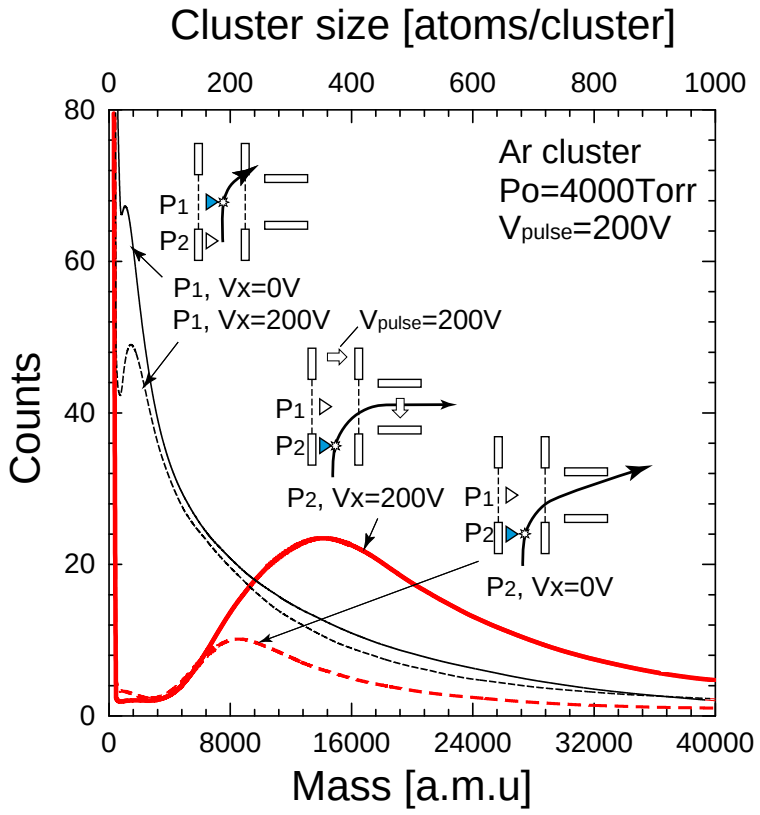

Figure 3.5: TOF mass spectra of Ar cluster at various extraction conditions.

Ionizing position of P_1, P_2 is the center of TOF beam axis and 18mm upstream from the center, respectively. V_x is deflection voltage. Perpendicular extraction voltage V_{pulse} is 200V.

In the case of perpendicular extraction, neutral clusters turn 90° to the beam axis of the TOF. Perpendicular extraction is preferred because the initial energy distribution is the main cause for the reduction of the mass resolution. However, the initial kinetic energies of neutral clusters with size of 3000 are several hundreds of eV, therefore, the drift motion perpendicular to the extraction direction is not negligible. To compensate for the perpendicular motion, deflection by a deflector or a change of the ionization point was carried out. In our TOF system, a deflector is mounted in the ionizing assembly and the ionization point can be changed by an XY-stage on which an electron gun is mounted.

Fig. 3.5 shows mass spectra of Ar cluster beams when the ionizing point and the deflection voltages V_x were changed. Neutral clusters were fed perpendicularly into the TOF axis and extracted by a V_{pulse} of 200V. One of the ionizing points was in the center of the ion beam axis (P_1) and the another was located 18mm upstream from the center (P_2). The source pressure of Ar was 4000Torr and the beam contained many large clusters.

When the ionizing point was in the center (P_1), mainly small clusters were extracted and few large cluster ions were observed at both V_x=0V and 200V (thin line). As the extraction voltage of 200V was almost the same as the kinetic energy of neutral large clusters, large clusters were extracted at an oblique angle. A large cluster conserves the initial velocity and it collides with some electrode before reaching the deflector. Therefore, large clusters could not be observed when the ionizing position was at center (P_1).

When the ionizing point was P_2 (thick line), there was enough space to drift to the oblique angle before reaching the deflector, as shown in Fig. 3.5. When V_x was 200V, larger clusters were observed than with a V_x of 0V. From these results, compensation of the initial velocity with a deflector and the change of ionization position was necessary to extract large cluster ions.

3.1.4 Detection of Large Clusters

Micro Channel Plate

Mass selected ions are detected by an ion detector which has a gain of $10^4 \sim 10^8$. Dynode, channeltron and micro channel plates are used for ion detection. The principle of these detectors is the same. Secondary

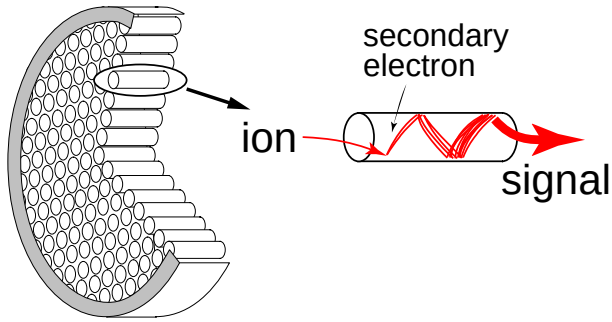

Figure 3.6: Structure of a Micro Channel Plate.

electrons that are produced on the top dynode are accelerated to a second dynode, resulting in amplification of the electron current. Sequential amplification of the electron converts a one ion signal to $10^4 \sim 10^8$ electrons.

Among these detectors, the Micro Channel Plate (MCP) is suitable for the time of flight mass spectrometer because it has a large detection area and fast response ($\sim$ 10psec). Fig. 3.6 shows a schematic diagram of an MCP. There are many small channels 10μm in diameter, and each channel is coated with a semiconductor material. Secondary electrons are generated by ion impact in the micro channel and accelerated by the bias between the plates. These electrons then bombard the walls of the channel plate again and numerous secondary electrons are emitted from there. In this study, a micro channel plate assembly (Galileo MCP-18B) with two stacked channel plates was used. The gain of the MCP depends on the voltage between each plate. The output of the MCP is terminated by a 50Ω resistor and a fast ion signal of sub-nanosecond transition can be detected.

As the MCP detects ion signals by secondary electron emission, no signal is observed when the secondary emission probability is zero. It is reported that the secondary electron emission is proportional to the velocity of the particles, and there is a threshold velocity[48]. The threshold velocity of secondary electron emission on a metal was reported as 2×10^4 [m/s], which is much faster than that of large cluster ions with an energy of several keV. When an Ar cluster ion with cluster size of 2000 is accelerated with an energy of 2keV, the velocity is only 2200[m/s]. It

is expected that the detection probability of the MCP for slow or large cluster ions is much smaller than for fast single ions.

Detection of Large Clusters with MCP

To clarify the velocity dependence of the detection probability with an MCP, time of flight spectra were taken at several acceleration voltages[49]. Fig. 3.7 shows TOF mass spectra of Ar cluster beams with an energy of $1.0 \sim 2.5$keV. The source pressure of Ar was 4000Torr.

There was no significant difference in the intensity of small clusters whose size was less than 1000 atoms/cluster. However, the intensity of large clusters (> 1500 atoms/cluster) increased with the acceleration energy. If these increases arose from an energy dependence of the ion optics of the TOF system, the intensity of all sizes should increase uniformly, but this was not the case.

The detection probability f_{det} with MCP is expressed in the following equation[50];

$$f_{det} = f_1(E) \cdot f_2(n) \cdot \exp\left(-\frac{1}{E_{atom}}\right) \tag{3.7}$$

where, $f_1(E)$ is an energy dependent constant which relates to the trajectory of an ion, $f_2(n)$ is a factor which depends on the number of atoms, and E_{atom} is the energy of each constituent atom in the cluster. From the secondary electron yield measurements from an Au surface under carbon cluster bombardment, the secondary electron emission increased almost linearly with the cluster size. However, in the large cluster size region, it is negligible compared with the exponential decay.

The TOF spectra in Fig. 3.7 were normalized to that at 2.5keV, and the relative detection rate versus cluster size was plotted on a logarithmic scale in Fig. 3.8. The relative detection rate was almost the same around the size of 1000, however, it showed an exponential decay with cluster sizes of over 1500. As shown in Eq. 3.7, f_{det} decreased exponentially with E_{atom}. Therefore, the main reason for the reduction of the relative detection rate of large cluster size was attributed to a decrease of E_{atom}, i.e. the velocity of the cluster ions.

The relative detection rate f_{det} versus velocity is shown in Fig. 3.9. When the velocity was larger than 2500m/s, f_{det} was almost unity which means that all of the ions in flight were detected by the MCP. However, with decreasing velocity, f_{det} suddenly dropped and there was a threshold for detection at around 1000m/s. Thus, if the velocity of a cluster ion is

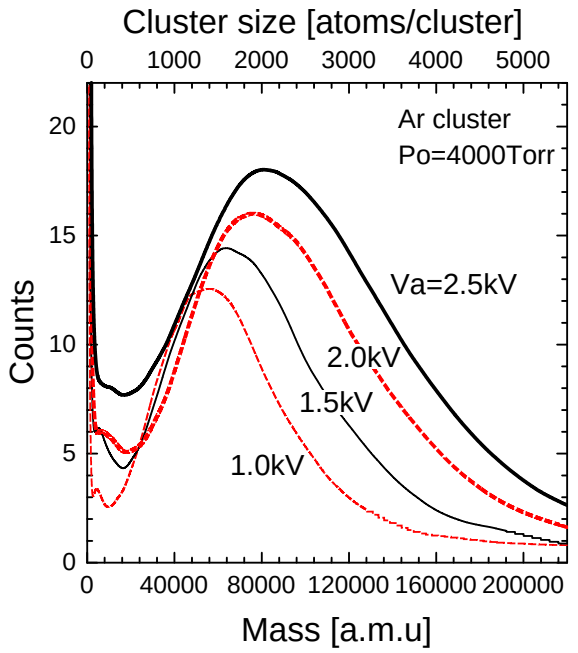

Figure 3.7: Acceleration voltage dependence of TOF mass spectra of Ar cluster beams.

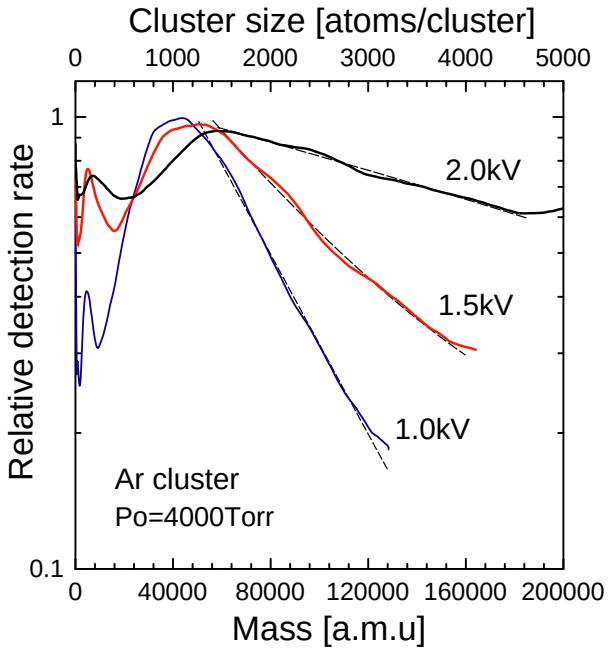

Figure 3.8: Relative detection rate of Ar clusters normalized to TOF spectra at acceleration voltage of 2.5kV.

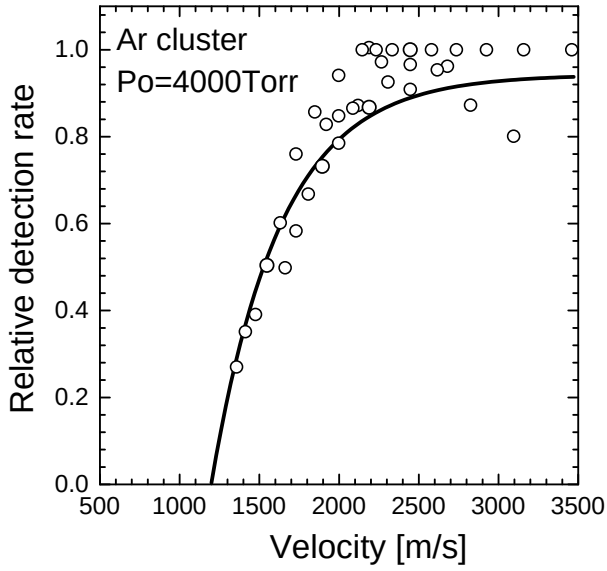

Figure 3.9: Velocity dependence of the relative detection rate with the MCP.

slower than 1000m/s, no signal will be observed.

When an Ar cluster with a size of 3000 is accelerated to an energy of 1.0keV, its velocity is 800m/s, which is less than the threshold velocity. On the other hand, when a cluster with a size of 3000 is accelerated to an energy of 2.5keV, its velocity is 2000m/s, which is sufficient for detection. It was reported that an acceleration energy of 16keV was required for the detection of large size ($\sim$ 20,000) Li, Na and Cs cluster ions[50].

The velocity dependent function of $f_{det}(v)$ can be obtained from curve fitting.

$$f_{det}(v) = 1 - \exp[-2.3 \times 10^{-3} \cdot (v - 1200)] \tag{3.8}$$

With this function, the actual cluster size distribution can be obtained by a compensation of the relative detection rate at low velocity.

Fig. 3.10 shows TOF mass spectra of Ar cluster beams compensated with $f_{det}(v)$. The original TOF spectra were taken with an energy of 2.5keV. The peak of the intensity was slightly shifted to a larger size, from 2000 to 2400 atoms/cluster.

The mass spectra of large cluster ions with conventional mass analysis, such as retarding potential method or Wien filter, showed that the average size of Ar cluster beams was about 2000 $\sim$ 3000 atoms/cluster. The cluster size distribution shown in Fig. 3.10 agrees well with those

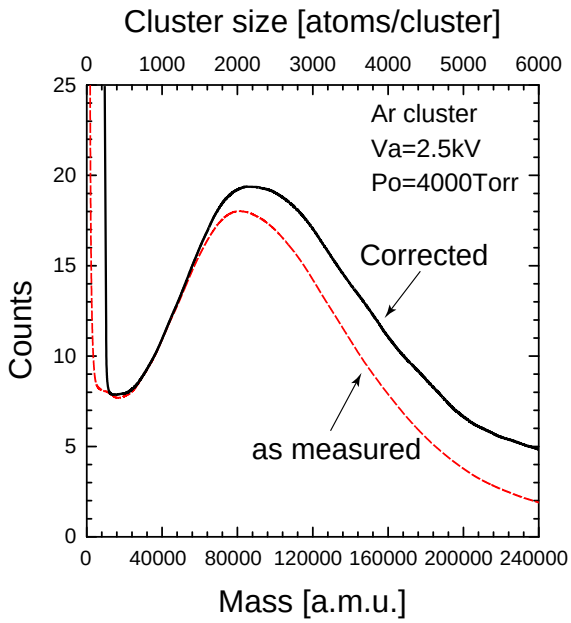

Figure 3.10: TOF mass spectra before and after correction of the relative detection rate.

measurements. With this compensation of the relative detection rate for large cluster ions, the accurate cluster size distribution can be obtained.

Detection of Cluster Ions as Charged Particles

As shown in the previous section, the main problem for the detection of large cluster ions with an MCP is the reduction of secondary electron emission. It means that the relative detection rate depends on the cluster size. If a large cluster ion can be detected as an ion current, there is no dependence for detection on the cluster size.

To measure the cluster size distribution using the ion current, a cluster source that provides intense cluster ion currents is necessary. As the volume of the electron gun in the TOF mass spectrometer is too small, the 30keV gas cluster ion beam apparatus shown in Fig. 2.5 was used instead. The maximum emission current of this apparatus was 40 times higher than that of the electron gun in the TOF. A pulsed voltage with a duration time of 10μsec was supplied on the deflector in the target chamber, and bunches of ionized clusters were formed. The ion signals

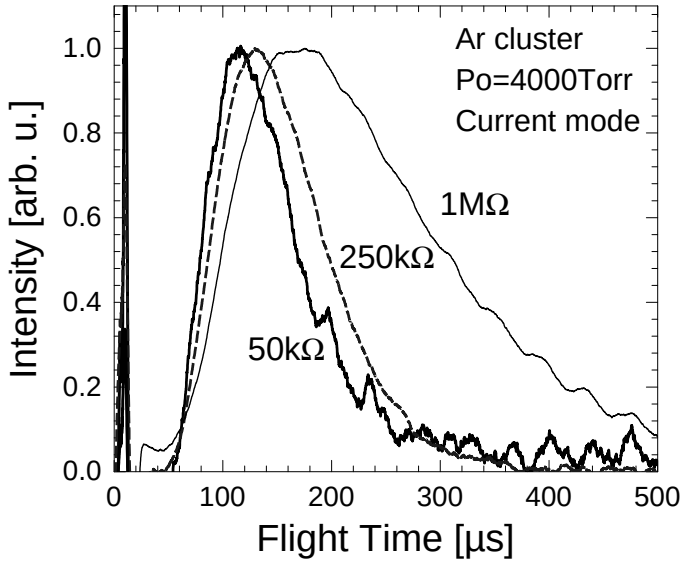

Figure 3.11: TOF spectra measured as an ion current with various terminating resistors.

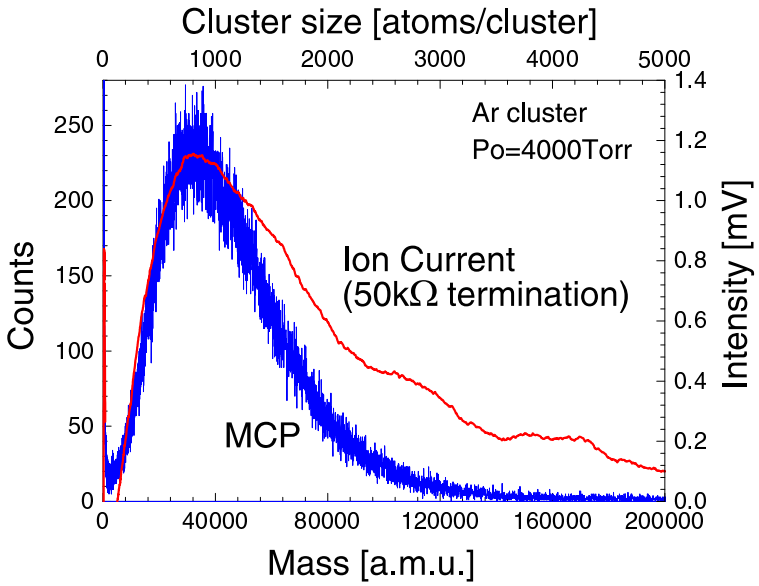

Figure 3.12: TOF mass spectra measured with the MCP and ion current.

were measured as voltages at the terminating resistor with a digital oscilloscope.

Fig. 3.11 shows TOF spectra measured as ion currents with three values of resistors (50kΩ, 250kΩ and 1MΩ). The acceleration voltage was 2.5kV. When the target was terminated with a 1MΩ resistor, the TOF spectra became wide and shifted to longer flight times due to the long time constant. As the flight time was of micro second order, a smaller resistor with low time constant was preferred. However, it caused low output voltage between the ends of the resistor. Considering that the cluster ion current observed at the target was a few tens of nA at an acceleration voltage of a few kV, and the minimum voltage to distinguish the ion signals from electrical noises was about a few mV, a resistance of 50kΩ was selected for the termination.

Fig. 3.12 shows the mass spectra of Ar cluster ion beams measured as an ion current. To compare the cluster size distribution, mass spectra of Ar cluster beams measured with the MCP were also plotted. The acceleration voltage of the cluster ions was 2.5kV. From Fig. 3.12, the peak positions of both spectra were almost the same. However, the intensity in current mode in the large cluster size region was higher than that with MCP. Though it indicated the existence of the quite large clusters, the average cluster size of both spectra showed good agreement.

3.2 Ar cluster beams

3.2.1 Cluster Size Distribution

Small Clusters

From the work presented in the previous sections, it was confirmed that the range of cluster sizes, from small to large, could be measured with the TOF. In this section, properties of an inert gas cluster, specifically Ar cluster, was studied.

Cluster formation in a supersonic beam is a consequence of collisions with isolated atoms. The dimer formation process was expressed in Eq. 2.4, and once the dimers were formed, they act as condensation nuclei for the cluster growth. When a cluster grows by monomer addition, the intensity of the mass spectra decays exponentially with the cluster size n.

To observe the size distribution of small clusters with high mass res-

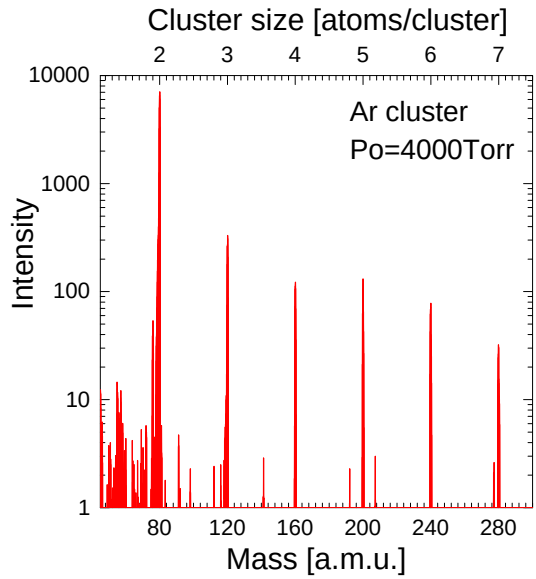

Figure 3.13: Mass spectrum of an Ar cluster beam with a Quadrupole Mass Spectrometer. (Mass ranges 1 to 300 [a.m.u.])

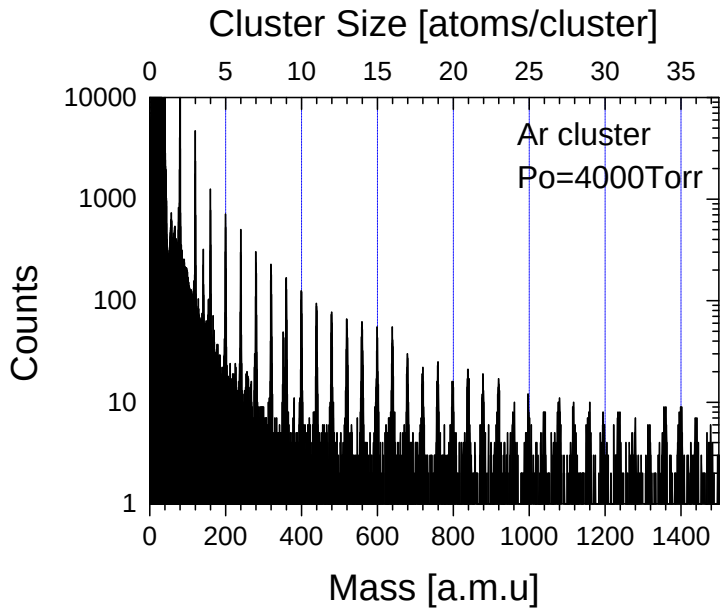

Figure 3.14: Mass spectrum of an Ar cluster beam with the TOF mass spectrometer. (Mass ranges 1 to 1500 [a.m.u.])

olution, a Quadrupole Mass Spectrometer (QMS ; Stanford Research Systems, RGA-300) and a TOF mass spectrometer were used. Fig. 3.13 shows the mass spectra of Ar cluster beams measured with QMS. The ionization of the clusters was performed with 70eV electron bombardment. As the atomic mass of Ar is 40, peaks with an interval of 40 are attributed to Ar_n clusters.

Although the mass resolution of the QMS is much higher than that of the TOF spectrometer, the mass range is limited to less than 300 [a.m.u.], which corresponds to a maximum cluster size of 7 in the case of Ar. To measure the size distribution of larger clusters, TOF mass spectra with sizes of up to 30 were taken as shown in Fig. 3.14. The source pressure was 4500Torr and the ionization energy was 70eV. There were many peaks with an interval of 40 atomic mass units, as that with QMS. The intensity of Ar_n decreased exponentially with cluster size.

It is well known that there is an enhanced abundance of clusters (magic numbers[52]) which is successfully explained in terms of the stability of close packed shell structures. In the case of Xe, the enhancement of the intensity is observed at the sizes of 13, 55 and 147[53, 54], which is attributed to the icosahedral structure. However, no enhancement at these sizes is reported in the case of Ar, and this is also true in our experiments. Ionization of small van der Waals clusters by electron bombardment is accompanied by strong fragmentation or dissociation of the clusters, and consequently, the enhancement of the peak intensity corresponding to the magic number is weakened.

Large Clusters

It is expected that both neutral beam intensity and average cluster size increase with the source gas pressure P_0 from the theoretical points of view. Fig. 3.15 shows TOF mass spectra of large cluster sizes at different P_0 (760 to 3800Torr). The ionization energy and the acceleration energy were 70eV and 1.5keV, respectively.

When P_0 was 760Torr, the cluster beam intensity decayed monotonically with the cluster size starting from monomers. In this condition, the cluster grew by monomer additions. When P_0 was 1500Torr, the decay was no longer exponential, and there was a small maximum at around a size of 500atoms/cluster. With the increase of P_0, the peak position of the size distribution was shifted to larger sizes, and the dip found at the size of several hundreds became more marked. The mass spectrum

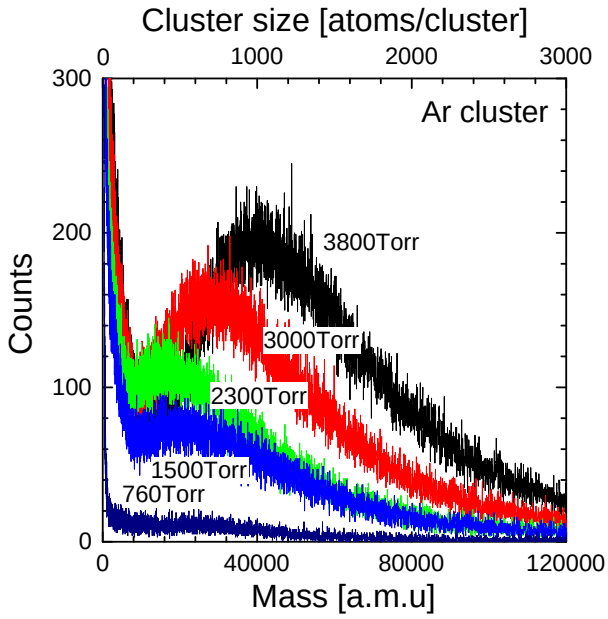

Figure 3.15: TOF spectra of Ar large clusters at different source gas pressures P_0. Cluster size ranges up to 3000 atoms/cluster.

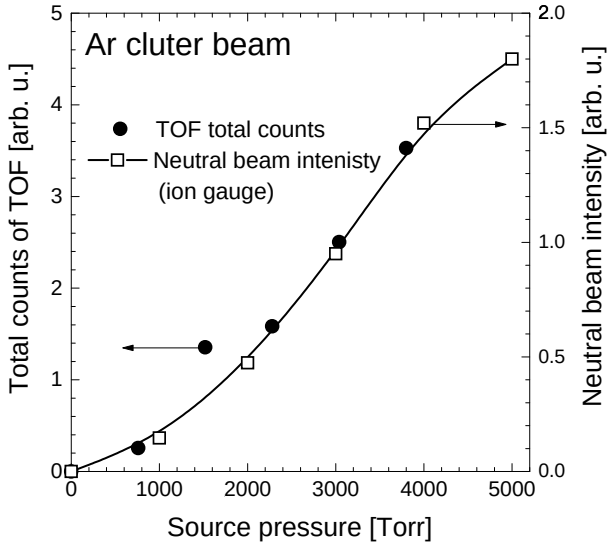

Figure 3.16: Source gas pressure P_0 dependence of the total number of Ar atoms obtained from both an intensity of ion gauge and the integrated counts of TOF mass spectra.

is expressed as the combination of two distributions; exponential decay in the small size region and wide distribution in the large cluster region. When P_0 is high, clusters grow by not only monomer additions but also by cluster-cluster aggregation, which contributes to the broad distribution at large sizes. As described in section 2.1.1, there is a critical cluster size r^* where a cluster grows or dissociates in a supersaturating condition. When a cluster is smaller than r^*, it will evaporate to monomers, whereas a larger one will grow. From the TOF spectra, the critical size r^* is estimated to be around 300atoms/cluster at P_0 of 4500Torr.

Not only the cluster size but also the beam intensity becomes higher with the source gas pressure. Fig. 3.16 shows the pressure (P_0) dependence of neutral beam intensity. The neutral beam intensity was measured by the difference of the ion gauge signal in the TOF chamber when the intervening shutter was opened or closed. Neutral clusters are broken in the ion gauge and thousands of atoms are emitted. Therefore, the total number of atoms in the beam was measured with an ion gauge. From the TOF spectra, the total number of atoms can be obtained from the integration of the counts multiplied by each cluster size.

The neutral beam intensity shows a sudden rise at 2000Torr, and increased monotonically with increasing pressure. Similarly, the total amount of atoms obtained from TOF spectra showed a sudden increase at 1500Torr and it increased with P_0. As indicated by the P_0 dependence of cluster size distribution in Fig. 3.15, the formation of large clusters started at around this pressure. Therefore, the sudden increase of the neutral beam intensity indicated the formation of large clusters. Whether neutral clusters are formed or not can be roughly evaluated from the neutral beam intensity measurement.

3.2.2 Collisions with Residual Gas

In general, collisions with residual gas reduce the beam intensity. In the case of Ar atoms at room temperature, the mean free path is 5.31cm at a pressure of 1×10^{-3} Torr. If the transport length is 5m, the vacuum condition must be better than 1×10^{-5} Torr for the beam to go through without collision with residual gas. The mean free path is strongly dependent on the size of an atom. Since the volume and cross-section of a cluster are much larger than those of a single atom, the mean free path of a large cluster may become small. For example, the cross-section of a cluster with 1000 atoms is a hundred times larger than that of monomer.

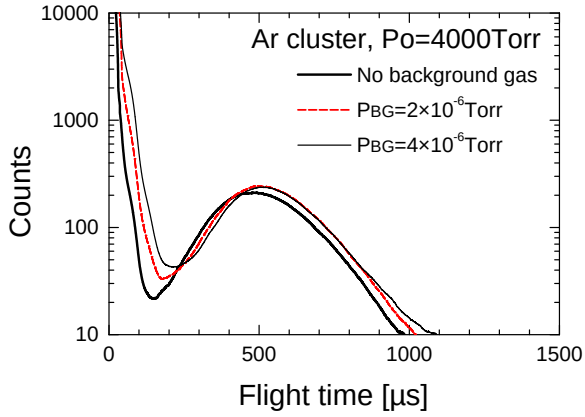

Figure 3.17: TOF spectra with introducing background gas.

If collisions with residual gases influence the beam intensities, the vacuum condition must be two orders of magnitude lower to keep the same mean free path as for single ions.

To investigate the influences of residual gas on the cluster beam intensity, Ar gas was introduced into the TOF vacuum chamber as a background gas. When the background pressure P_{BG} is kept at 4×10^{-6}Torr, the mean free path of clusters with 1000 atoms is expected to be 25cm, which is shorter than the flight length in the TOF chamber (120cm).

Fig. 3.17 shows TOF spectra of Ar cluster beams with or without introducing Ar at 4×10^{-6} and 2×10^{-6}Torr. The acceleration voltage was 1.5kV. There was no significant difference between these spectra. This means that collisions with residual gas do not affect the cluster beam intensity. Since the mass ratio between Ar cluster and background Ar gas is thousands of times higher than that of an Ar-Ar collision, the momentum of a cluster is conserved after the collision. However, this estimation is based on the rigid body system. As cluster constituent atoms are combined weakly with van der Waals forces, the dissociation of a cluster due to collision is probable.

In Fig.3.18, a monomer ion impact with a large cluster is represented by molecular dynamics simulation. Ar monomer ions with energies of 20, 200 or 2000eV collide with an Ar cluster with a size of 688 atoms. These figures are snapshots at 2.14 and 4.29ps after the impacts. The Ar cluster has fcc structure and the Lennard-Jones potential was used for

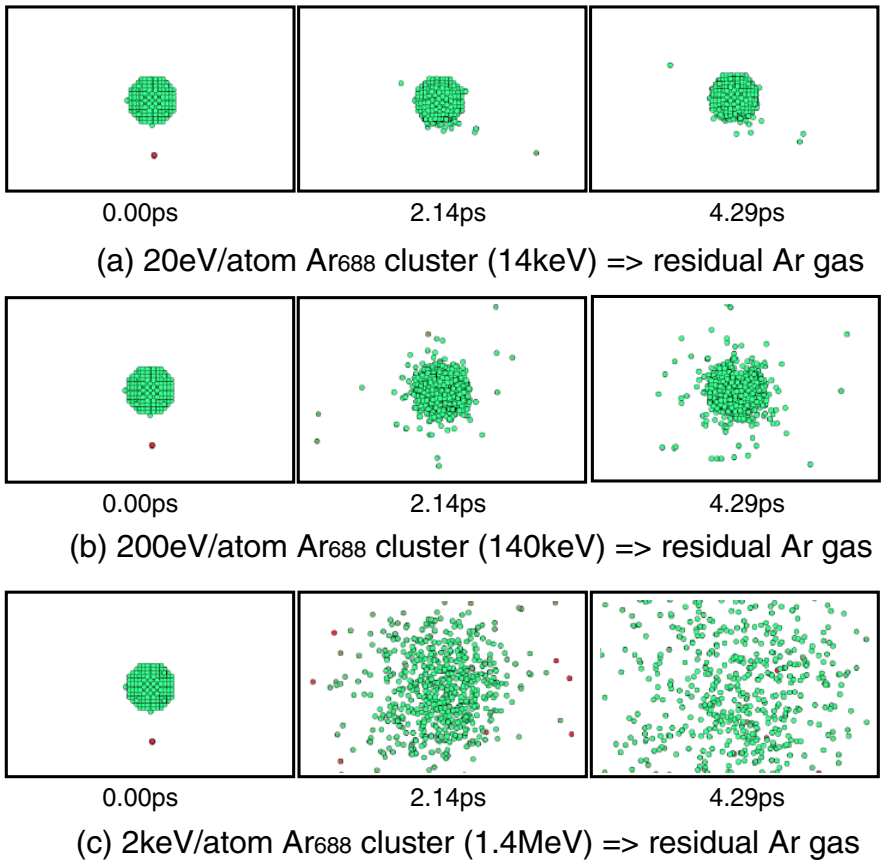

Figure 3.18: Molecular Dynamics simulation of the Ar^+ impact to Ar cluster with energy of 20, 200 or 2000eV. The Ar cluster size was 688.

the Ar-Ar interactions. When an Ar monomer having an energy of 20eV impacted with an Ar cluster (Fig. 3.18(a)), the Ar cluster was stable. Though the Ar ion impact induced collision cascades inside the cluster, the kinetic energy of the projectile ion was relaxed by the cohesive energy of the cluster. The atoms ejected from the cluster were very few.

With increasing kinetic energy of Ar monomers, the number of atoms ejected from the cluster increased. In the case of the 200eV Ar monomer impact (Fig. 3.18(b)), the cohesive energy of the cluster no longer compensated the impinging energy, and this energy was released by the ejection of energetic atoms from the cluster. However, the cluster kept its shape after a 200eV Ar^+ impact. In contrast, Ar cluster was dissociated into single atoms in the case of 2keV Ar^+ impact (Fig. 3.18(c)).

When cluster ions with size of 1000 are accelerated by 2keV and 20keV, each atom has only 2eV and 20eV, respectively. The energy of 2keV is the normal acceleration energy in TOF measurements, and that of 20keV is the acceleration energy mainly used for sputtering and surface smoothing with cluster ions. Therefore, cluster ions with energies of this range are stable even if they collide with the residual gas. However, care must be taken for the background pressure when small or high energy clusters are used because the cohesive force becomes smaller with decreasing cluster size.

3.2.3 Ionization Efficiency of Clusters

To Obtain Higher Cluster Ion Current

A cluster ion can transport larger number of atoms in proportion to its size than does a single ion. When cluster ion current with a cluster size of 1000 is 1μA, it has the same equivalent ability as a 1mA monomer ion beam in transporting atoms. However, a high cluster ion current is required for surface smoothing or thin film formation over a large area. For example, surface smoothing of diamond films requires an ion dose of 1×10^{17}ions/cm^2. When the irradiation area is 10cm^2 and cluster ion current density is 100nA/cm^2, the process requires 44 hours. Therefore, improvement of the equipment to obtain much higher cluster currents is necessary for practical applications using cluster ion beams.

The simplest way to get a higher ion current is to increase the ionization electron emission current. Fig. 3.19 shows the emission current dependence of Ar monomer and cluster ion current. The ionization bias of electrons V_e was 300V and the source pressure for cluster formation

was 4000Torr. A monomer ion beam was formed from an ambient gas in the ionizing chamber. From Fig. 3.19, the monomer ion current increased linearly with the electron emission current, whereas the cluster ion current saturated at 400nA. The probable reasons for this saturation are the following:

1. **Space Charge Effect**
   Space charge effect limits the maximum ion current. The space charge limited current J between two parallel electrodes is expressed as follows.
   $$J = \frac{4\epsilon_0}{9}\sqrt{\frac{2q}{m}}\frac{V^{\frac{3}{2}}}{d^2} \tag{3.9}$$
   where m, q, ϵ_0, d and V are mass, charge, the dielectric constant in vacuum, the distance between the two electrodes and the voltage across the electrodes, respectively. As the mass of clusters is thousands of times larger than that of monomers, J is lower than that of monomer ions at same extraction voltage.

2. **Dissociation of Clusters**
   It is probable that cluster ions are dissociated by impacts of energetic particles. As large amounts of monomer ions are involved in the beam, the collisions between cluster ions and energetic monomer ions are significant.

3. **Lack of Neutral Clusters**
   As the cross-section of a cluster is much larger than that of a monomer (typically a hundred times), the cluster will be preferentially ionized by collisions with ionization electrons. Also the number of clusters is less than a few percent compared with Ar monomers, therefore, a lack of available neutral clusters appears sooner than in the case for monomers.

If the space charge effect is the reason for the saturation, the ion current must increase at higher extraction voltage. However, the cluster ion current has saturated similarly in spite of a high extraction voltage. If the dissociation of clusters is the reason, the cluster ion current must decrease with the increase of the extraction voltage due to the energetic monomer ion impacts, which is also not the case. Therefore, the lack of neutral clusters is thought to be the probable reason for the saturation.

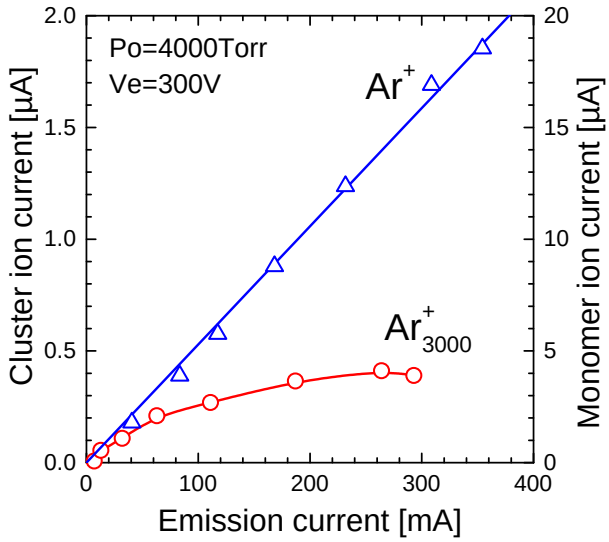

Figure 3.19: Cluster and monomer ion currents versus electron emission current.

Experimental Procedure

To confirm that the saturation can be attributed to the lack of neutral clusters, a two-stage ionization experiment was performed. A schematic diagram of the experimental setup is shown in Fig. 3.20. The TOF chamber was connected to the end of the 30keV gas cluster ion beam apparatus. The pre-ionization was performed at (A) in the 30keV apparatus, and pre-ionized clusters were removed from the beam axis by deflectors. As a result, only residual neutral clusters entered the TOF chamber and these were subsequently ionized at (B) in the TOF chamber. Thus, mass spectra of residual neutral clusters can be measured. From the difference between TOF mass spectra with and without pre-ionization, the number of neutral clusters ionized at position (A) can be obtained. The source gas pressure was 4000Torr and the electron energy of the pre-ionization was 300eV. The emission current of pre-ionization was changed from 0mA (without ionization) to 260mA. Neutral beam intensities were also measured from the difference in the vacuum condition of the TOF chamber when the shutter was opened or closed.

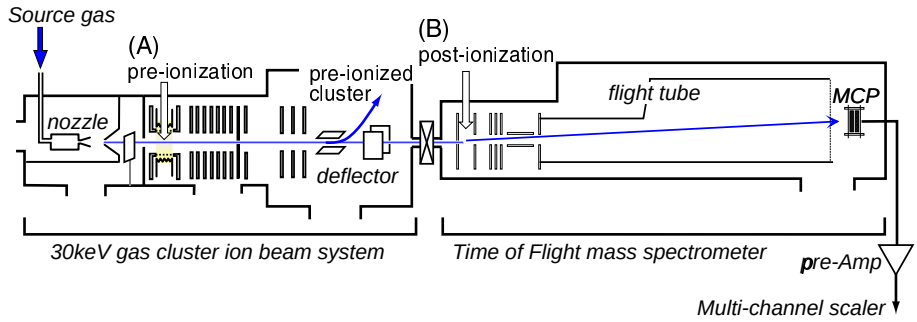

Figure 3.20: Schematic diagram of the TOF mass spectrometer connected to the 30keV gas cluster ion beam apparatus.

Ionization Efficiency

Fig. 3.21 shows the emission current dependence of the neutral beam intensity measured with the ion gauge. The neutral beam intensity decreased monotonically with the emission current. Even when the extraction voltage was increased from 0 to 500V, no marked change was observed. It should be noted that if the space charge effect is the main reason for the saturation of ion current, the neutral beam intensity should not decrease with the emission current.

Time of flight mass spectra at several emission currents are shown in Fig. 3.22. The TOF spectrum without ionization is displayed as a thick line. The intensity of cluster ions decreased with increasing emission current, and the total amounts of particles obtained from integration of these TOF spectra were also plotted in Fig. 3.21. The decay of the total number of particles of TOF showed good agreement with neutral beam intensity measurements.

When the emission current was 260mA, the intensity at a cluster size of 2000 was half of the value without ionization. This means that the ionization efficiency of clusters with a size of 2000 was almost 50%. The ionization efficiency for all sizes of cluster was obtained from $(I_0 - I_e)/I_0$, where I_0 and I_e are the neutral beam intensity and the residual beam intensity after pre-ionization, respectively.

Fig. 3.23 shows the cluster size dependence of the ionization efficiency. Each line was fitted by $k \cdot n^{\frac{2}{3}}$ (k is an arbitrary constant and n is the cluster size) displayed as a dotted line. The ionization efficiency increased with cluster size regardless of the emission current. As the cross-section

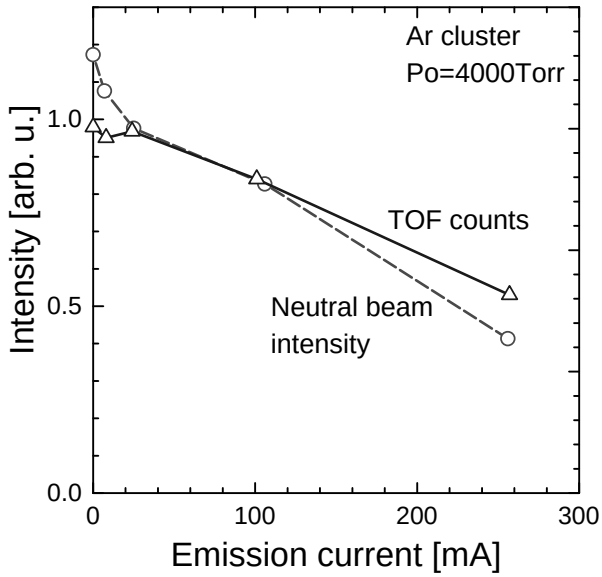

Figure 3.21: Emission current dependence of neutral beam intensity and total number of atoms in the beam obtained from the integration of the TOF spectra.

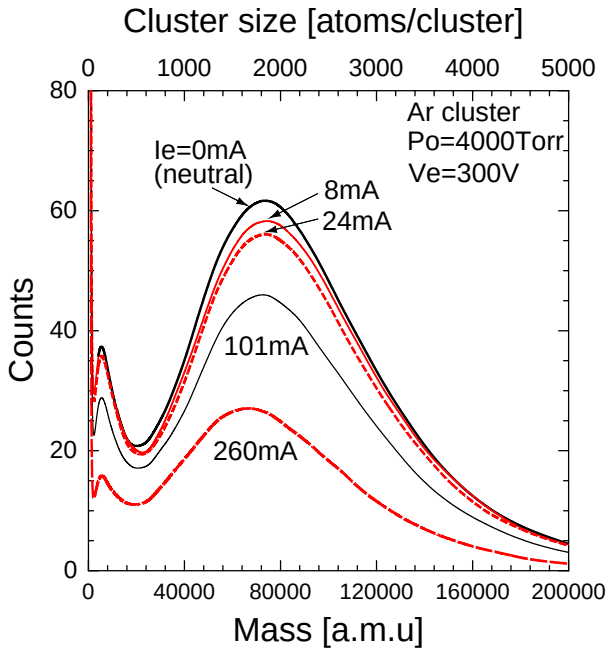

Figure 3.22: TOF mass spectra of residual neutral clusters under different pre-ionization electron current.

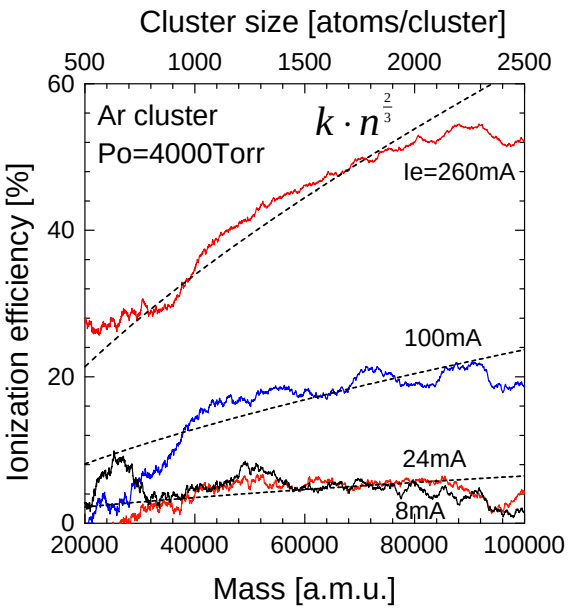

Figure 3.23: Cluster size dependence of the ionization efficiencies.

of a cluster with size of n was proportional to $n^{\frac{2}{3}}$, the probability of collisions with ionization electrons was $n^{\frac{2}{3}}$ times higher than that in the case of monomers.

It has been reported that the ionization potential of clusters decreases gradually with size[55]. In table 3.1, ionization potentials were arranged according to the cluster size. The difference between the ionization potentials of isolated Ar (15.75eV)[55] and bulk Ar (13.9eV)[55] is only 1.85eV, therefore, the cluster size dependence of ionization potential is negligible when the ionization energy was 300eV.

From these results, it is made clear that the ionization efficiency of clusters is much higher than that of monomer ions. Therefore, neutral clusters are preferentially ionized compared with monomers, and the cluster ion current saturates because of the lack of neutral clusters. To obtain higher cluster ion current, a more intense neutral cluster beam is necessary in the 30keV gas cluster ion beam equipment.

Table 3.1: The ionization potentials of Ar clusters obtained from photo ionization curve[55].

cluster size n	ionization potential Ar (eV)
1	15.75
2	14.52
3	14.34
4	14.36
5	14.34
6	14.34
7	14.34
8	14.32
9	14.31
10	14.29
20	14.21
30	14.27
∞	13.90

3.3 Reactive and Mixed Cluster Beams

3.3.1 Oxygen Cluster Beams

An Ar cluster shows many characteristic irradiation effects due to the dense energy deposition at a local area. These non-linear effects are physical in origin. When reactive gases are supplied from the source, enhancements of these irradiation effects by chemical reactions are expected.

So far, reactive gas clusters of O_2, NO, NO_2, N_2O, CO_2 and SF_6 have been formed[56]. Among them, SF_6 and O_2 cluster ion beams are frequently used in many applications such as etching of Si and diamond films, the formation of oxide films and as the primary ion for Secondary Ion Mass Spectrometry (SIMS) analysis. For example, Indium Tin Oxide (ITO) films with high transparency (over 80%) and low resistivity ($1.5 \times 10^{-4}\Omega$·cm) were fabricated with O_2 cluster ion beam assisted deposition[57]. Since the chemical reactions are affected strongly by the energy density on the target, the cluster size distribution, which is re-

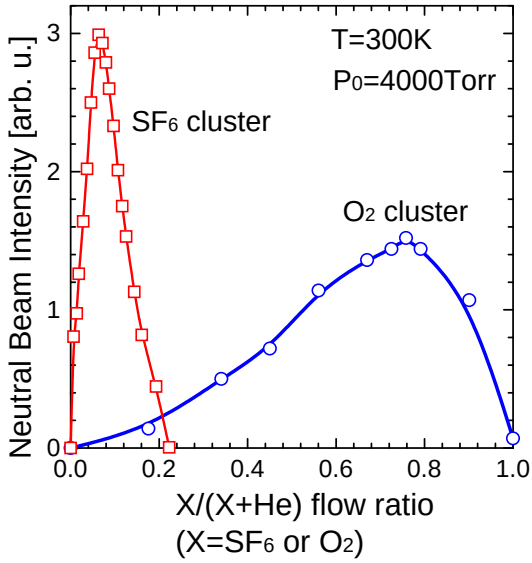

Figure 3.24: Neutral beam intensity versus mole fractions of reactive gases mixed with He gas.

sponsible for the energy per atom of cluster, is significant. In this section, the formation and the cluster size distributions of reactive clusters are discussed.

Formation of Reactive Cluster Beams

A molecule has degrees of freedom for rotation and vibration in addition to the translational energy. During a supersonic expansion, the rotational temperature (T_{rot}) and the vibrational temperature (T_{vib}) are decreased by energy transfer to the translational one (T_{trans}) through numerous collisions. In general, the energy transfer cross-sections decrease in the order: $E_{trans} \rightarrow E_{trans}$, $E_{rot} \rightarrow E_{trans}$ and $E_{vib} \rightarrow E_{trans}$, where E_{trans}, E_{rot} and E_{vib} are the translational, the rotational and the vibrational energy, respectively. Therefore, there is a sequence of $T_{vib} > T_{rot} > T_{trans}$. As O_2 and SF_6 molecules have large rotational and vibrational energies, the cooling effect in the supersonic expansion of pure O_2 or SF_6 is insufficient for the formation of an intense cluster beam.

To form an intense cluster beam, He gas was mixed with a reactive gas and used as a carrier gas. Fig. 3.24 shows the relation of the neutral beam intensity of O_2 and SF_6 versus the mole fractions, [X]/[He+X] (X=O_2

or SF_6). Since the SF_6 molecule has many vibration modes compared with the O_2 molecule, it needs a high fraction of He mixing to obtain an intense cluster beam. The maximum intensity was obtained at a mole fraction of SF_6 (f_{SF_6}) of 5%, whereas that of O_2 (f_{O_2}) was 75%. Valente and coworkers generated a SF_6 cluster beam by the co-expansion of SF_6 and an inert gas thorough a Laval nozzle with f_{SF_6} of 10%[58]. This result agrees well with our results. One may expect containment of He gas in the reactive cluster beam. However, He atoms were not observed in the TOF or QMS mass spectra. Since He atoms are moving very fast and the van der Waals force of He is very low, He atoms are evacuated in the source chamber without forming a He cluster beam.

Mass spectra of O_2 Clusters with TOF

Fig. 3.25 shows TOF spectra of small O_2 clusters. The O_2 cluster size ranged from 1 to 45atoms. He gas was mixed with oxygen at 30% and the source pressure was kept at 4000Torr. The ionization electron bias V_e was 70V. In a similar manner to the Ar clusters, the intensity of each O_2 peak decreased exponentially with the cluster size. There were also two series of peaks in the spectra. One had an interval of 32[a.m.u.] and another was located exactly in the middle of the first series. As the atomic mass of oxygen is 16 [a.m.u.], the former series of peaks with high intensities was attributed to clusters with even numbers of oxygen atoms expressed as $(O_2)_n$. The latter series of peaks with lower intensities were attributed to the clusters with odd numbers of oxygen atoms expressed as $(O_2)_nO$. As the ionization energy was 70eV, the dissociation of oxygen molecules caused these odd numbered clusters to form.

Two dissociation processes of oxygen clusters are described as follows.

$$(O_2)_n \rightarrow (O_2)_{n-1} + O_2 \tag{3.10}$$

$$(O_2)_n \rightarrow (O_2)_{n-1} \cdot O + O \tag{3.11}$$

It is reported that the O_2 evaporation from a cluster expressed in Eq.3.10 is preferred over oxygen atom evaporation[59]. Therefore, the intensity of O_2 clusters with odd numbers of oxygen atoms $(O_2)_n \cdot O^+$ was much lower than that with even numbers $(O_2)_n^+$ [59].

Time of flight spectra of large O_2 clusters are shown in Fig. 3.26. The cluster size ranged from 1 to 6250. The total pressure and ionization energy were 4000Torr and 70eV, respectively. There was a first peak at a cluster size of 1500 and also a shoulder was found at around a size of

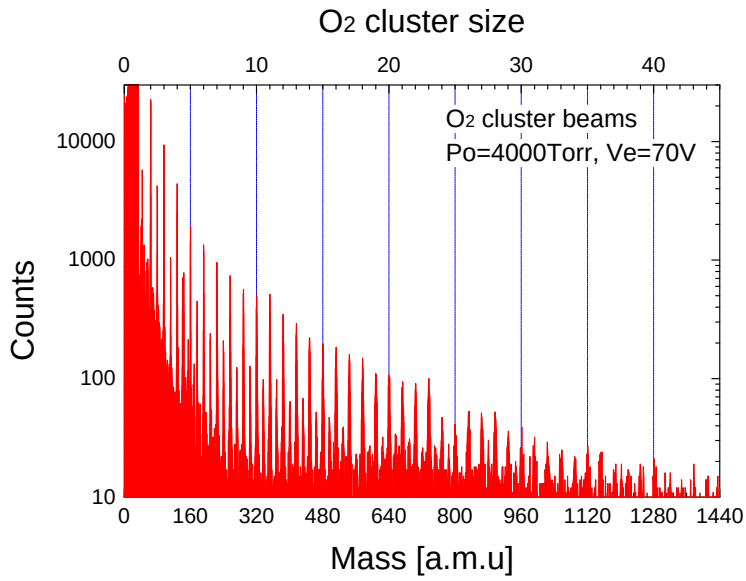

Figure 3.25: TOF mass spectrum of small O_2 cluster beams.

3000. The mass spectrum was separated in two Gaussian distributions that had peaks at cluster sizes of 1500 and 3000. In the mass spectrometer which uses ion charge for the mass separation, it is not possible to distinguish between ions with the same mass to charge ratio. There are other possibilities for the origin of the two peaks, i.e., fragmentation to smaller sizes and the presence of clusters having double charge. The multiply charged clusters are discussed in section 3.4.

3.3.2 Ar and Oxygen Mixed Cluster Beams

The reactivity of a cluster changes according to its electronic and geometric structure. Cluster size is the only parameter available to change these structures in the case of monatomic clusters. On the other hand, an additional parameter, the 'composition' of the elements, gives different properties to complex clusters. For example, reactivity and work function of an alloy cluster change according to the composition of the elements[60].

Further, the reactivity of clusters in the impact processes can be changed by the composition of the reactive and non-reactive elements in complex clusters. In this study, Ar and O_2 were mixed and complex

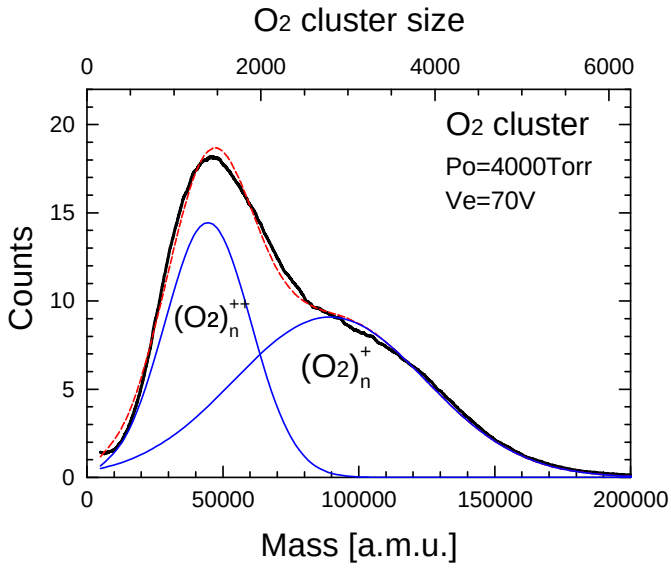

Figure 3.26: TOF mass spectrum of large O_2 cluster beams.

cluster beams were formed. The ratio of Ar to O_2 affect both sputtering yield and surface roughness. The formation of clusters from mixed gas is also interesting from the aspect of whether two kinds of monatomic clusters are formed independently or complex clusters involving two elements are formed. In this section, the cluster size distribution was measured with quadrupole mass spectrometer and TOF mass spectrometer, and the formation of complex clusters is discussed.

Formation of $Ar_m(O_2)_n$ Complex Clusters

Ar and oxygen gases were introduced to the nozzle via two mass flow controllers (Tylan general, MFC-260). The flow fraction of Ar (f_{Ar}) and O_2 (f_{O_2}) were varied using the mass flow controllers. The total pressure in the nozzle was kept at 4000Torr. The mole fractions of Ar and O_2 in the cluster beam were measured with a QMS installed in the target chamber. Also, the neutral beam intensity of the complex gas cluster beam was measured with an ion gauge. The ion gauge measured only the total intensity of the cluster beam.

Fig. 3.27 shows the f_{O_2} dependence of the neutral beam intensity. Since inert gases have a high specific heat ratio (γ), they were used as carrier gas. In the case of He, there was little He gas left in the beam.

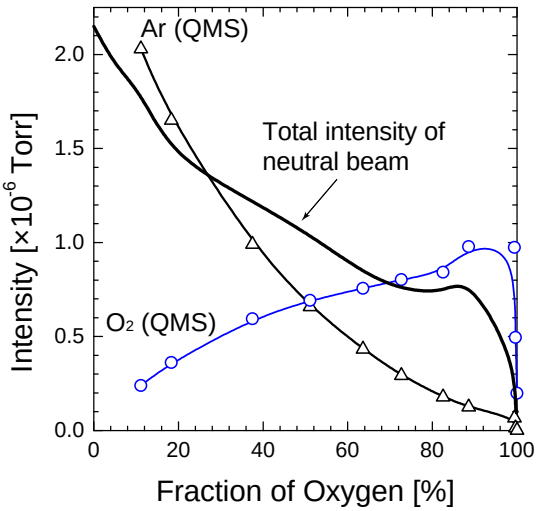

Figure 3.27: O_2 flow fraction dependence upon the neutral beam intensity and QMS signals of Ar and O_2.

However, Ar clusters were formed because of their high van der Waals force.

The neutral beam intensity of the mixed gas (indicated by the thick line) decreased with increasing f_{O_2}. As the O_2 intensity measured with QMS was very low at $f_{O_2} \leq 20\%$, Ar clusters were preferentially generated in this region. This decrease of the neutral beam intensity was due to the reduction of Ar flow, i.e. Ar only formed Ar_n in this region. With a further increase in f_{O_2}, the intensity of Ar and O_2 crossed at around an f_{O_2} fraction of 50%. Both neutral beam intensity and O_2 intensity had a maximum value at an f_{O_2} of 90%. In this region Ar atoms were consumed as a carrier gas. In the case of the He gas mixture shown in Fig. 3.24, the neutral intensity of O_2 cluster beam had an maximum value at f_{O_2} of 75%. This indicates that the cooling effect of Ar was higher than that of He because of the larger mass[61].

Fig. 3.28 shows QMS spectra for (a) pure Ar, (b) mixed Ar/O_2 and (c) pure O_2 cluster beams. The mole fraction of oxygen was 90% in the case of the Ar/O_2 mixtures. Although pure Ar and O_2 clusters had peaks at an interval of their atomic mass, the mass spectra of the mixed cluster beams had further peaks in addition to Ar_n and $(O_2)_n$ peaks. The possible combinations of clusters such as, Ar_m, $(O_2)_n$ and Ar_mO_n

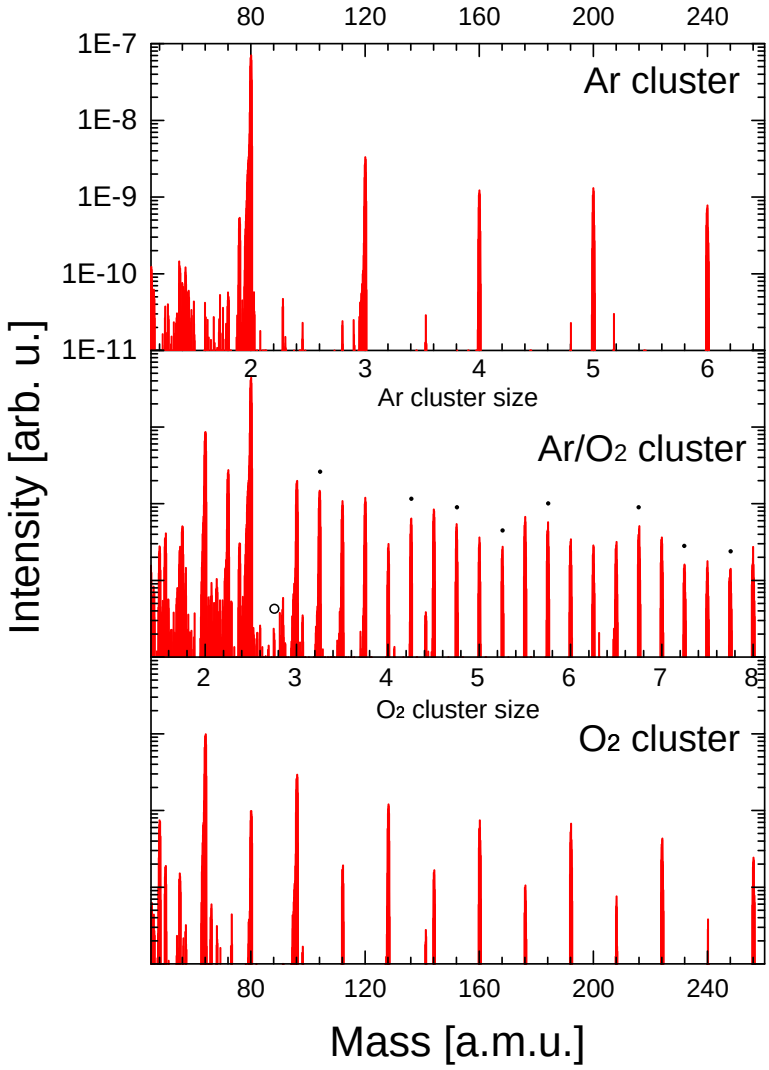

Figure 3.28: QMS spectra of pure Ar, O_2 cluster beams and Ar/O_2 mixed cluster beams. f_{O_2} was 5% in the case of Ar/O_2 cluster beam.

Table 3.2: Combination of $Ar_m(O_2)_n$ with various atomic masses. ($m = 0 \sim 5$, $n = 0 \sim 8$).

Mass	Ion species		
48			
56			
64	$(O_2)_2$		
72	$Ar_1(O_2)_1$		
80	Ar_2		
88			
96	$(O_2)_3$		
104	$Ar_1(O_2)_2$		
112	$Ar_2(O_2)_1$	$(O_2)_3O$	
120	Ar_3		
128	$(O_2)_4$		
136	$Ar_1(O_2)_3$		
144	$Ar_2(O_2)_2$	$(O_2)_4O$	
152	$Ar_3(O_2)_1$		
160	Ar_4	$(O_2)_5$	
168	$Ar_1(O_2)_4$		
176	$Ar_2(O_2)_3$	$(O_2)_5O$	
184	$Ar_3(O_2)_2$		
192	$Ar_4(O_2)_1$	$(O_2)_6$	
200	Ar_5	$Ar_1(O_2)_5$	
208	$Ar_2(O_2)_4$	$(O_2)_6O$	
216	$Ar_3(O_2)_3$		
224	$Ar_4(O_2)_2$	$(O_2)_7$	
232	$Ar_5(O_2)_1$	$Ar_1(O_2)_6$	
240	Ar_6	$Ar_2(O_2)_5$	$(O_2)_7O$
248	$Ar_3(O_2)_4$		
256	$Ar_4(O_2)_3$	$(O_2)_8$	
264	$Ar_5(O_2)_2$	$Ar_1(O_2)_7$	

($m = 0 \sim 6, n = 0 \sim 15$) were arranged according to their atomic masses in table 3.2. As the atomic masses of Ar and oxygen are 40 and 16, respectively, the clusters with atomic mass of 72, 104, 136, 152, 168, 184, 216, 232, 264 and 296 cannot be composed by Ar_m, $(O_2)_n$ or $(O_2)_n$·O clusters. This is evidence of the formation of $Ar_m(O_2)_n$ complex clusters. These peaks were marked by solid dots in Fig.3.28.

Taking into account the complex clusters of Ar with odd numbers of oxygen atoms ($Ar_m(O_2)_n$·O), the peak of $Ar(O_2)O$ should appear at 88[a.m.u.]. From Fig. 3.28(b), the abundance of $Ar(O_2)O$ marked by an open circle was very low, which indicated that the number of complex clusters with odd numbers of oxygen atoms was negligible.

Flow Fraction Dependence of $\mathbf{Ar}_m(\mathbf{O}_2)_n$

Figure 3.29 shows TOF mass spectra of Ar/O_2 mixed cluster beams at several flow fractions of oxygen (f_{O_2}=[O_2]/[Ar+O_2]). When f_{O_2} was 95%, the intensity of $(O_2)_n$ clusters decreased monotonically with the mass interval of 32[a.m.u.]. The peaks of the dissociated $(O_2)_n$O clusters were also observed as in Fig.3.25. In the case of an f_{O_2} of 50%, there were many peaks with an interval of 8 [a.m.u.], which were attributed to complex cluster formation. However, there were bunches of peaks with mass ranges of 32 [a.m.u.]. It suggests that the O_2 cluster was the dominant species in the cluster beam. On the other hand, when f_{O_2} was 5%, the width of the peak bunches changed from 32 to 40 [a.m.u.], and this means that Ar cluster ions were dominant.

From these results, it is evident that the nature of the cluster nuclei changes with the flow fraction. It has been reported that Ar_3^+ and $(O_2)_3^+$ are cluster nuclei in the case of monatomic clusters [62, 63, 64]. Therefore, changes of the intensity of both Ar_3^+, $(O_2)_3^+$ and their composites in the mixed cluster beam were studied. The f_{O_2} dependence of the intensity of $Ar_3(O_2)_n$ and $Ar_m(O_2)_3$ ($m, n = 0 \sim 4$) are shown in Fig. 3.30 and 3.31, respectively. In the case of $Ar_3(O_2)_n$, as shown in Fig. 3.30, the peak position was shifted to higher f_{O_2} with increasing number of oxygen atoms n. In contrast, from Fig. 3.31, the peak position of $Ar_m(O_2)_3$ was shifted to lower f_{O_2} with increasing number of Ar atoms m. The increase of intensity of the atomic masses 176 and 256 in the high f_{O_2} region was due to the increase of oxygen clusters as O_{11} and $(O_2)_8$, respectively. The intensity of the complex clusters which have large numbers of oxygen atoms increased with f_{O_2}.

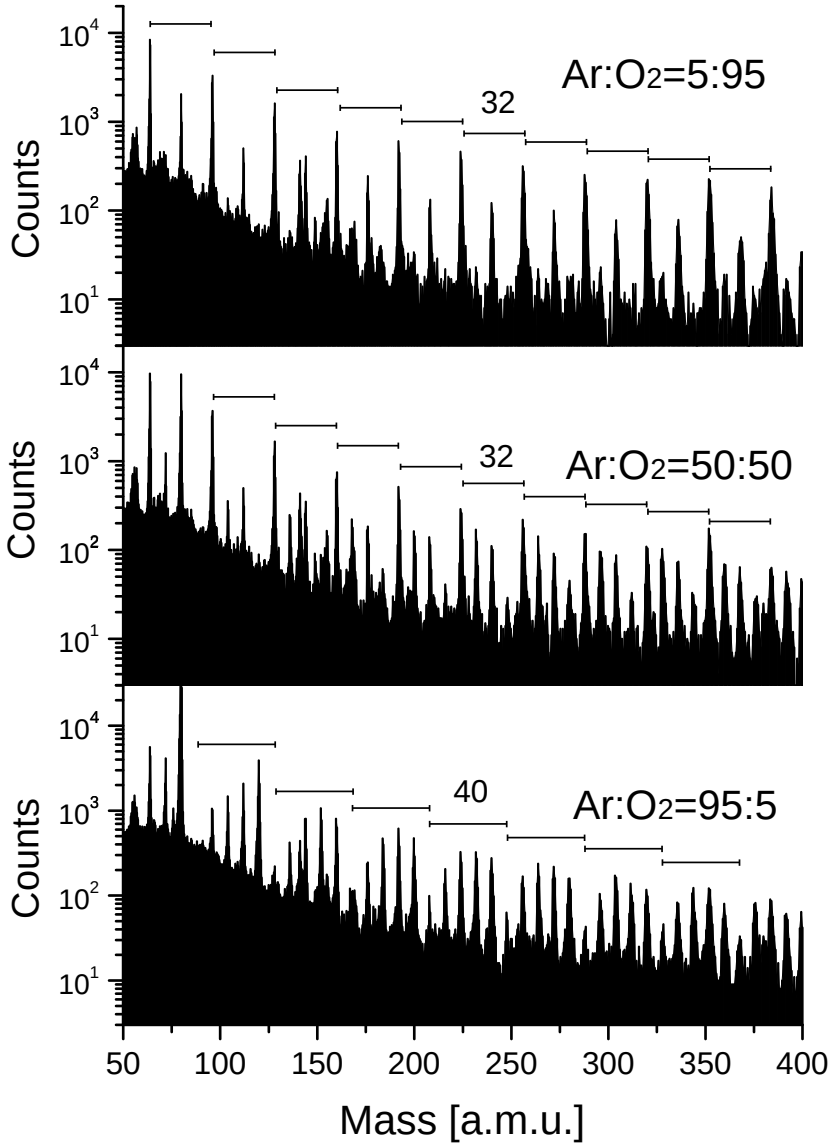

Figure 3.29: TOF mass spectra of Ar/O_2 mixed cluster beams at several flow fractions of oxygen.

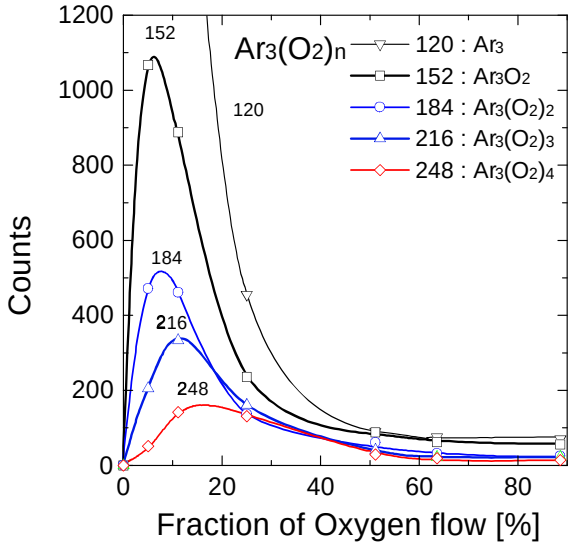

Figure 3.30: f_{O_2} dependence of $Ar_3(O_2)_n$ intensity obtained from TOF spectra.

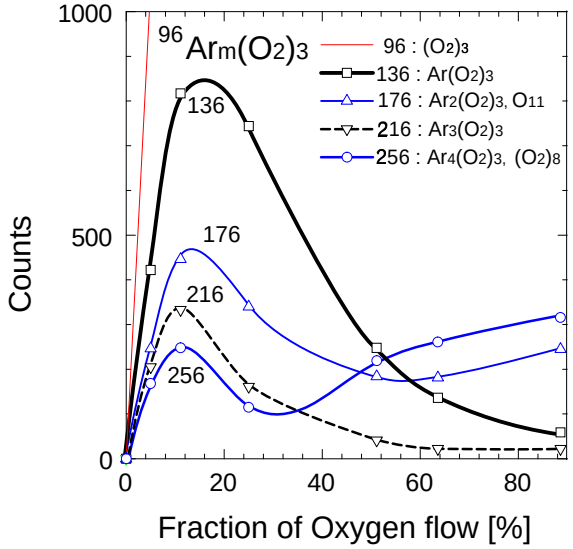

Figure 3.31: f_{O_2} dependence of $Ar_m(O_2)_3$ intensity obtained from TOF spectra.

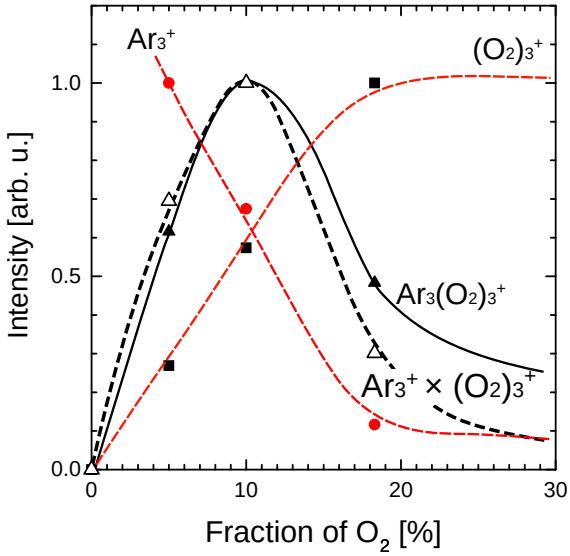

Figure 3.32: The f_{O_2} dependence of the normalized intensities of Ar_3^+, $(O_2)_3^+$, $Ar_3(O_2)_3^+$ and $Ar_3^+ \times (O_2)_3^+$mass spectra on f_{O_2}.

Figure 3.32 shows the f_{O_2} dependence of the normalized intensities of Ar_3^+, $(O_2)_3^+$ and $Ar_3(O_2)_3^+$. To allow comparison with $Ar_3(O_2)_3^+$, the intensity of the Ar_3^+ was multiplied by $(O_2)_3^+$, and the resulting normalized intensity of $Ar_3^+ \times (O_2)_3^+$ was plotted in Fig. 3.32. Each intensity was normalized to the maximum value. The intensity of Ar_3^+ decreased monotonically with f_{O_2}, whereas that of $(O_2)_3^+$ increased, and that of $Ar_3(O_2)_3^+$ had a maximum at f_{O_2} of 10%. The curve of $Ar_3^+ \times (O_2)_3^+$ showed the same tendency as for the $Ar_3(O_2)_3^+$. It indicates that the intensity of complex clusters can be predicted from the intensity of the monatomic clusters of Ar_m and $(O_2)_n$, and suggests homogeneous cluster formation. In the case of metal clusters of Li and Na, homogeneous mixing of Li_nNa_m which follows a binomial distribution has been reported[65].

3.4 Multiply Charged Cluster Ions

When a neutral beam is bombarded by electrons of sufficient energy, not only single but also multiply charged clusters are generated. However, the fragmentation of clusters is also probable because the atoms in the cluster are weakly bound by van der Waals forces.

Fig. 3.33 shows TOF mass spectra of O_2 clusters ionized by different ionization electron energies (E_i). The electron emission current was fixed at 0.2mA. When E_i was 40eV, only one peak around a cluster size of 4000 existed in the mass spectrum. However, with increasing E_i, a second peak around a cluster size of 2000 appeared in the lower mass part of the TOF spectrum, which was exactly half the size of the former peak. This second peak grew with E_i and, subsequently, its intensity exceeded that of the first peak at E_i of 100eV. In addition, another two shoulders appeared at around cluster sizes of 1400 and 1000 with E_i of 100eV. These sizes corresponded to one third and one fourth of the original cluster peak at 4000 atoms/cluster, and it suggested that multiply charged clusters with three or four charges were being generated.

From these results, it is probable that the smaller size of the peaks originates from the multiply charged large clusters. However, the mass spectrometer measures mass to charge ratio, and it is not possible to distinguish between singly charged cluster ions with size n and doubly charged cluster ions with size $2n$. On the other hand, a doubly charged cluster ion of size $(2n+1)$ will appear in a mass spectrum halfway between the singly charged cluster of size n and $(n+1)$. Therefore, the appearance of the peak between singly charged clusters is evidence for the formation of doubly charged cluster ions.

Fig. 3.34 shows a TOF spectrum of O_2 clusters with size between 240 and 560 atoms/cluster. Due to the dissociation of the O_2 molecule, the TOF spectrum became complicated. In Fig. 3.34, there existed peaks halfway between singly charged $(O_2)_n^+$ and $(O_2)_nO^+$. These peaks corresponded to the doubly charged $(O_2)_{2n}O^{2+}$, and were observed as $(O_2)_nO_{0.5}^+$ in the TOF mass spectra. This is evidence for the generation of doubly charged O_2 cluster ions.

When there are two charges present on a cluster and the Coulomb repulsion between them is higher than the cohesive binding force of the cluster, it leads to an immediate dissociation of the cluster ions[66, 67]. This process is termed a Coulomb explosion. With decreasing cluster size, the cohesive force becomes low and the Coulomb repulsion force between charges becomes high. Thus, there is a certain critical size for the appearance of multiply charged clusters. In the case of O_2, the appearance size of doubly charged cluster ions was reported as 92[68]. It is proposed from the liquid drop model that the appearance size of doubly

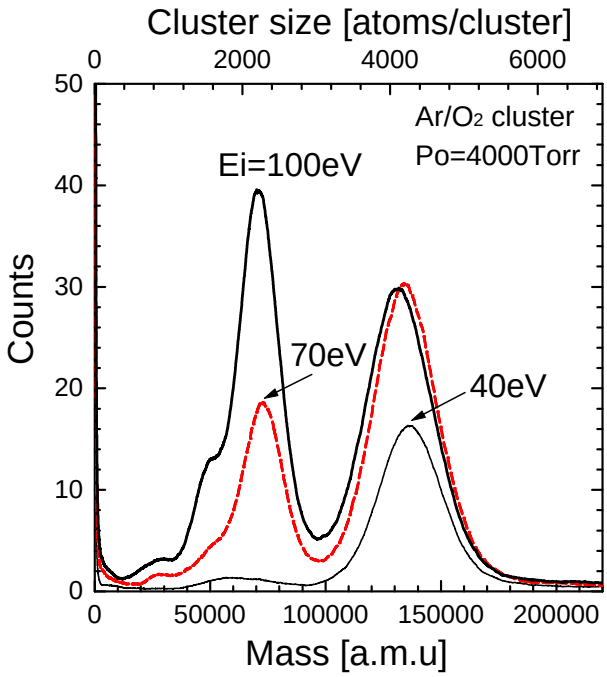

Figure 3.33: Ionization energy dependence of TOF mass spectra of O_2 cluster beams.

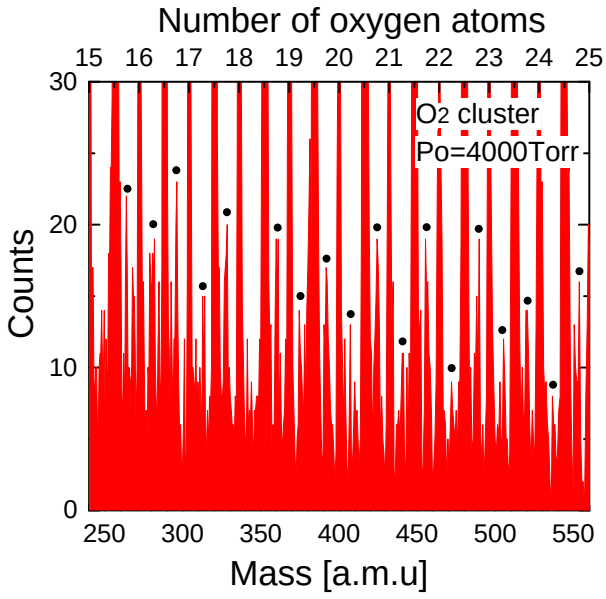

Figure 3.34: Doubly charged O_2 cluster ions of $(O_2)^{2+}_{2n+1}$

charged clusters (n_2) has a relation described as follows[69];

$$n_2 v^{\frac{1}{3}} \approx \frac{1}{T_b} \tag{3.12}$$

where v and T_b are atomic volume and boiling temperature, respectively. As Ar and oxygen have almost same $T_b v^{\frac{1}{3}}$ value and ionization potential, the threshold energy and the tendency for multiply charged cluster ion formation are similar.

Mark and co-workers reported that the threshold energy for the generation of doubly charged O_2 cluster ions was shifted to a lower value (40eV) than that of single oxygen atoms O^{2+} (52.7eV) [68]. This 'red shift' of the threshold energy was also observed in multiply charged Ar[70], Kr[71], Xe[72], N_2[73] and Hg_n cluster ions[74]. If multiple ionization occurs as the result of a single collision of an electron with one Ar atom and produces a $Ar_{n-1}{\cdot}Ar^{2+}$ followed by subsequent charge exchange process, the remarkable decrease of the threshold energy cannot be explained. The threshold energy should be the same under this assumption. Therefore, a doubly charged cluster is produced by two sequential single ionization events of one incoming electron at two different atoms in the cluster.

This ionization process explains the high cross-sections of multiply charged cluster ions. Here it is assumed that the fragmentation of the original cluster into two clusters of the same size is a very rare event, so that the peak at lower mass size in Fig. 3.33 was caused by doubly charged clusters. From Fig. 3.33, the ratio of $(O_2)_n^{2+}/(O_2)_n^{+}$ with an ionization energy of 100eV was roughly the same, which indicated a similar ionization cross-section of singly and doubly charged clusters. Such a large fraction of doubly charged ions is not observed for doubly charged monomer ions (typically 10%).

The multiply charged cluster is problematic for basic research because the mass spectrometer cannot separate ions with same mass to charge ratio. However, the acceleration power supply or the insulator requirements can be reduced by the use of doubly charged cluster ions because a half of the acceleration voltage gives equivalently the same energy as the monomer ion.

3.5 Summary

Properties of cluster beams were studied with a high resolution TOF mass spectrometer. The formation and the size distributions of inert, reac-

tive and complex cluster beams were discussed. Collision cross-sections, ionization efficiency and multiply charged clusters were also discussed. These considerations have great importance for the development of intense cluster ion beam equipment. The following are summaries of this chapter.

1. Mass resolution ($m/\Delta m$) of the linear type TOF was 500 and that of reflectron TOF was 1500. To perform a perpendicular extraction of large clusters, the initial kinetic energy of a cluster must be compensated with a deflector or a change of ionizer location.

2. The relative detection rate of the MCP was degraded due to the reduction of the secondary electron emission by low velocity cluster ions. Therefore, it decreased exponentially with cluster size. The as-measured TOF spectra can be compensated with the detection probability function on the ion velocity.

3. Both cluster beam intensity and average size increased with the source gas pressure, and neutral clusters started to be generated from 1500Torr. The neutral cluster grew not only by monomer attachment but also by cluster-cluster aggregations. The average size of Ar clusters at P_0=4000Torr was 2000atoms/cluster.

4. Since the cross-sections of clusters were much higher than those of monomers, the mean free path becomes small. A large cluster compensated the energy of collisions with residual gas by the cohesive energy.

5. Though the monomer ion current increased linearly with the electron emission current, the cluster ion current was saturated. This was attributed to the lack of neutral clusters in the beam.

6. The ionization efficiency of the cluster with size n was almost proportional to $n^{\frac{2}{3}}$. The ionization efficiency of a cluster with size of 1800 was about 50% when the electron emission current was 260mA.

7. Intense reactive cluster beams such as O_2 and SF_6 were obtained by mixing of He. Since a SF_6 molecule has many vibration modes, it needed a large fraction of admixed He to obtain cryogenic SF_6 beams compared with O_2 clusters. The average cluster size of O_2

cluster beams was about 2000, which was almost the same as Ar cluster beams.

8. When Ar/O_2 mixed gas was used as a source gas, not only monatomic clusters of Ar_n and $(O_2)_n$ but also complex clusters of $Ar_m(O_2)_n$ were generated. The composition and intensity of complex clusters could be changed by the flow fraction of O_2. The intensity of $Ar_m(O_2)_n$ could be estimated from that of Ar_m and $(O_2)_n$.

9. Multiply charged O_2 clusters were observed when the ionization energy exceeds 40eV. The fraction of doubly charged cluster ions increased with the ionization energy. The generation of doubly charged cluster ions was verified by the existence of $(O_2)_n \cdot O^{2+}$ ions.

10. Coulomb repulsion between the charges was compensated by the cohesive force of a cluster. Therefore, a multiply charged large cluster was more stable than small clusters. The cross-section of singly and doubly charged clusters was almost the same when the ionization energy was 100eV, which was much higher than for monomer ions.

Chapter 4

Sputtering Phenomena with Ar Cluster Ions

4.1 Sputtering yield with Ar Cluster Ions

4.1.1 Sputtering Yield

Introduction

When an energetic ion penetrates into a target, the target atoms yield to the kinetic energy carried by the projectile ion, and subsequently they are knocked on from their lattice sites. If these primary knocked on atoms have enough kinetic energy, they also knock on other atoms in the same way as the projectile ion. This leads to chain reactions of collisions, and is termed a 'collision cascade'. When this collision cascade reaches the target surface, surface atoms are ejected into vacuum if the kinetic energy of these atoms is higher than the surface binding energy.

Sputtering had originally been regarded just as an undesired effect, which destroys cathodes and grids in gas discharge tubes or ion sources and contaminates the plasma and the surrounding walls. However, sputtering is used today for many applications and has become an indispensable process in modern technology. For example, it is applied in sputter ion sources, in obtaining atomically clean surfaces, in micro-machining, in surface planarization, and in depth profiling of thin films. For thin film deposition, high quality thin films are produced by physical vapor deposition, such as the magnetron sputtering technique. The majority of the sputtered particles are neutral, however, a few percent of them are

ionized. The Secondary Ion Mass Spectrometry (SIMS) technique makes use of this secondary ion emission.

To treat the sputtering phenomenon in the solid, Sigmund proposed the linear cascade theory[75]. In the theory, it is assumed that any moving atom collides only with stationary atoms, which is the reason that it is called 'linear'. The average values of various parameters (sputtering yield, angular and energy distributions) can be obtained by solving the Boltzmann equation. The sputtering yield Y at normal incidence is described as follows[75].

$$Y(E) = 0.042 \frac{\alpha(M_2/M_1)s_n(E)}{U_s} \tag{4.1}$$

where α is a function depending on the mass ratio of the impinging ion (M_1) and the target atom (M_2). The $s_n(E)$ and U_s are the nuclear stopping cross-section and the surface binding energy, respectively. From Eq. 4.1, the sputtering yield is proportional to the nuclear stopping cross-section $s_n(E)$. This theoretical analysis and experimental results show good agreement over a broad energy range.

However, the linear cascade theory is based on the linearity of the collision cascade. Thus, it breaks down under dense cascade conditions (spike cascade). It is reported that strong yield enhancement is observed for heavy mass projectiles, molecules or clusters[76, 77]. These effects are explained as non-linear effects caused by high density of energy deposition in a local area.

When the primary projectile is a cluster ion, the nuclear stopping power is much higher than that of a monomer ion and the total energy of a cluster is deposited in the surface region. Fig.4.1 shows molecular dynamics simulations of an Ar monomer ion and an Ar cluster ion with cluster size of 688 impacting Si surfaces. The total acceleration energy was 7keV. In the case of the Ar monomer ion impact, this causes cascade collisions in the Si substrate and the dislocated atoms are generated deep inside the target. In contrast, the Ar cluster ion with the same total acceleration energy generates a spherical damaged area near the surface. The total energy of 7keV is deposited in this small area which causes crater and shockwave generation. Therefore, the sputtering mechanism with cluster ions is completely different from that with the monomer ions. In this section, the sputtering effects with Ar cluster ions are discussed in terms of the sputtering yield, the energy and incident angle dependencies.

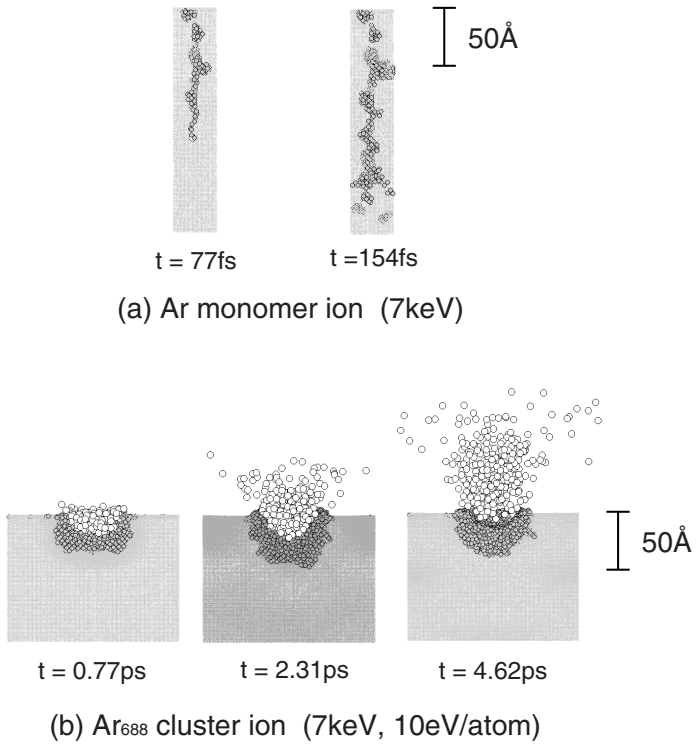

Figure 4.1: Molecular dynamics simulations of an Ar monomer ion and an Ar cluster ion with cluster size of 688 impacting Si substrate.

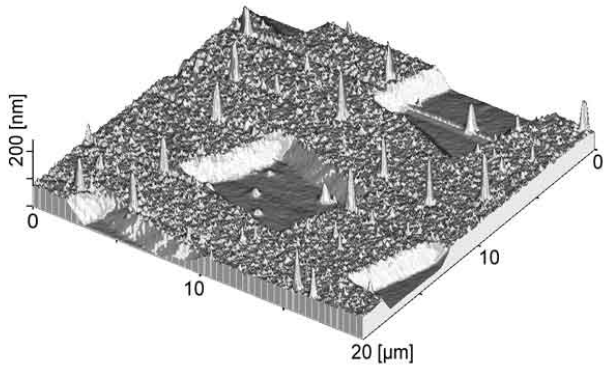

Figure 4.2: AFM images of Au surface irradiated with 20keV Ar cluster ion beams through an ultra fine mesh. The ion dose was 1×10^{16}ions/cm^2.

Experimental Procedure

Sputtering yields of various materials were obtained from the sputtered depth measured by a contact surface profilometer or an Atomic Force Microscope (AFM). Since the contact surface profilometer requires a sputtered depth of more than 100Å, it was used for targets with high sputtering yield. A stainless mesh with 1mm spacing was mounted on the target as a mask, and after irradiation the difference of the height was measured.

For a material that is hard and difficult to sputter to a depth of over 100Å, an AFM observation was carried out. In the AFM observation, the target was covered with an ultra fine Ni mesh (Buckbee-Mears St.Paul, MN-47) before irradiation. This micromesh has 2000 wires per inch, in other words, 12μm spacing between the lines. As the maximum scanning area of the AFM was 20μm$\times$20μm, at least one of the edges can be observed in the scanning area.

Fig. 4.2 shows the AFM image of an Au target irradiated with an Ar cluster ion beam through the ultra fine mesh. The acceleration energy, cluster size and the ion dose were 20keV, 2000atoms/cluster and 1×10^{16}ions/cm^2, respectively. Several square areas with lower height were observed which were the areas irradiated with Ar cluster ions. The sputtered depth can be measured from the cross-section of the AFM image. Sputtering yields were obtained from the sputtered depth, the ion dose and the density of the target.

Sputtering Yields of Various Elements

To measure the sputtering yield with Ar cluster ions, the linearity between the ion dose and the sputtered depth must be confirmed. If this linearity is not satisfied, the sputtering yields will change according to the ion dose. Fig. 4.3 shows the ion dose dependence of the sputtered depth with 20keV Ar cluster ion beams for various elements[78]. The average cluster size was 2000atoms/cluster. The target materials were Ag, Si, Cu, Au, W, Zr and Ti. The Cu and W films were deposited on Si by magnetron sputtering and chemical vapor deposition, respectively. The other films were deposited by vacuum evaporation onto Si substrates. The ion dose was changed over a range from 8×10^{14} to 8×10^{15}ions/cm^2.

From Fig. 4.3, the sputtered depth increased linearly with the ion dose, and no dose effect was observed. If the surface was contaminated or was covered by a film of other materials with low sputtering yield, the sputtering yield recorded would not lie on the observed curve and would saturate at a certain value. But, this was not the case in this experiment. The slopes of these lines were defined as the sputtering yields of each material.

Fig. 4.4 shows the sputtering yields of various materials with 20keV Ar cluster ions arranged according to the atomic numbers. The sputtering yields with cluster ions were obtained from the slopes of the lines in Fig. 4.3. To confirm the reliability of this experimental procedure, the sputtering yield with 20keV Ar monomer ions was compared with the reference values[79].

The sputtering yields with monomer ions showed periodic changes according to the atomic number. This tendency originated from the fact that the sputtering yield was inversely proportional to the binding energy of the atoms. Therefore, the sputtering yields of the atoms in the Ib group (Cu, Ag and Au) were higher than those in the IIIa group (Ti, Zr) or VIa group (W). This is explained in that the binding energy becomes low when the *d* shell is filled by electrons, which results in the increase of the sputtering yield[80, 81]. The sputtering yields measured in these experiments showed good agreement with the reported values, and this confirmed the reliability of the experiment.

Compared with the sputtering yields measured with Ar monomer ions at the same acceleration energy, those obtained with Ar cluster ions were one order of magnitude higher. For example, the sputtering yield of Cu with Ar cluster ions (65.5 atoms/ion) was twelve times higher than that

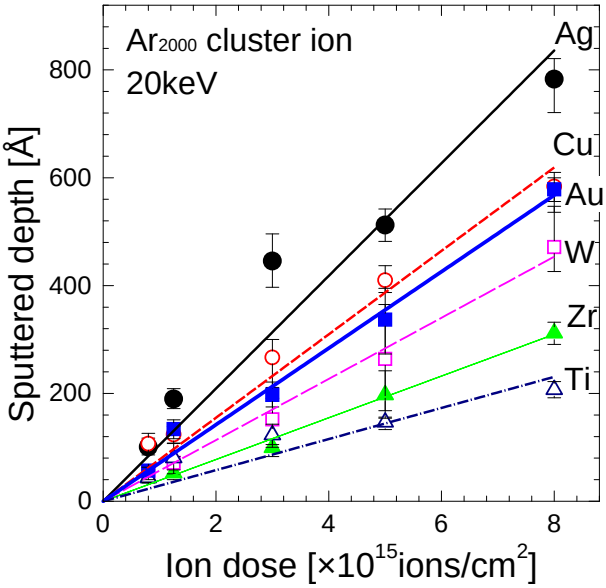

Figure 4.3: Ion dose dependence of sputtered depth with 20keV Ar cluster ions for various materials.

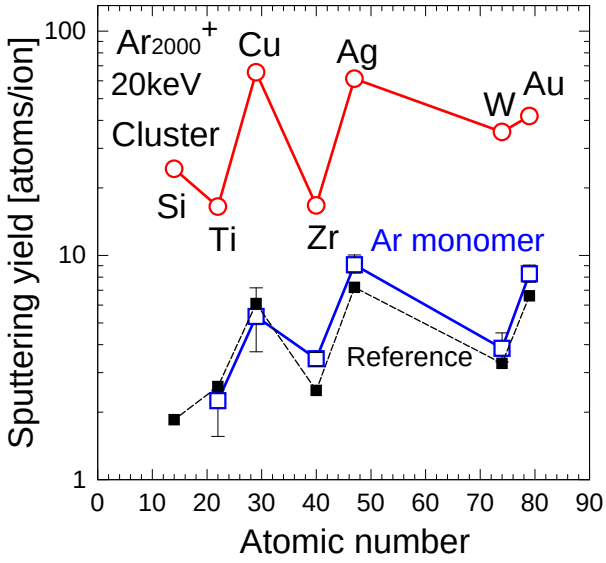

Figure 4.4: Sputtering yields of various materials with 20keV Ar monomer ions and Ar cluster ions.

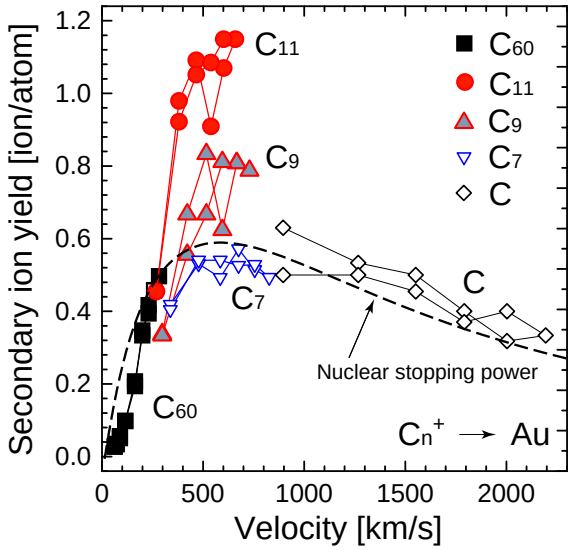

Figure 4.5: Velocity dependence of secondary ion yield with C_n cluster ions from an Au surface. ($n = 1 \sim 60$)

with Ar monomer ions (5.3 atoms/ion). Moreover, the sputtering yield with Ar cluster ions followed the same periodic changes as that observed with monomer ions. The sputtering yields of other materials with Ar cluster ions can be roughly estimated from the reference values with Ar monomer ions.

The enhancement of the sputtering yields have been observed with dimers and trimers with energies of 4∼500keV [77, 82, 83]. To confirm a yield enhancement at the same velocity, a carbon cluster which has an accurate cluster size was irradiated on Au, and the secondary ion yields were measured. Fig. 4.5 shows the velocity dependence of secondary ion yield with C_n cluster ions ($n = 1, 7, 9, 11, 60$) from an Au surface. The secondary ion yield was normalized to the cluster size, i.e., the number of secondary ions produced by one atom with the same velocity. From Fig. 4.5, the secondary ion yield of small clusters (C_7) was almost same as that of the carbon monomer ions, which followed the nuclear stopping power curve of a carbon ion in Au calculated with TRIM[84]. At this cluster size, there was no difference in the ion emission process between monomer and small cluster ions.

However, an enhanced secondary ion yield was observed starting from cluster size of 9. At the ion velocity of 600km/s, the secondary ion yield

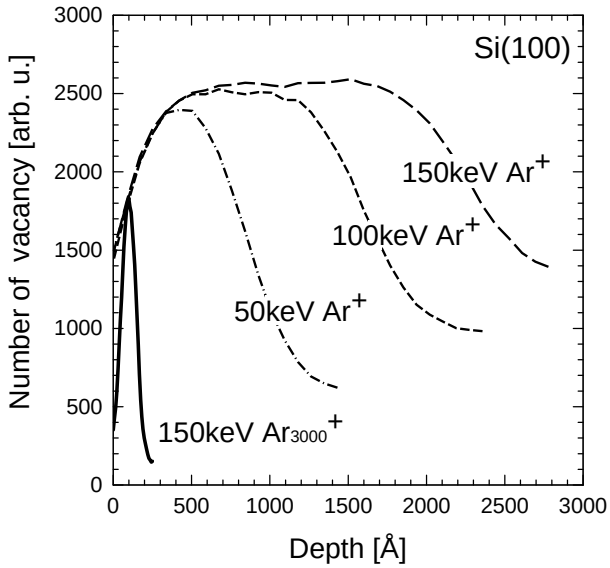

Figure 4.6: Damage distribution in Si(100) with Ar monomer and Ar cluster ion irradiation. The acceleration energy ranged 50 to 150keV.

with C_{11} was twice as high as those with C and C_7. From the molecular dynamic simulation, the nuclear stopping power of C_{60} in graphite with an energy of 1keV/atom was 40eV/Å, which was twice that of a monomer ion. The total energy of a cluster ion was deposited on the surface region and the penetration depth became shallow. It attained a dense energy region on the surface, and as a result, both the secondary ion yield and the sputtering yield became high with large cluster ions.

As well as the enhancement of secondary ion emission, the depth profiles of the dislocated atoms in Si were measured by the channeling method of Rutherford Backscattering Spectrometry (RBS). Fig. 4.6 shows RBS channeling spectra of Si(100) substrates irradiated with 150keV Ar cluster ions and 50∼150keV Ar monomer ions. The ion dose of clusters and monomers were 2.5×10^{13} and 1×10^{15}ions/cm^2, respectively. The thickness of the damaged layer with Ar cluster ions ranged from 20 to 30nm, which was about one tenth of that with Ar monomer ions at the same acceleration energy.

However, the energy of monomer ion which gives the same damaged depth as that with 150keV Ar cluster ions was estimated as 10keV from the TRIM calculation. As the energy per atom of the cluster was

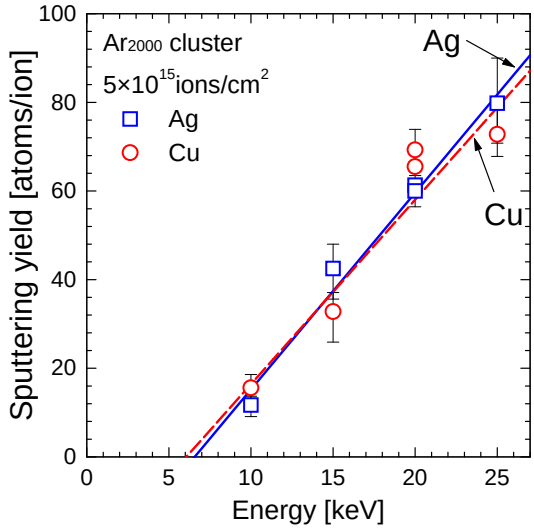

Figure 4.7: Energy dependence of the sputtering yield with Ar cluster ions

50eV/atom, the cluster impact caused greater damage than monomers with the same energy per atom. The nuclear stopping power of a large cluster ion is extremely high and the total impinging energy is deposited at the surface region. This causes shockwave generation and consequent damage formation[85].

4.1.2 Energy Dependence

Energy Dependence of the Sputtering Yield

Fig. 4.7 shows the acceleration energy dependence of the sputtering yield of Cu and Ag with Ar cluster ions. The ion dose was 5×10^{15}ions/cm^2 and the average cluster size was 2000 atoms/cluster. Acceleration energy ranged from 10 to 25keV.

The sputtering yields increased almost linearly with the acceleration energy in this range, and there was a threshold energy for sputtering at 6keV. In the case of monomer ions, the sputtering yield increased linearly in the range from about 50eV to 1keV, and then gradually saturated due to the energy deposition in the deeper region[86]. The threshold energies of sputtering for Cu and Ag are 17 and 15eV, respectively[87]. As the cluster size was 2000atoms/cluster, each atom in the cluster had a kinetic energy of 3eV at a total acceleration energy of 6keV. This measured threshold

energy was one fifth of the reported value.

Sputtering with single ions is caused by the knock-on cascade which is generated inside of the target and develops towards the surface. This process generates large numbers of defects in the target as the energy of the impinging ion is absorbed there. In the case of cluster ions, the collisions near the surface are dominant and all of the energy is efficiently deposited onto the surface atoms as shown in Fig. 4.6. Thus, the surface atoms are sputtered at a low energy, indeed, below the threshold value with cluster ions.

Microscopic View

When a cluster impacts upon a solid surface, a crater structure is formed similar to a meteor impact on the earth[10]. The target morphology, the diameter and the depth of craters formed by a cluster impact are determined by the kinetics of energy transfer from the projectile to the target. The single tracks of a cluster impact have been studied with Transmission Electron Microscope (TEM)[88], however it is troublesome and difficult to prepare the samples. In this study, a single crater was observed with a Scanning Tunneling Microscope (STM). As the depth resolution of the STM is affected by a localization of electrons, the crater diameter was used to obtain the energy dependence.

Fig. 4.8 shows the energy dependence of the inside and outside of the crater diameters as measured with STM. The target was an Au(111) surface and the acceleration energy V_a of the Ar cluster ranged from 20 to 150keV. The cluster size was 3000 atoms/cluster as separated with a Wien filter. The irradiation with the Ar cluster was performed at a very low ion dose (1×10^{10}ions/cm^2) to prevent overlapping of the craters. From Fig. 4.8, both the inside and outside diameters of the crater were proportional to the cubic root of the acceleration voltage ($V_a^{\frac{1}{3}}$). The same tendencies of crater diameter were also observed in Highly Oriented Pyrolytic Graphite (HOPG) and sapphire(0001) surfaces[14].

Fig. 4.9 shows a molecular dynamics simulation of a C_{60} cluster ion impact on HOPG at various acceleration energies. The damaged area was colored in black. The damaged area with a cluster ion impact was almost hemispherical when the energy per atom was less than 500eV/atom. If the energy was larger than 500eV/atom, the damaged area became deeper. Under the irradiation conditions of the large Ar clusters in Fig. 4.8, the energy per atom varied between 6 and 50 eV/atom. This

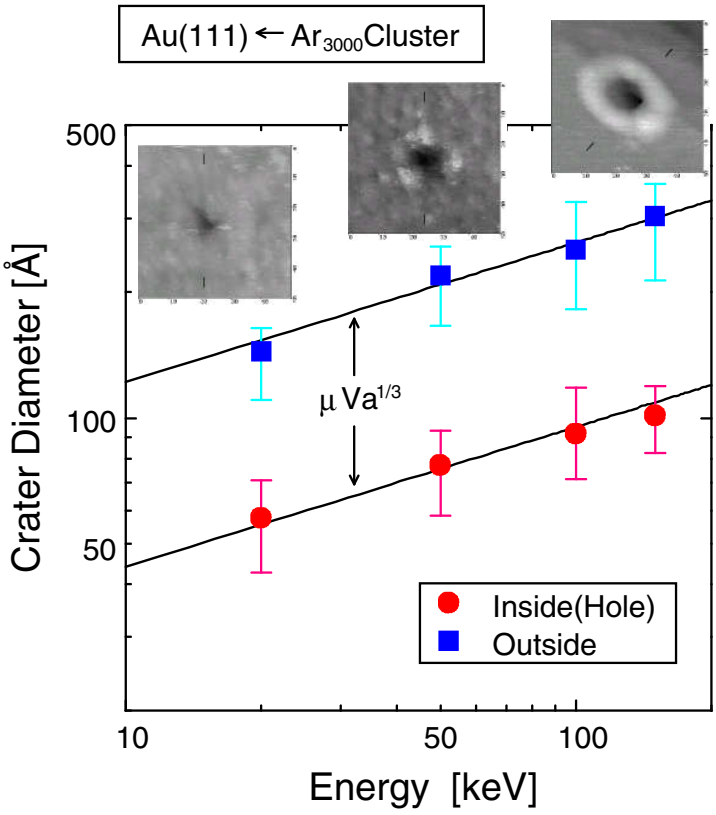

Figure 4.8: Energy dependence of the crater diameters with Ar cluster ions on Au surfaces.

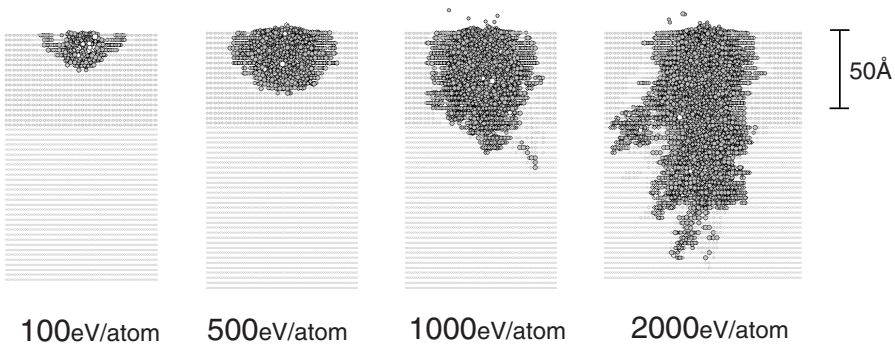

Figure 4.9: Molecular dynamics simulation of C_{60} impacts on HOPG surface at various acceleration energies.

result means that the total energy was deposited into the target isotropically at this energy. Since the crater diameter increased in proportion to $V_a^{\frac{1}{3}}$, the volume of the damaged area showed a linear dependence on V_a.

The damaged area induced by cluster ion impact became longitudinal in shape along the penetration direction when the acceleration energy exceeded 1keV/atom. In this energy region, the nuclear stopping power of the cluster decreased. The reduction of nuclear stopping power of a cluster is attributed to the 'clearing-the-way effect'[89, 90], which is explained as follows: only the bottom part of the cluster collides with target atoms whereas majority of the atoms in the upper part of the cluster penetrate deeper without collisions. It is expected that the sputtering yield of clusters with high energy will no longer be proportional to the acceleration energy.

4.1.3 Incident Angle Dependence

The first qualitative information on the angular dependence of the sputtering yield was obtained by Fetz and Wehner[91]. For single ion bombardment in the keV energy region, it was found that the angular dependence of the sputtering yield $\psi(\theta)$ was given by $\psi(\theta)/\psi(0°) = 1/\cos\theta$, where θ is the angle from the surface normal.

Sigmund, however, showed that $1/\cos\theta$ dependence should be expected only for large M_2/M_1, and that it increased in proportion to

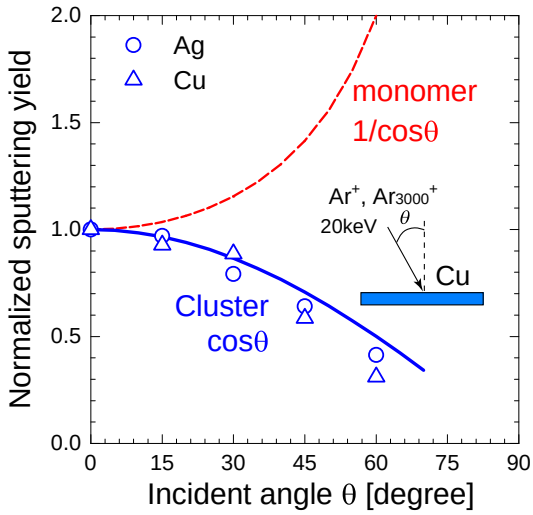

Figure 4.10: Incident angle dependence of the sputtering yields of Cu and Ag with 20keV Ar cluster ions.

$\cos^{-f}\theta$ ($f = 1 \sim 2$)[75]. In both cases, the sputtering yield reaches a maximum at angle of $60° \sim 80°$. When the incident angle changes inclination from normal to oblique, the collision frequency in the near surface region becomes high and all the energy is deposited in this area, resulting in high sputtering yield. With a further increase of the incident angle, the sputtering yield suddenly decreases. As reflection from the surface is dominant in this region, the incident ions cannot deposit their kinetic energy onto the target atoms.

The incident angle dependence of the sputtering yield with monomer ions can be described by the linear cascade collision theory[75], however, the energy loss and deposition process of cluster ions are completely different from those of monomer ions. Fig. 4.10 shows the incident angle dependence of the sputtering yield with 20keV Ar cluster ions. The target materials were Cu and Ag films. The ion dose and the average cluster size were 5×10^{15}ions/cm^2 and 2000 atoms/cluster, respectively. The sputtering yields $\psi(\theta)$ were normalized to that of normal incidence $\psi(0°)$. The angular dependence with monomer ions was plotted as a function of $1/\cos\theta$.

The normalized sputtering yield with 20keV Ar cluster ions decreased in proportion to $\cos\theta$ in both Cu and Ag targets, which was completely different from the dependence with monomer ions. When the incident

angle was 0°, the penetration depth was the greatest, and most of the kinetic energy was deposited onto the target atoms. In the case of oblique incidence, the impinging energy of the cluster ion was partially deposited onto the target and many atoms in the cluster were ejected or reflected from the surface with large kinetic energy. Since the kinetic energy deposited perpendicularly onto the target was proportional to $\cos\theta$, the sputtering yield followed this curve.

4.2 Angular Distributions of Sputtered Atoms

4.2.1 Introduction

Physical sputtering with monomer ions has been studied from both a theoretical and an experimental point of view. In particular, the angular distributions of the sputtered particles have attracted the interest of both theoreticians and experimentalists working on the sputter deposition of films. In the region where isotropic cascade collision is the dominant process, the linear cascade collision theory gives a good quantitative description of the sputtering process[75]. It led to the isotropic distribution of the sputtered atoms, termed the 'cosine distribution'.

However, in both the low energy and high energy regions, the linear collision cascade theory cannot describe the sputtering phenomenon. In the case of very low projectile energy, it is difficult to convert the momentum and the distribution is flattened, which is called 'under-cosine' distribution. At higher projectile energy, the distribution becomes more outward peaked than the cosine one, which is called 'over-cosine'. These angular distributions at normal incidence are well fitted by a function of $\cos^n\theta$[92].

When the projectile ion impacts the target at an oblique angle, the angular distributions are described in terms of two physical mechanisms: cascade collision and direct ejection. With increasing incident angle, the influence from direct ejection become more dominant and, finally, no cascade collisions are observed at a glancing angle.

In the case of cluster ion incidence, there are few experimental measurements of the angular distribution of sputtered atoms. Computer simulations with molecular, poly-atomic and cluster ion impact have been performed[24]. When a large cluster impacts a solid surface, the impinging energy of the cluster is deposited into a local area, resulting in the formation of a crater with depression and hill. Since this large crater for-

mation is not observed under monomer ion impact, a different sputtering mechanism and angular distribution are expected. In this section, the angular distribution of sputtered atoms with Ar cluster ions at several incident angles is discussed.

4.2.2 Experimental Procedure

The experimental setup of the angular distribution measurement is shown in Fig. 4.11(a)[93]. The target material was irradiated with Ar cluster ion beams through an aperture 2mm in diameter. The incident angles were changed from 0° to 60°, and the ion dose was fixed at 1×10^{17}ions/cm^2. Sputtered particles were collected on Si substrates mounted on a semi-cylindrical holder. The size of the Si collector was 5mm×20mm, and the distance between the target and the Si collector was 50mm. Each Si substrate was located at the same interval of 15°, and the temperatures of the substrate and target were ambient.

After irradiation, the densities of the target materials on the Si collectors were measured by Rutherford Backscattering Spectroscopy (RBS). The dependence of the sticking probability on the collector was negligible because there was no difference in the distribution with carbon collectors. Fig.4.11(b) shows example RBS spectra at a Cu peak on a Si substrate at several incident angles of the cluster ions. The relative yield at the collector was obtained by the integration of the area under the peak. The peak counts with an ion dose of 1×10^{17}ions/cm^2 were sufficient for these measurements.

In the case of Ar cluster ions, polycrystalline Cu films were used because the surface binding energy of Cu is relatively low and it shows a high sputtering yield. In addition, there are many previous reports on the sputtering of Cu with Ar monomer ions and they allow a good comparison with the sputtering mechanisms of cluster ions.

As well as the macroscopic distributions, a microscopic observation of single tracks with cluster ion impact was carried out using a Scanning Tunneling Microscope. These track images have been compared with the macroscopic angular distributions.

4.2.3 Angular Distribution with Ar Clusters

Fig. 4.12 shows the angular distributions of Cu atoms sputtered by 20keV Ar monomer ions and 10keV and 20keV Ar cluster ions at normal inci-

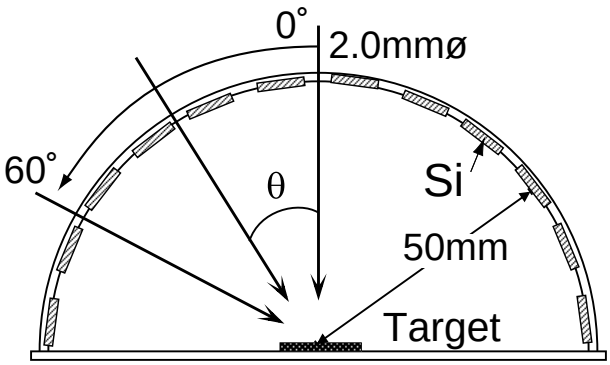

(a) Sample holder for the angular distribution measurement

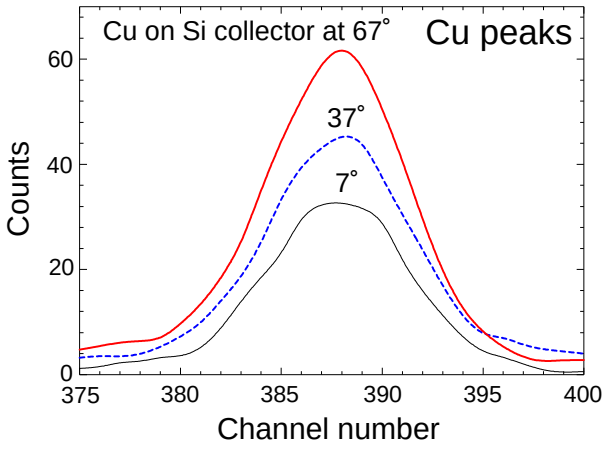

(b) RBS spectra around Cu peaks on Si collectors

Figure 4.11: Sample holder for the measurement of angular distribution of sputtered particles and the RBS spectra around Cu peak on Si collectors.

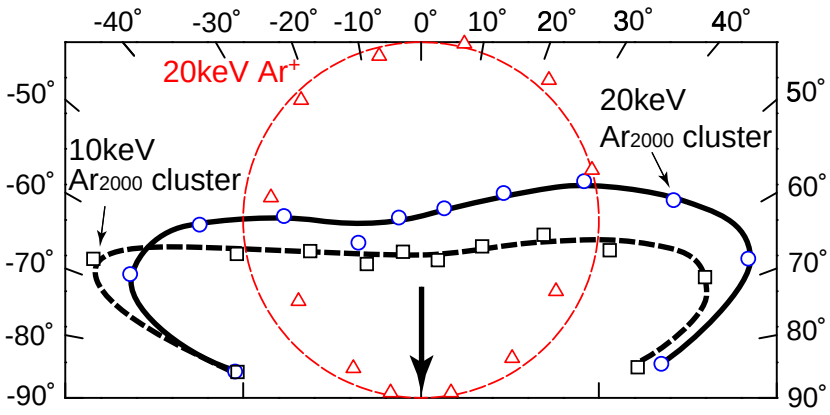

Figure 4.12: Angular distribution of sputtered Cu atoms with 20keV Ar monomer, 10keV and 20keV Ar_{2000} cluster ions at normal incidence.

dence. The average cluster size and the ion dose were 2000 atoms/cluster and 1×10^{17}ions/cm^2, respectively. It was reported that the surface morphology affected the angular distribution[94]. The Cu surface used in this study was polycrystalline with a grain width of 400nm and 15nm height. However, the Cu surface was smoothed by Ar cluster ions with an ion dose of 3×10^{15}ions/cm^2, which was a few percent of the total ion dose. Therefore, the initial surface roughness was expected to have little influence on the angular distributions.

In the case of 20keV Ar monomer ion, the angular distribution formed a circle in the center of Fig. 4.12. This circular distribution almost followed the cosine law, which indicated an isotropic ejection of atoms from the surface. This result showed good agreement with the linear cascade collision theory, and also verified the accuracy of the present experiments.

In contrast, the angular distribution with Ar cluster ions showed it to be under-cosine. With the reduction of incident energy to 10keV, the angular distribution became more flattened. Although the shape was similar to that produced by low energy monomer ions, the energy density was much greater with a cluster ion impact. It has been reported that the dense cascade (spike) collision with very heavy ions or molecular ions impact causes sputtering yield enhancement, crater formation and other non-linear effects[76]. From MD simulations, it was estimated that the transient temperature of the surface rose to 10^5 K and the pressure increased to 1Mbar on cluster impact[95]. Thus, one can expect differences

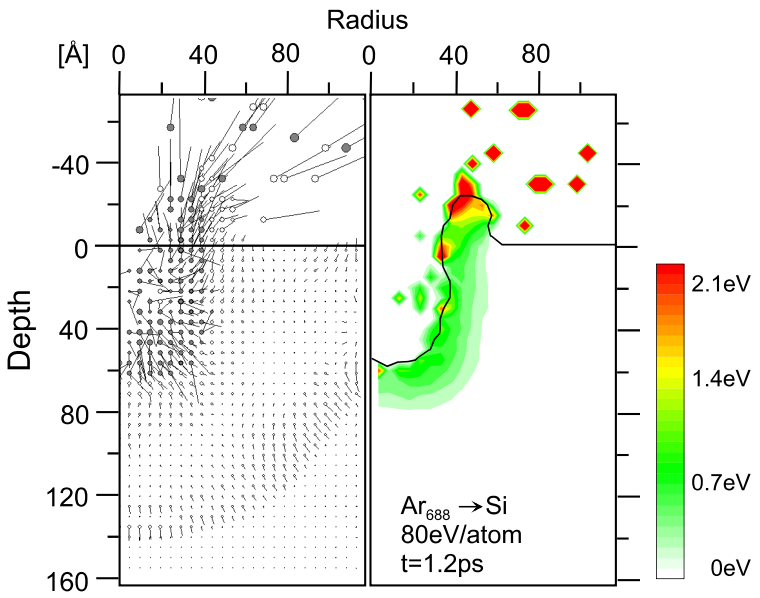

Figure 4.13: Cross-sectional view of the crater when an Ar_{688} cluster with energy of 80eV/atom impacts a Si target as simulated by molecular dynamics method. The radius of the circles and the length of the lines represent the mean kinetic energy and the mean magnitude and direction of the momentum, respectively.

between the sputtering mechanisms of monomer and cluster ions.

Fig. 4.13 shows the energy and momentum profiles in a collision of an Ar cluster with a Si target as simulated by the molecular dynamics method[96]. This snapshot was at a time of 1.2ps after the impact. The cluster size and the energy per atom were 688 and 80eV/atom, respectively. The radius of the circles and the length of the lines represent the mean kinetic energy and the mean magnitude and direction of the momentum, respectively.

When a cluster collides with the target, the kinetic energy of the cluster was transferred to the target isotropically and, as a result, a symmetric crater was formed. The impacted area came under both high temperature and high pressure conditions, and the shockwave propagated isotropically. Shockwave generation was also observed in the macroscopic body impact with supersonic velocity[97]. There were common characteristics between them.

In Fig. 4.13, numerous particles were sputtered and the direction of

these particles was lateral to the trajectory of the impinging cluster. Also, there were many atoms with large lateral momentum in the rim of the crater. The kinetic energy of these atoms was higher than 2eV. Since this was close to the energy of the Si-Si bond (3.4eV)[98], these atoms would be ejected to vacuum at a future time point in the simulation. These ejected particles caused the under-cosine distributions. It was reported that large number of dimers and trimers were contained in the sputtered particles with the cluster ion impact[99]. These phenomena can be explained by a mechanism whereby bunches of atoms leave from the edge of the crater. From these results, it is clear that the sputtering mechanism with cluster ions is completely different from that of low energy monomer ions. This ejection of the sputtered atoms horizontal to the target plane is termed 'lateral sputtering'.

4.2.4 Incident Angle Dependence of Angular Distribution

As described in section 4.1.3, the sputtering phenomena, such as the penetration depth, density of deposited energy, damaged area, sputtering yield and numerous other parameters, depend upon the incident angle. Therefore, the angular distribution of sputtered particles is also influenced by the incident angle.

Fig. 4.14 shows the angular distribution of Cu atoms sputtered by Ar cluster ions incident at oblique angles. The incident angle ranged from 10° to 60° and the acceleration energy was fixed at 20keV. The average cluster size was 2000 atoms/cluster.

Even at an oblique incident angle of 10°, the majority of the sputtered particles was distributed to the forward direction. No significant change in the angular distribution was found on increasing the incident angle from 10° to 60°. At normal incidence, as shown in Fig. 4.12, the angular distribution was not perfectly symmetrical, which might be due to a slight tilt of the target caused by an experimental error. These results clearly indicate that the angular distribution with cluster ions is sensitive to the incident angle near to the normal. When a cluster impacts the target at normal incidence, the acceleration energy is deposited isotropically. However, localization of energy density occurs under an oblique impact, and this energy is preferentially released from one side.

In the case of monomer ions, energetic ions penetrate deep into the target and induce random collision cascades. Therefore, there are no sig-

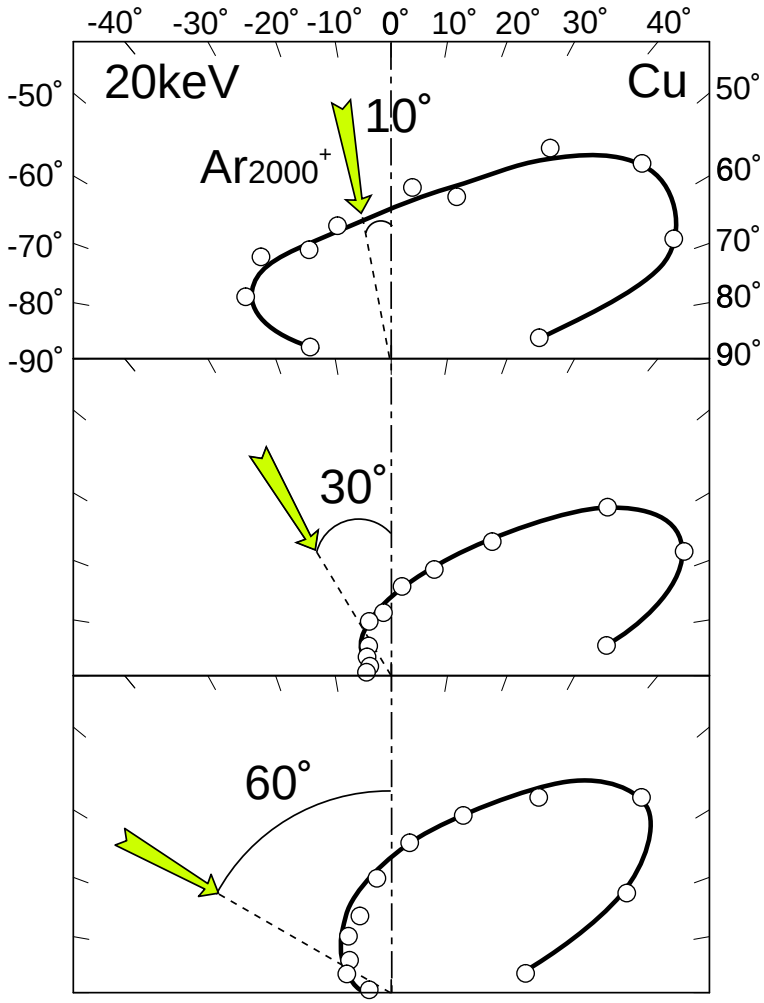

Figure 4.14: Angular distribution of atoms sputtered by Ar cluster ions at several incident angles. The average cluster size and acceleration energy are 2000atoms/cluster and 20keV, respectively.

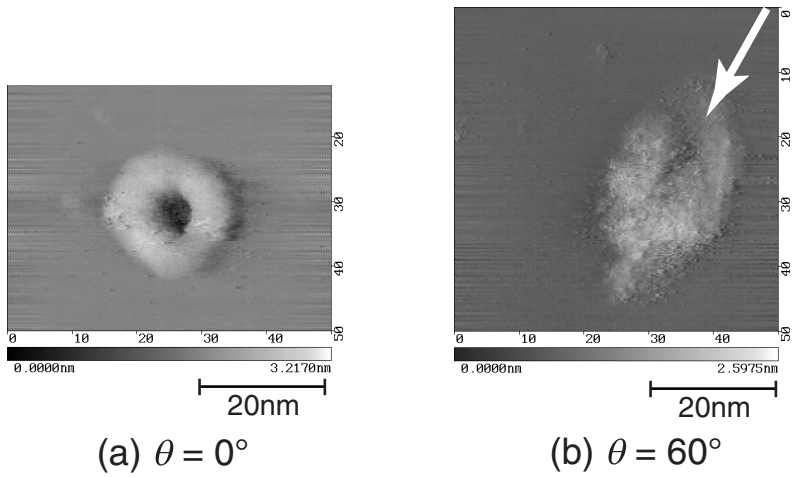

Figure 4.15: STM images of Ar_{100} cluster ion impact on HOPG surface at oblieque incidence. The acceleration energy was 150keV.

nificant changes with change of incident angle near 0°. With increasing the incident angle up to 80°, the preferential ejection angle, which corresponds to direct ejection, is observed with monomer ions. Thus, the drastic change of the angular distribution at near normal incidence is a distinctive feature of cluster ion bombardment.

In addition to the macroscopic measurement of sputtered particle distributions, microscopic observations of single traces caused by cluster ion impacts were performed with STM. Fig. 4.15 shows STM images of a Highly Oriented Pyrolitic Graphite (HOPG) surface irradiated with 150keV Ar cluster ions at incident angles of 0° and 60°. The Ar cluster size was 100atoms/cluster as selected with a Wien filter. The scanning area of the STM was 50nm×50nm. In the case of normal incidence (Fig. 4.15(a)), a doughnut shape crater was formed and the ejected atoms from the crater formed a mound around the hole of the crater. A highly symmetric crater was clearly observed at normal incidence.

However, at an incident angle of 60° (Fig. 4.15(b)), the shape of crater was asymmetric and the ejected atoms formed a large mound in the direction forward from the penetration direction. These microscopic images of a single cluster ion impact showed good agreement with the angular distribution of the sputtered atoms as shown in Fig. 4.14. An asymmetric track was also observed in a high energy ($\sim$ MeV) C_{60} cluster

ion impact at oblique angles[100].

From the cross-section of the crater, the volume of the crater hole was much higher than the volume of the sputtered atoms, or, in other words, the sputtering yield of the cluster ion. Therefore, most of the atoms ejected by a cluster ion impact were moved to around the rim of the crater, and the fraction of sputtered atoms was estimated to be only about a few percent of the ejected atoms.

4.3 Summary

Sputtering phenomena associated with Ar cluster ion beams were discussed in this chapter. The dense energy deposition in a local area caused multiple collisions which resulted in shockwave and crater formation. Therefore, the sputtering effects were completely different from those of monomer ions. The results were summarized as follows:

1. Sputtering yields of various elements with Ar cluster ions were one or two orders of magnitude higher than those with Ar monomer ions. However the sputtering yield with cluster ions depended on the surface binding energy of the elements so that it showed the same trend on the elements as that of monomer ions.

2. The secondary ion yield from a gold surface was enhanced with C_n clusters ($n > 9$). The nuclear stopping power of a cluster was much higher than for monomer ions in the energy between 10∼1000eV/atom. The damage depth with 150keV Ar cluster ions ranged from 20 to 30nm, which was one tenth of that with 150keV Ar monomer ions.

3. Sputtering yield with Ar cluster ion increased linearly with the acceleration energy. There was a threshold energy for sputtering at the acceleration energy of 6keV. The energy dependence of the crater diameter measured with STM showed the same trends. Also, with increasing the incident angle θ, the sputtering yield with cluster ions decreased in proportion to $\cos\theta$.

4. The angular distribution of sputtered atoms with Ar cluster ions showed an under-cosine distribution which was similar to that with low-energy monomer ions. However, these laterally distributed

atoms originated from the edge of the crater so that the sputtering mechanism with cluster ions was completely different from that with monomer ions. These ejections of the sputtered atoms horizontal to the target plane is termed 'lateral sputtering'.

5. The angular distribution changed from an isotropic one to a directional one even when the incident angle was 10°. A further increase of the incident angle did not influence the distribution. The angular distribution of sputtered atom was very sensitive to the incident angle near 0°.

6. The STM images of the sigle traces caused by Ar cluster ion impacts showed good agreements with the angular distributions of the sputtered atoms at both normal and oblique incidence.

Chapter 5

Etching with Reactive Cluster Ions

5.1 Introduction

Following from the rapid progress of electronic devices such as Ultra Large Scale Integrated circuits (ULSI), more advanced fabrication processes for nano-structures are continuously demanded. In addition to the lithography and the impurity doping processes, the dry etching technique is one of the most indispensable technologies for ULSI fabrication, and development of new dry etching processes have been carried out enthusiastically over the last twenty years. Among them, plasma etching processes have been frequently used. Basically, the etching processes are evaluated in the following points.

1. **Etching rate**
   Because of its relation to productivity, high etching rate is preferred.

2. **Uniformity and repeatability**
   In the plasma etching process, perturbations of etching rate depend on the localization of the plasma, the radical density and temperature of the wafers. Uniformity has become essential with the increase of wafer diameter.

3. **Selectivity**
   Selectivity is expressed by the ratio of etching rate between the mask materials and the desired film or substrate. The selectivity

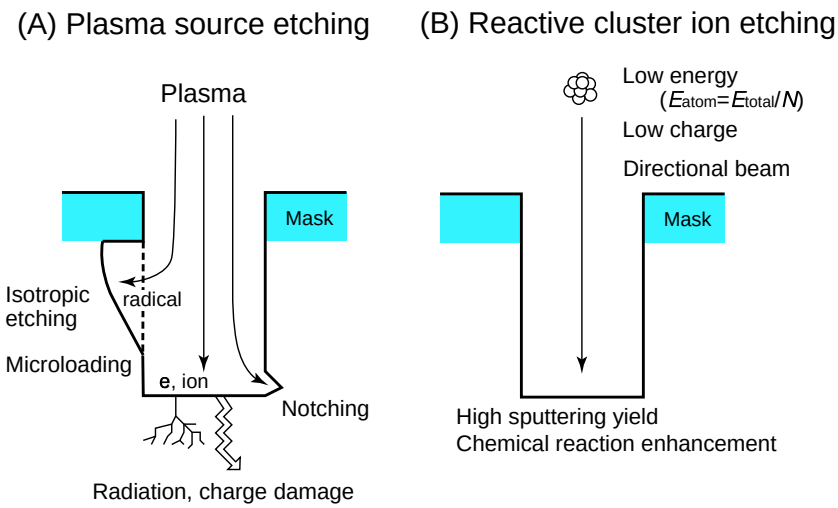

Figure 5.1: Advantages of the reactive cluster ion etching compared with the plasma source etching.

originates from the difference of the chemical reactivities and the volatility of the etching products.

4. **Pattern Profile**
   When a photoresist pattern is etched by wet processing with acid or alkali solution, the substrate is etched isotropically. It causes erosion underneath the mask, and the dimensional difference between mask and target (ΔW) becomes high. Directional beams produce anisotropic etching.

5. **Radiation Damage**
   Both electric and physical damage in the target are expected in a dry etching process. Due to the irradiation with charged particles, a wafer surface becomes charged, resulting in an electric stress in the device. In addition, energetic particles in a plasma cause defects in the crystal or implantation of contaminants into the target.

The chemical reaction becomes the more dominant etching process in the order of (a) Sputter etching, (b) Reactive Ion Etching (RIE), (c) Plasma etching and (d) Downflow etching. Sputter etching uses physical sputtering with inert gas ions, and it is difficult to obtain selectivity. The downflow etching process is performed with excited neutral atoms,

and it does not cause any damage by energetic particles. However, the etching is isotropic. In the RIE process which is frequently used in practical device fabrications, chemical etching is assisted by an energetic ion bombardment[101]. Since the energetic ions in the plasma are directional, anisotropic etching with high selectivity is achieved in the RIE process.

Although the RIE process which uses a plasma source has high productivity and offers the capability for micro-pattern fabrications, there remain many problems as shown on the left hand side of Fig. 5.1; the radiation damage caused by energetic particles in the plasma, the reduction of etching rate in the pattern with high density and high aspect ratio (microloading effect), the notching and the breakdown of the device by charging up.

As discussed previously, the gas cluster ion beam shows distinctive physical sputtering effects caused by the dense energy deposition in a local area. When a reactive gas is used as source gas, enhancement of these sputtering effects by chemical reaction is expected. Also, as to the radiation damage induced by high energy particles, the energy per atom in a cluster is equal to the total energy divided by the cluster size. For example, each SF_6 molecule has only 10eV when SF_6 clusters with a cluster size of 2000 are accelerated to 20keV. As the displacement energy of Si is about 13eV[102], this energy per molecule is less than the displacement energy. Therefore, low damage etching of a Si substrate is expected.

Further, since the number of atoms transported by a reactive cluster is much larger than the number of electrical charges, the reactive cluster ion beam process does not cause the charging up which is usually a serious problem in plasma processes. Moreover, in the cluster beam process, the beam impacting the target is directional. As a result, anisotropic etching is achieved and there is no dependence of the etching rate on etching pattern (microloading) as caused by radicals in the plasma. The advantages of the reactive cluster ion beam method were summarized in Fig. 5.1.

In this chapter, the reactive sputtering effects with SF_6 cluster ions were studied as to the reactive sputtering yield, the energy dependence and the selectivity of the etching rate. Application of the reactive cluster ion etching were demonstrated for the etching of a Si substrate with fine pattern.

5.2 Reactive Sputtering

5.2.1 Reactive Sputtering Yield

Reactive Sputtering Yield for Various Elements

As described in section 4.1.1, the sputtering yields with Ar cluster ions for various materials are one or two orders of magnitude higher than those with Ar monomer ions. This is caused by the dense energy deposition on the target. However, if the incident ion reacts with the target atoms, the sputtering yield is expected to be much higher than with inert cluster ions due to the enhancement of chemical reactions.

Fig. 5.2 shows the sputtering yield of Si, SiC, W and Au with Ar monomer ions, Ar cluster ions and SF_6 cluster ions for an energy of 20keV. The average size of the Ar and SF_6 cluster ions was 2000. Compared with W and Au which have similar atomic mass, the sputtering yield of Au with Ar cluster ions (42 atoms/ion) was higher than that of W (35 atoms/ion). This tendency was the same as that found with Ar monomer ions. On the other hand, the sputtering yield of W with SF_6 cluster ions was 320 atoms/ion, which was three times higher than that of Au (112 atoms/ion). Tungsten atoms reacted with fluorine and the sputtering yield was enhanced by the production of volatile materials such as WF_x. The enhancement of the sputtering yield with SF_6 cluster ions was also observed for compound materials such as SiC.

Similarly, the sputtering yield of Si with Ar cluster ions (24atoms/ion) was enhanced 55 times by chemical reaction with SF_6 cluster ions (1300 atoms/ion). As the average size of the SF_6 clusters was about 2000 molecules/cluster, the SF_6 cluster ions showed quite a high reaction probability with Si.

The question can be posed as to why a SF_6 cluster ion shows such a high reaction probability with Si even though a SF_6 molecule is stable at room temperature. In the etching process, the following events must be occurring sequentially; (a) absorption of the etchant on the surface, (b) formation of a volatile product and (c) evaporation or ejection of the product from the surface. It was reported that chemical reactions between SF_6 molecules and Si were stimulated by energetic Ar monomer ion bombardments[103], which was explained in that SF_6 molecules were dissociated by the energetic ion bombardment and, as a result, the released fluorine atoms react with Si atoms.

We suppose that both the fragmentation of a cluster and the dissoci-

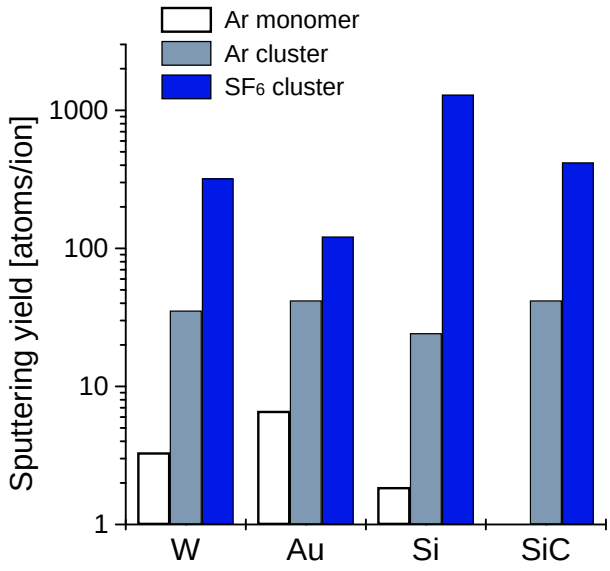

Figure 5.2: Reactive sputtering yield with SF_6 cluster ions for various materials. The acceleration energy was 20keV.

ation of a SF_6 molecule occurred at the same time when a SF_6 cluster ion collided with a Si or W surface. Consequently, SiF_x or WF_x, which are volatile compounds, were produced. SiF_x and WF_x were physically sputtered by energetic ions or were thermally evaporated into the vacuum. Thus, the sputtering yield increased as a consequence of the production of volatile compounds promoted by SF_6 cluster ion bombardment.

To confirm that the etching yield was enhanced by the production of volatile materials such as SiF_x, the mass spectra of evaporated particles during SF_6 cluster ion irradiation was measured using a quadrupole mass spectrometer (QMS). Fig. 5.3 shows the mass spectra when a Si substrate was irradiated with 25keV SF_6 cluster ion beams. The average cluster size was 2000molecules/cluster. An intermediate shutter was installed in front of the Si target and the mass spectra were acquired when it was opened or closed.

From Fig. 5.3, a peak at the atomic mass of 85 showed a marked increase on opening the shutter. This peak was attributed to SiF_3^+. It is well known that SiF_4 molecules lose one fluorine atom by electron ionization. As the ionization of the QMS was performed by electron bombardment, SiF_4 molecules changed to SiF_3^+. Thus, this SiF_3 peak

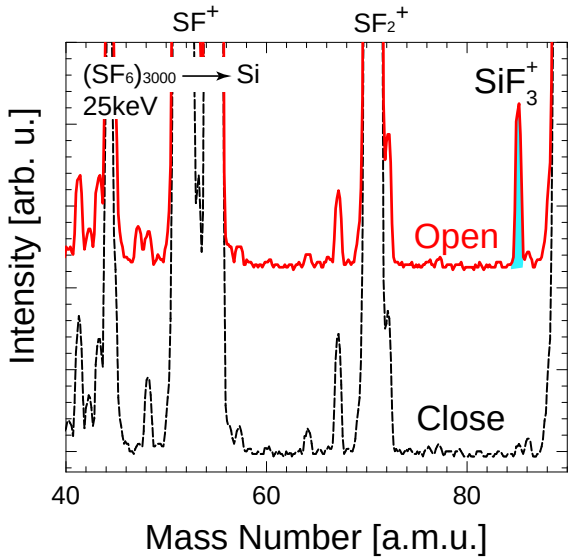

Figure 5.3: Etching product during 25keV SF_6 cluster ion irradiation on Si. The average cluster size was 2000atoms/cluster.

arose from SiF_4 molecules. A marked increase of SiF_4 is evidence for the chemical reaction between Si and fluorine.

As well as SF_6 cluster ions, O_2 cluster ions showed reactive sputtering for diamond and graphite. The high reactivity of O_2 cluster ions was also applied in the oxidation of metals, such as In and Ta to fabricate ITO and Ta_2O_5 films. For the further understanding of the etching process with reactive cluster ions, information concerning the energy distribution of the reaction products is necessary.

Dose Dependence

In case of Ar cluster ions, there is no residual side-product remaining on the surface as a consequence of the chemical reactions. So, the etching rate remains constant. However, in the plasma etching process, the decrease of the etching rate and the delay of the etching process (RIE Lag)[104] are caused by the production of non-volatile materials on the surface. This non-volatile material forms a micro-mask on the surface and prevents the etching of the substrate beneath it. As a result, cone-shaped debris termed 'grass' is formed on the surface[105].

The dose dependence of the etching depth of Si and SiO_2 with SF_6

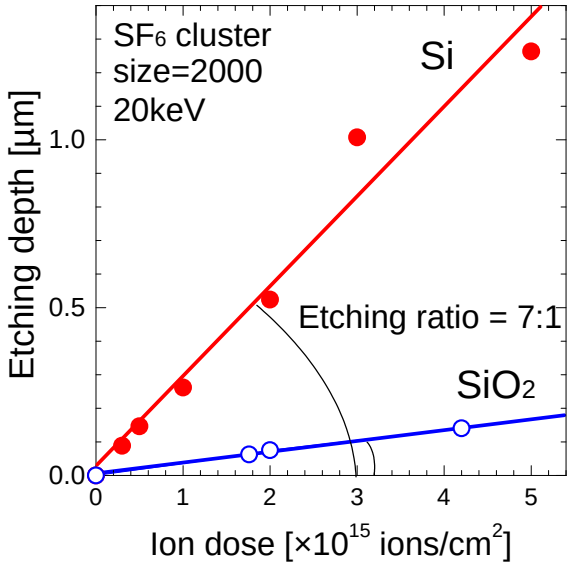

Figure 5.4: Ion dose dependence of etching depth of Si and SiO_2 with 20keV SF_6 cluster ions.

cluster ions is shown in Fig. 5.4. The ion dose ranged from 3×10^{14} to 5×10^{15}ions/cm^2. The acceleration energy and the average cluster size were 20keV and 2000molecules/cluster, respectively. From Fig. 5.4, the sputtered depths of both Si and SiO_2 increased linearly with the ion dose, and no dose effects were observed with SF_6 cluster ion irradiation. The reactive sputtering yields of Si and SiO_2 were measured from these curves as 1300 and 70 atoms/ion, respectively. The etching ratio of Si to SiO_2 at 20keV was obtained from the ratio of the slopes as 7. Regarding the surface morphologies observed by AFM, no debris or grass structures were observed on the Si and SiO_2 surfaces after irradiation, and the surface roughness of the Si surface was 5Å.

5.2.2 Energy Dependence

Etching Depth

Fig. 5.5 shows the energy dependence of the etching depth of Si and SiO_2 with SF_6 cluster ions. The SF_6 cluster size and the ion dose were 2000molecules/ion and 5×10^{15}ions/cm^2, respectively. The target temperature was room temperature. In the case of Ar cluster ions, the sput-

tering yield increased linearly with the acceleration energy as shown in Fig. 4.7. In addition, there was a threshold energy for physical sputtering at 6keV.

In the case of SF_6 cluster ions, the etching depth of Si and SiO_2 increased exponentially with the acceleration energy. When the acceleration energy and the ion dose were 25keV and 5×10^{15}ions/cm^2, respectively, the etching depth of Si was 2.2μm. Even when the acceleration energy was 5keV, which was lower than the threshold energy for physical sputtering, Si was etched to a depth of 300Å by SF_6 cluster ions. In this case, the energy per molecule was 2.5eV, which lay between the activation energy of chemical reactions and the displacement energy of Si crystals. Chemical reactions between Si and fluorine were the dominant etching process at low energy, and as a result, the threshold energy of reactive sputtering became difficult to define.

Etching Ratio

The selectivity arises from the volatility of the reaction products and the difference of the binding energies of the materials. The selectivity with Ar cluster ions is only defined by the surface binding energy of the elements, resulting in the low selectivity.

Fig. 5.6 shows the energy dependence of the etching ratio of Si to SiO_2 with SF_6 cluster ions. With decreasing acceleration energy, the etching ratio increased markedly below 15keV. The etching ratios at acceleration energies of 25keV and 10keV were 7 and 33, respectively. In plasma etching process, the etching ratio of Si to SiO_2 has been reported to be in the range 10∼50. It should be noted that the energy of the cluster ions was in the keV region, and the increase of the selectivity was usually found below 1keV in the case of monomer ions. When the acceleration energy was 5keV, Si was etched in 200∼300Å depth, and the etching depth of SiO_2 was less than the detection level of the surface profiler. This means that the etching ratio was extremely high, and chemical etching was the dominant process at 5keV.

In contrast, the etching ratio with high energy SF_6 cluster ions became low because not only Si but also SiO_2 were physically sputtered with SF_6 cluster ions. Since the irradiation effect of a cluster is defined by energy per atom, the etching ratio of small clusters is thought to be lower than that of large cluster ions.

In Fig. 5.6, the etching ratio of Si to SiO_2 with smaller cluster size

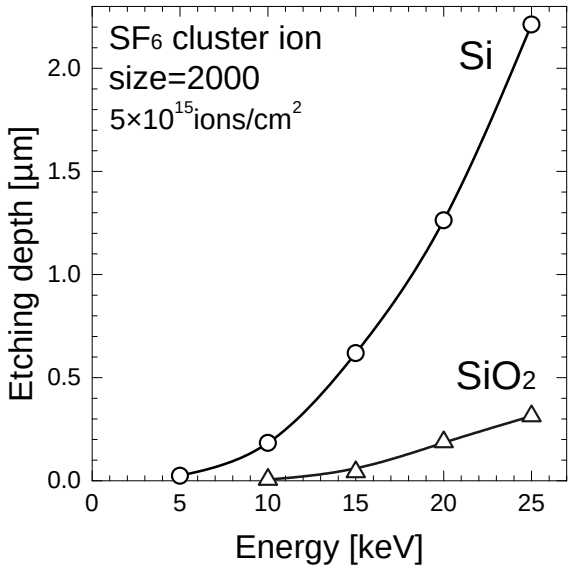

Figure 5.5: Energy dependence of etching depth of Si and SiO_2 with SF_6 cluster ions at ion dose of 5×10^{15}ions/cm^2.

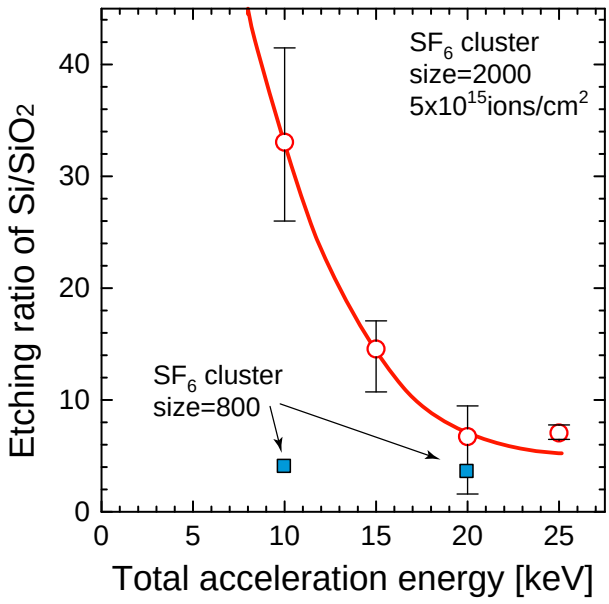

Figure 5.6: Energy dependence of the etching ratio of Si to SiO_2. The average cluster size was 2000 and 800molecules/cluster, respectively.

were also plotted. It should be noticed that the extraction voltage was set higher (V_{ext}=500V) than usual to extract smaller size cluster ions, which caused the mixing of the amount of monomer ions in the cluster beam. The average size of SF_6 cluster ions in this extraction condition was 800 molecules/ion. From Fig. 5.6, there was no dependence of the etching ratio on the acceleration energy because physical sputtering became dominant in this size range. From these results, the etching ratio with a cluster ion beam can be controlled by the cluster size as well as by the total acceleration energy.

5.2.3 Angular Distribution

As the sputtering effects with cluster ions occur near the surface region, the angular distribution is affected by the surface states of the target. When the projectile ion reacts with the target atoms, compound products are generated on the surface as a consequence of the chemical reactions, which increase or decrease the sputtering yield. The angular distribution of sputtered atoms is expected to be strongly affected by these chemical reactions[106].

In this section, the angular distributions of atoms sputtered by reactive cluster ion beams were studied on both reactive and non-reactive targets. Tungsten and gold films were used as targets with SF_6 cluster ion irradiation. Tungsten and gold were deposited on Si substrates by sputter deposition and vacuum deposition methods, respectively. As shown in Fig. 5.2, tungsten reacts with SF_6 cluster ions, whereas gold is stable. The Au target suffers only physical sputtering effects from SF_6 cluster ions, whereas SF_6 reacts with tungsten and gives rise to both physical and reactive sputtering effects.

In addition, the atomic masses of gold (197.0) and tungsten (183.8) atoms are almost the same. The mass ratio of impinging ion to target atom is significant in physical sputtering phenomena. Therefore, the effects of chemical reactivity on the angular distributions can be compared without considering the mass ratio of primary ion to target atom.

The experimental setup for the angular distribution measurement was the same as that used for Cu targets with the Ar cluster ions as shown in Fig. 4.11. The sputtered Au and W atoms were collected on Si substrates and, subsequently, their concentrations on Si were measured with RBS. Fig. 5.7 shows the angular distribution of sputtered Au atoms with SF_6 cluster ions. The acceleration energy was 20keV and the incident angles

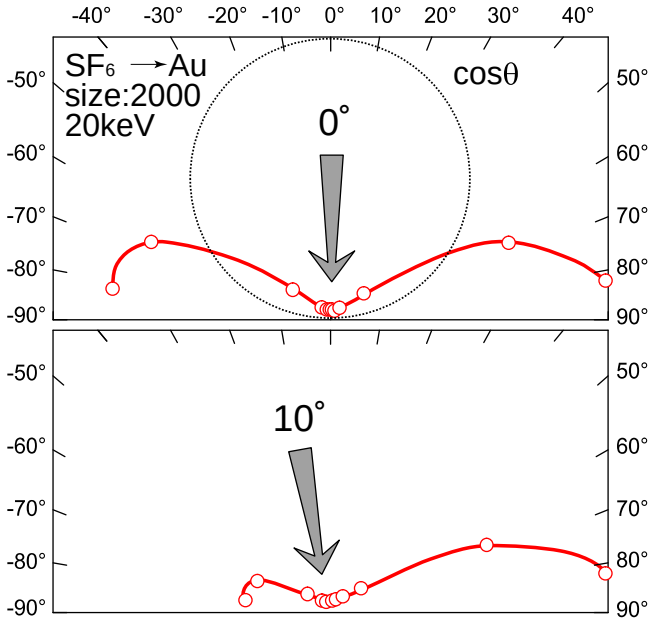

Figure 5.7: Angular distribution of sputtered Au atoms with 20keV SF_6 cluster ions at incident angle of 0° and 10°.

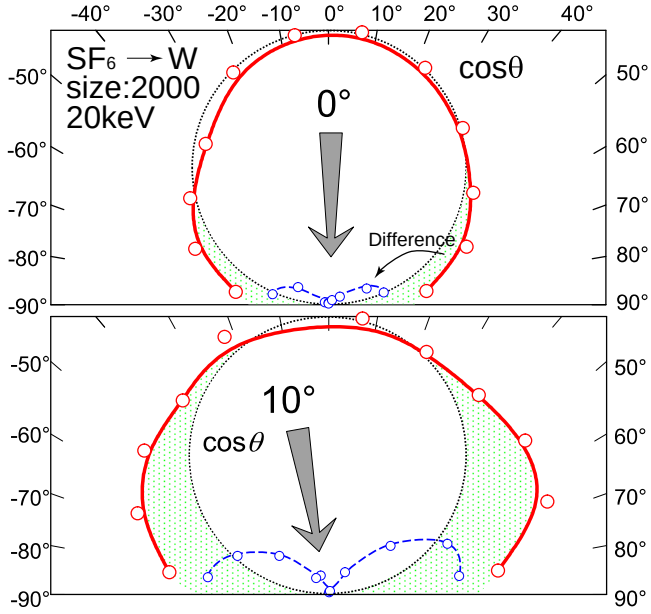

Figure 5.8: Angular distribution of sputtered W atoms with SF_6 cluster ions at incident angle of 0° and 10°. The difference of the yield between the as-measured and the cosine distribution were also plotted by the dotted line in the center.

were 0° and 10°.

The angular distribution of Au at normal incidence showed a flattened distribution, which was the same as that of Cu with Ar cluster ions. In addition, sputtered Au atoms were distributed in the forward direction at an incident angle of 10°. Since no chemical reaction occurred on the Au surface with SF_6 cluster ions, these angular distributions were only induced by physical sputtering. From these results, the lateral sputtering at normal incidence and the marked change of angular distribution at near normal incidence is intrinsic to the physical sputtering by every kind of cluster ion.

Fig. 5.8 shows the angular distribution of W with SF_6 cluster ions. In contrast to the Au, the distribution with SF_6 cluster ions almost followed a cosine law at normal incidence. As discussed in section 5.2.1, tungsten reacted with fluorine and produced reaction products such as WF_6. WF_6 is a volatile material and was thermally evaporated from the surface isotropically. As a result, the angular distribution followed a cosine law. Even at an oblique impact, the angular distribution was almost isotropic. This was completely different from the behavior of Ar cluster ions on a Cu surface or that of SF_6 cluster ions on an Au surface at oblique impact, which showed asymmetric distribution to the forward side of the incident direction.

However, the number of sputtered particles at high angles (near to the surface) was larger than expected from the cosine law (shown as a circle). The difference of the yield between the as-measured and the cosine distribution were also plotted by the dotted line in Fig. 5.8. This extra yield showed an under-cosine distribution and was similar to that of Cu with Ar cluster ions. This could be attributed to the physical sputtering effects of SF_6 cluster ions on W.

Chemical reaction was a dominant etching process at this energy level. However, the contribution from physical sputtering with reactive cluster ions showed the same distribution as with the Ar cluster ions. Therefore, both physical and chemical sputtering effects were contained in the SF_6 cluster impact, and the angular distribution became isotropic when chemical reactions were dominant. The surface smoothing effects are strongly influenced by the angular distributions of the sputtered atoms as discussed in chapter 6.

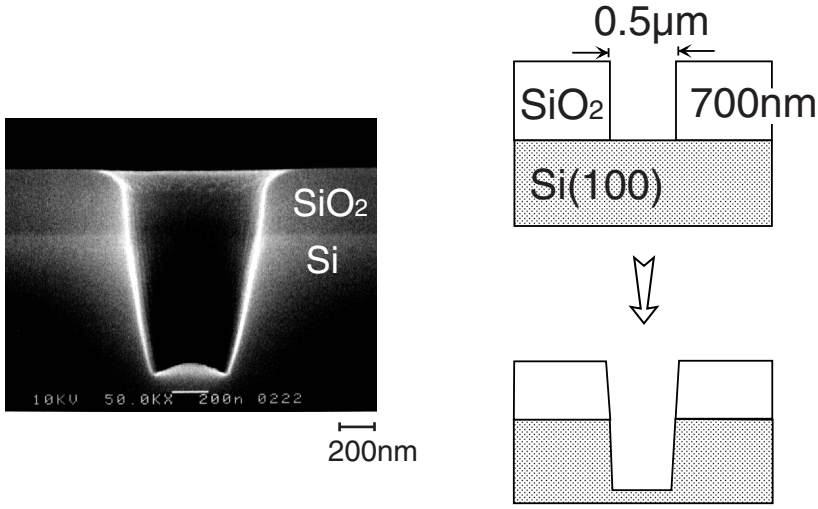

Figure 5.9: Etching of Si with 0.5μm diameter of SiO_2 mask

5.3 Microetching

Anisotropic etching using reactive cluster ion beams has been verified from the observation of the etching pattern profiles[107]. Fig. 5.9 shows a Scanning Electron Microscope (SEM) image of a Si(100) substrate etched with 20keV SF_6 cluster ions at normal incidence. The Si surface was covered with a patterned SiO_2 mask 700nm thick with a 0.5μm diameter opening hole. The ion dose and the average cluster size were 1×10^{15}ions/cm^2 and 2000molecules/atom. The substrate was at room temperature.

From Fig. 5.9, anisotropic etching of Si by SF_6 cluster ions was verified, and etching under the SiO_2 mask was not observed. If the direction of the ion trajectory were dispersive or was curved as would be caused by the charging up of the patterned mask, the side wall of the hole would be etched, and would have resulted in curvature at the bottom part of the wall. As only energetic cluster ions penetrated into the hole, the trajectories were almost perpendicular to the hole openings. In addition, charging up of the mask was less significant in the cluster ion beam process because the mass to charge ratio of the clusters was quite high.

In the Fig. 5.9, a taper structure was observed on the side walls. This structure originated from the spread of the SiO_2 mask by cluster ion bombardment. This spread of the mask could be avoided by using a multi-

layer resist which was more durable against the ion bombardment[108] in place of the SiO_2 mask.

It is very difficult to achieve such anisotropic etching with a fluorine based plasma etching at room temperature because of the fluorine radicals in a plasma. To avoid isotropic etching with fluorine radicals, additional treatments such as cooling of the substrate or protective formations for the side walls[109] have been proposed. In the case of the reactive cluster ion beam, anisotropic etching is possible without these treatments.

In this experiment, the cluster ion current density was $2\mu A/cm^2$ at the acceleration energy of 20keV. From the etching depth of Si substrate, the etching rate of Si with SF_6 cluster ion beams was $0.2\mu m/min$. To apply the reactive gas cluster ion beam process in the industrial fields, much higher cluster ion current density will be required.

5.4 Summary

The reactive sputtering phenomena associated with reactive cluster ion beams were discussed in this chapter. Reactive cluster ions enhanced the chemical reactions between cluster and target atoms, thus the etching processes were completely different from those with Ar cluster ion beams. Applications of the reactive cluster ions were also demonstrated on Si substrate with a fine patterned mask. The results were summarized as follows:

1. The reactive cluster ions enhanced the sputtering yields as a consequence of chemical reactions. In the case of Si with SF_6 cluster ions, the yields were almost two orders of magnitude higher than those with Ar cluster ions.

2. When a cluster impacted the target, dissociation of the SF_6 molecule occurred as well as fragmentation of SF_6 cluster ions. The dissociated fluorine atoms reacted with Si and volatile materials such as SiF_4 were emitted isotropically from the surface.

3. When a chemical reaction was the dominant etching process, the angular distribution became isotropic caused by the evaporation of volatile products. The angular distribution was not sensitive to the incident angle compared with that of Ar cluster ion. However,

the reactive cluster ions involved a physical sputtering effect, which showed an under-cosine distribution.

4. The etching depth of Si and SiO_2 increased exponentially with the acceleration energy. Even when the acceleration energy was below the threshold for physical sputtering with Ar cluster ions, a Si substrate was etched to depth of several hundreds of Å with SF_6 cluster ions. In addition, the etching ratio of Si to SiO_2 decreased with the acceleration energy. Chemical reaction was the dominant etching process in this region. The etching ratio could be controlled by both the total acceleration energy and the cluster size.

5. Etching of a Si trench through a SiO_2 mask with 0.5μm diameter hole was performed with SF_6 cluster ions. There was no etching underneath the mask or curvature of the side walls. The anisotropic etching of the Si trench could be made possible by SF_6 cluster ions without any treatment such as protective wall fabrication or cooling of the target.

Chapter 6

Surface Smoothing Effects and Mechanisms

6.1 Surface Smoothing Effects

6.1.1 Introduction

Among the many possible surface smoothing techniques, mechanical polishing has a very old history. The principle of mechanical polishing is explained as follows; polishing particles which are harder than the target material are forced on the surface by a polisher. As a result, the stress is concentrated at the hills on the surface, and it induces local deformation and destruction. The volume of local deformation depends on both the diameter of the polishing particles and on the force of the polisher. In general, the surface roughness is improved with decreasing the minimum unit of the deformed and destroyed area. As well as a physical mechanical polishing, chemically assisted mechanical polishing has been developed.

Chemical Mechanical Polishing (CMP) is used for the surface smoothing of semiconductors such as Si and GaAs[110]. In the CMP process, polishing particles are mixed in the solution which is reactive with the target material. The polishing particles generate a high temperature and high pressure region, and as a result, chemical reactions between solution and target are enhanced locally. The chemical products are subsequently removed by the polishing particles.

However, CMP involves disadvantages in principle. Since mechanical polishing uses a large polisher, it is difficult to apply a mechanical polishing process to a surface with small 3D structures or to an object

which has weak mechanical strength, such as a thin film. Also, polishing is carried out in a wet condition so that it is difficult to control the surface condition during polishing. To solve these problems, energetic beam polishing with electrons, photons or ions are applied for surface smoothing in a dry condition instead of by mechanical polishing. In the case of ion beam polishing, the polishing conditions can be easily controlled by various parameters, such as ion species, acceleration energy, incident angle, ion dose and ion flux density.

Since the smoothing proceeds by removing the atoms from a hill, a high sputtering yield of atoms from the hill is required. In general, normal incidence of a single ion induces deep penetration of ion and damage formation, resulting in low sputtering yield. Therefore, surface smoothing with single ions is performed at an oblique incidence. Although many results for various materials have been reported, the smoothing speed is very low and it sometimes induces ripple formation on the surface.

In the case of cluster ions, the total energy is deposited in the near-surface region and large numbers of atoms are sputtered from the surface even at normal incidence. As shown in Fig.4.12 and 4.14, the sputtered particles have lateral momentum, and the angular distribution changes suddenly at off-normal incidence. From the molecular dynamics simulations, these motions of atoms were expected to cause a surface smoothing effect. In this chapter, the surface smoothing effect with a cluster ion beam and its mechanism are discussed. In addition, various applications of surface smoothing with cluster ions are demonstrated.

6.1.2 Surface Smoothing with Ar cluster ions

Surface Smoothing with Cluster Ions

To study the difference of the surface smoothing effect between monomer and cluster ions, surface morphologies of Cu targets were observed with AFM. Cu films were deposited on Si substrates by sputter deposition and were irradiated with Ar monomer and cluster ion beams at normal incidence. The target temperature was ambient. After irradiation, the surface morphology of the Cu target was observed with AFM. The scanning area of AFM was 1μm$\times 1\mu$m or 10μm$\times 10\mu$m. The irradiation area of cluster ion beams was 5mm$\times$5mm and the cluster ion beams were scanned with two pairs of deflectors to obtain uniformity. To evaluate the surface smoothness, the average surface roughness R_a was defined as

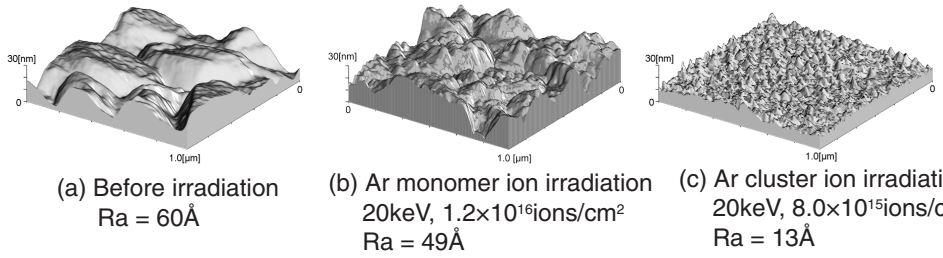

Figure 6.1: AFM images of Cu surfaces irradiated with Ar monomer and Ar cluster ions. The total acceleration energy was 20keV.

follows.

$$R_a = \frac{1}{x_{\max} \cdot y_{\max}} \int_0^{x_{\max}} \int_0^{y_{\max}} |h(x,y) - \overline{h}| dxdy \tag{6.1}$$

where, $x_{\max}$, $y_{\max}$, $h(x,y)$ and $\overline{h}$ are number of points in x and y axes, the height at an arbitrary point (x,y) and the average height of the surface, respectively.

Figure 6.1(a)∼(c) show AFM images of Cu surfaces irradiated with 20keV Ar monomer and Ar cluster ion beams. The average cluster size was 2000 atoms/cluster. The ion doses were 1.2×10^{16} ions/cm^2 with Ar monomer ions and 8.0×10^{15}ions/cm^2 with Ar cluster ions. The initial Cu surface (Fig.6.1(a)) had many grains 400nm wide and 15nm in height, and the average roughness was 60Å. Following Ar monomer ion bombardment (Fig.6.1(b)), there were still many grains on the surface and small hillocks caused by the energetic ion bombardment were observed. The average roughness of this surface was 49Å, which means that the surface roughness was little improved by 20keV Ar monomer ions at normal incidence.

When the Cu target was irradiated with 20keV Ar cluster ion beams with cluster size of 2000atoms (Fig.6.1(c)), the average roughness was reduced to 13Å, which was almost one fifth of the initial value. Considering that the ion dose was 2/3 of that with monomer ions, the Cu surface was smoothed more effectively with Ar cluster ions. In monomer ion sputtering, it has been reported that anisotropy of sputtering yield depends on the presence of facets or grain boundaries. From Fig. 6.1(c), no grains were observed on the surface and there seemed to be little dependence of sputtering yield with cluster ions on a grain boundaries or facets. As well as Cu targets, other metals, semiconductors and insulator

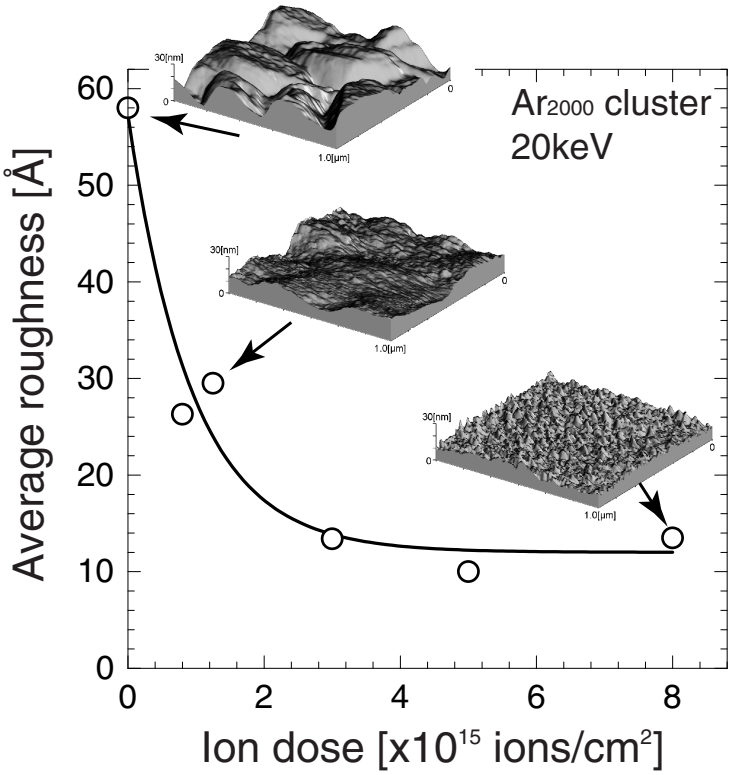

Figure 6.2: Ion dose dependence of the surface roughness of Cu irradiated with 20keV Ar cluster ions.

surfaces were smoothed with cluster ions.

Ion Dose Dependence

Figure 6.2 shows the ion dose dependence of the average roughness of the Cu surfaces bombarded with 20keV Ar cluster ion beams at normal incidence. The ion dose ranged from 8×10^{14} to 8×10^{15}ions/cm^2 and the average cluster size was 2000atoms/cluster. In addition to the average roughness, AFM images at each ion dose are shown.

From Fig.6.2, the average roughness decreased monotonically with increasing ion dose from the initial value of 60Å to 13Å at an ion dose of 8×10^{15}ions/cm^2. In the case of monomer ion irradiation at normal incidence, the surface roughness became worse with ion dose due to erosion or bubble formation inside the target[111]. However, no roughening

mechanism was observed with Ar cluster ion irradiation upon increasing dose. The average roughness of the Cu surface saturated at an ion dose of over 3×10^{15}ions/cm^2. As was shown in Fig. 4.8, large craters could be formed by energetic cluster ion impact, and their diameters were proportional to the cubic root of the total acceleration energy. From the molecular dynamics study, the total kinetic energy was deposited into the target isotropically when the energy per atom of a cluster was less than 1keV/atom. Therefore, the height, depth and width of the rim and holes of the crater increased with the acceleration energy, which would result in a higher saturation value of the average roughness.

To compare the smoothing effects at different acceleration energies, the relation between sputtered depth and the average roughness was studied as a function of acceleration voltage. Since the sputtered depth increased with energy, the surface smoothing effect should be compared not relative to the ion dose but relative to the sputtered depth necessary to reduce the influence of initial surface roughness. If the surface roughness decays faster at the same sputtered depth, it indicates a higher smoothing effect.

Fig. 6.3 shows the relation between the average roughness and the sputtered depth of Cu with Ar cluster ions. The open circles with a full curve referred to the average roughness caused by 20keV Ar cluster ions with an ion dose of 8×10^{14} to 8×10^{15} ions/cm^2, and other points were the average roughnesses from 10 to 25 keV Ar cluster ion irradiations with ion dose of 5×10^{15} ions/cm^2.

When the acceleration energies were 10, 15 and 25keV, the average roughness with all acceleration energies was located near the solid line, which means that there was no significant difference in smoothing efficiency compared with that of 20keV Ar cluster ions. However, the average roughness with 10 and 15keV Ar cluster ions was situated a little lower than the curve, whereas that of the 25keV Ar cluster ion was located a little above the curve. As shown in Fig.4.8, the crater diameter increased with the acceleration voltage, and in the case of a 100keV Ar cluster ion, it was 1.7 times larger than that of a 20keV Ar cluster. The impact of the high energy cluster ion will cause a higher saturation value than that assisted with a low energy irradiation.

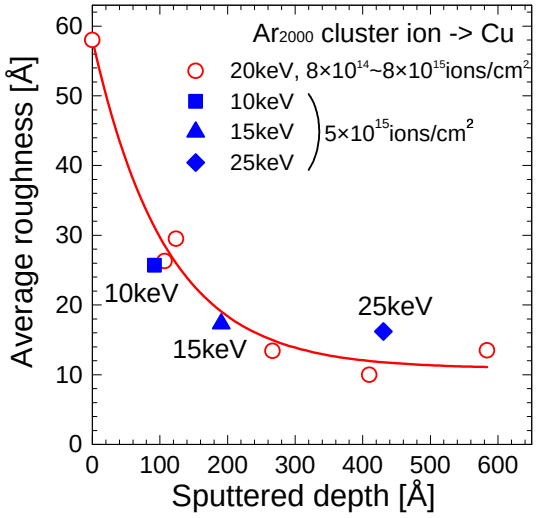

Figure 6.3: Sputtered depth dependence of the surface roughness of Cu irradiated with Ar cluster ions. The acceleration energy was in the range from 10 to 25keV.

6.1.3 Incident Angle Dependence

Ripple Formation

The principle of ion polishing is to move the atoms located near the top of a hill. Since atoms located on a hill have smaller binding energies than those in a valley, only the atoms on the hill can be moved without inducing dislocation of the atoms in the valley if an appropriate energy is supplied. Also the kinetic energy of the projectile ions should be sufficiently low so that atoms are not induced to move perpendicularly into the target. To achieve these aims, a glancing angle of incidence is frequently used for the surface smoothing with monomer ions.

However, a high-fluence ion bombardment produces a variety of surface topological features. The most interesting feature is a ripple or wavelike structure developed on metals (Ag(110)[112]), semiconductors (Si[114, 115], Ge(001)[113], GaAs[116, 117]) and insulators (SiO_2[118], glass[119]). This ripple formation is problematic in many applications, including secondary ion mass spectroscopy (SIMS)[120], depth profiling of Auger electron spectroscopy(AES)[121, 122] and ion milling[123]. In a typical SIMS apparatus, the incident angle of the primary ions is oblique to obtain high sputtering yield and to avoid ion mixing. As sputtering proceeds,

ripples are formed on the surface which induce degradation of the depth resolution.

Ripple formation at glancing incidence of monomer ions was first modeled by Bradley and Harper[124]. They considered it as a competition between the local curvature dependence of the sputtering yield and thermal diffusion on the surface. This theory agreed well with many experimental results. However, it could not explain the lack of ripple formation for small incident angles nor the insensitivity to both temperature and ion energy[125]. Carter and co-workers suggested that ion and atom-atom collision processes provided a ballistic atomic motion parallel to the surface in addition to the generally accepted isotropic diffusivity[125].

However, there is no data regarding ripple formation under cluster bombardment. Cluster ion sputtering effects are strongly affected by the dense energy deposition in a local area, which creates a spike cascade, and crater and shockwave formation near the surface. The sputtering phenomena with cluster ions are completely different from those with monomer ions, such as incident angle dependence of the sputtering yield and the angular distribution of sputtered atoms, termed 'lateral sputtering'. Therefore, the incident angle dependence of the surface smoothing induced by cluster ion bombardments is expected to be totally different.

Surface Smoothing Effects at Oblique Impact

Figure 6.4 shows AFM images of Cu surfaces irradiated with Ar cluster ions at several incident angles (0°, 15°, 30°, 45° and 60°)[128]. The average roughnesses of the Cu surfaces obtained from the AFM observations were plotted in Fig. 6.5. The average size of the Ar cluster ions was 2000atoms/cluster. The acceleration energy and the ion dose were 20keV and 5×10^{15}ions/cm^2, respectively. The initial Cu surface was shown in Fig. 6.4(a), and its average roughness was 60Å in a 1μm×1μm area.

In the case of the incident angle of 0° (Fig. 6.4(b)), the Cu surface was smoothed, and its average roughness became 10Å. On increasing the incident angles to 15° and 30° (Fig. 6.4(c) and (d)), distortions began to appear on the surfaces. Although the surface smoothing effect degraded with incident angle, the surface roughness was improved from the initial value of 60Å to 19Å and 44Å, respectively, at incident angles of 15° and 30°.

When the incident angle exceeded 45°, the surface roughness increased and ripples whose wave vector was parallel to the incident direc-

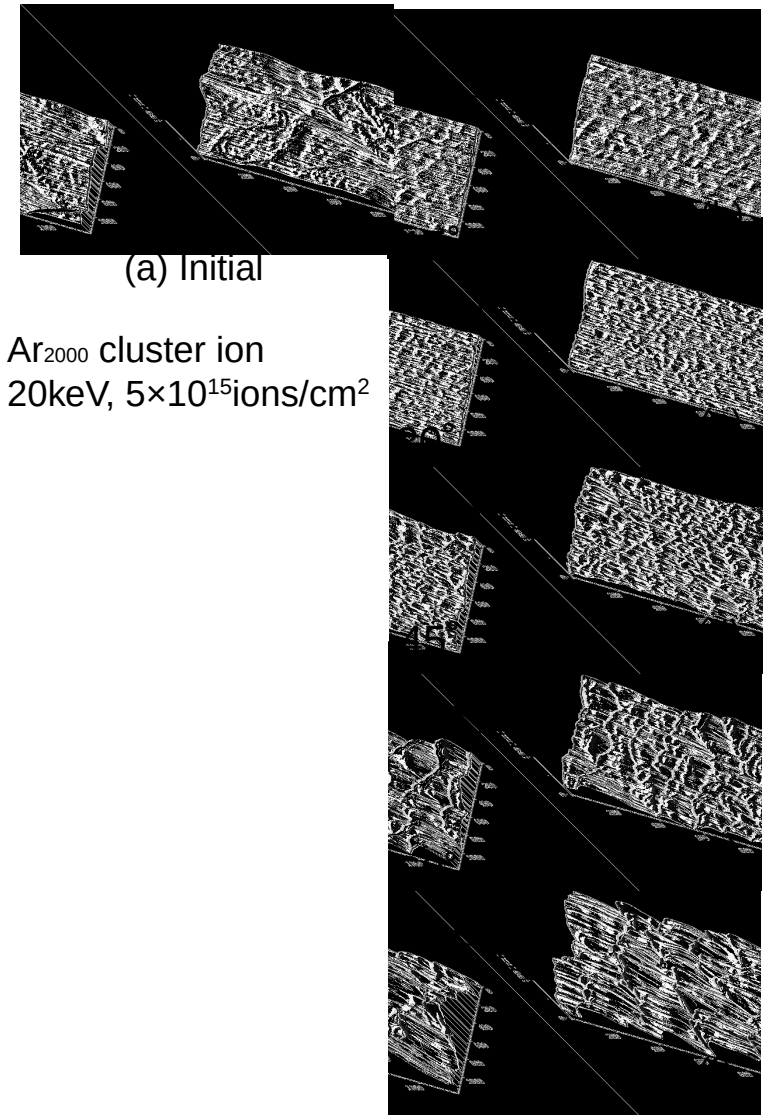

Figure 6.4: AFM images of Cu surface irradiated with Ar cluster ions at various incident angles from 0° to 60°. The acceleration energy and the ion dose were 20keV and 5×10^{15}ions/cm^2, respectively.

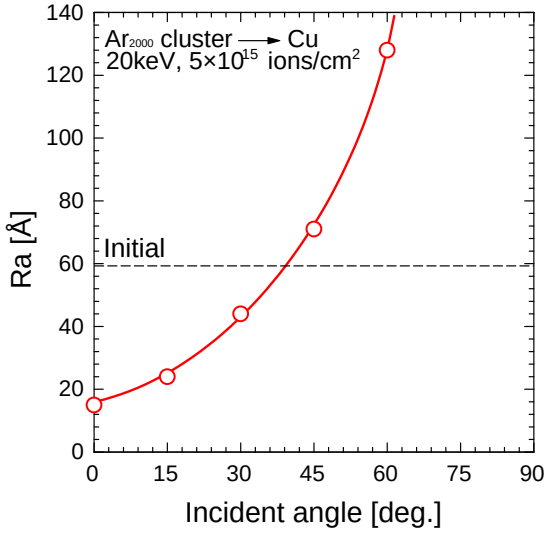

Figure 6.5: Incident angle dependence of the surface roughness.

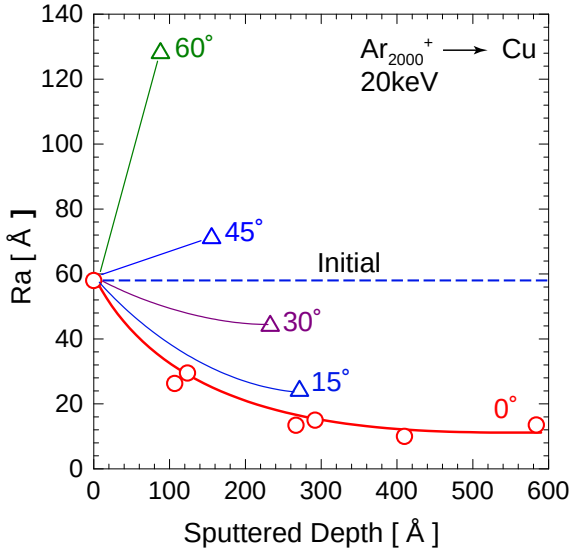

Figure 6.6: Incident angle dependence of the surface roughness on the sputtered depth.

tion appeared. The wavelength of the ripple produced by a 60° impact was about 0.2μm. The average roughnesses at incident angles of 45° and 60° were 71Å and 113Å, respectively, which were higher than the initial value of 60Å. Thus, surface roughening with ripple formation occurred at high incident angles with cluster ions. These ripple formations at glancing angles were also observed on silver surfaces.

To confirm that the increase of the surface roughness at oblique impact was not due to the reduction of the sputtered depth, the relation between the sputtered depth and the average roughness was shown in Fig. 6.6. As well as the results at various incident angles at a dose of 5×10^{15}ions/cm^2, ion dose dependence at normal incidence was plotted. If the surface smoothing effect at an oblique incidence was the same as at normal incidence, the data points should lie on the same line as at normal incidence, but this was not the case. In the case of an incident angle of 60°, Cu was sputtered to a depth of about 100Å, and its average roughness was 130Å, which was 5 times higher than that of normal incidence at the same sputtered depth. Therefore, it is clear that a surface roughening mechanism exists at oblique incidence.

In the case of a monomer ion beam at a glancing angle of incidence, rotation[126] or rocking of the target[127] is performed during irradiation, which prevents the steady state of ripple formation, and leads to a smooth surface. In the case of cluster ions at normal incidence, while lateral motions of atoms occurred on the surface, the direction in the horizontal plane was random. This non-directional motion of the atoms did not cause steady state ripple formation. In contrast, one-directional motion of the atoms was observed at off-normal impact of cluster ions, which resulted in steady state ripple formation, the same as with monomer ions. In the case of monomer ion irradiation, periodic structures are rarely observed on metal surfaces because the diffusion mobility of vacancies and adatoms is high[112]. However, since ripples were formed on a metal surface with cluster ion beam irradiation, thermal diffusion was expected not to be the main reason for the smoothing or roughening with cluster ions.

6.1.4 Surface Smoothing with Reactive Cluster Ions

From the discussion in the previous section, the surface smoothing with Ar cluster ions was influenced by the lateral motion of atoms, termed 'lateral sputtering'. However, in the case of reactive cluster ions, the an-

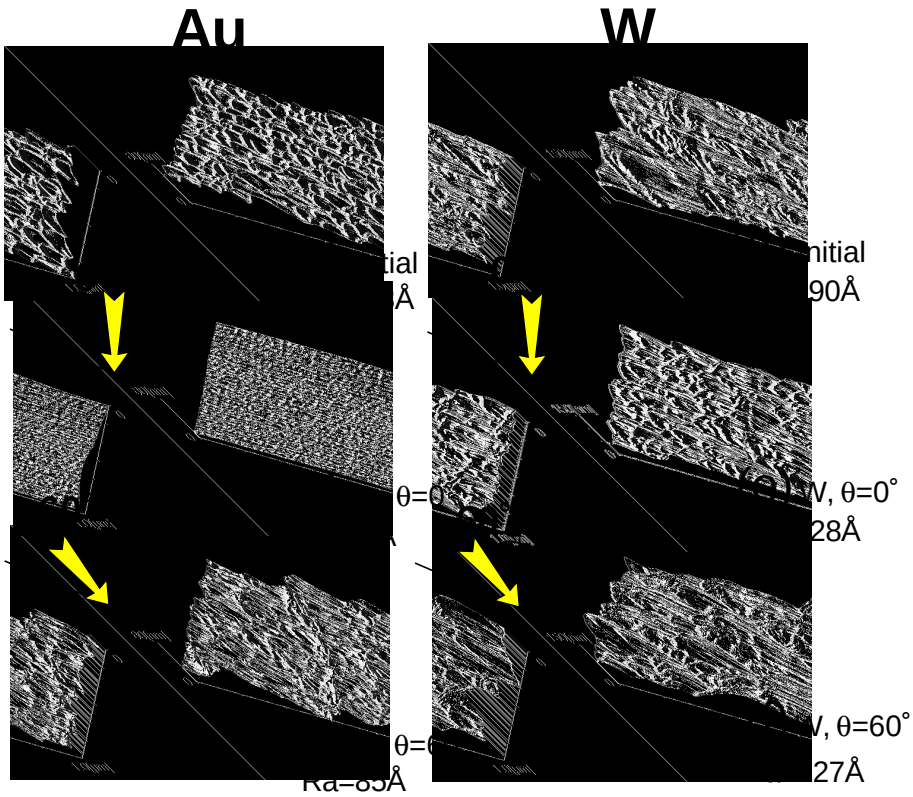

Figure 6.7: Surface morphology of Au and W surfaces irradiated with 20keV SF_6 cluster ions at normal and oblique incident angles. The ion dose was 7×10^{15}ions/cm^2.

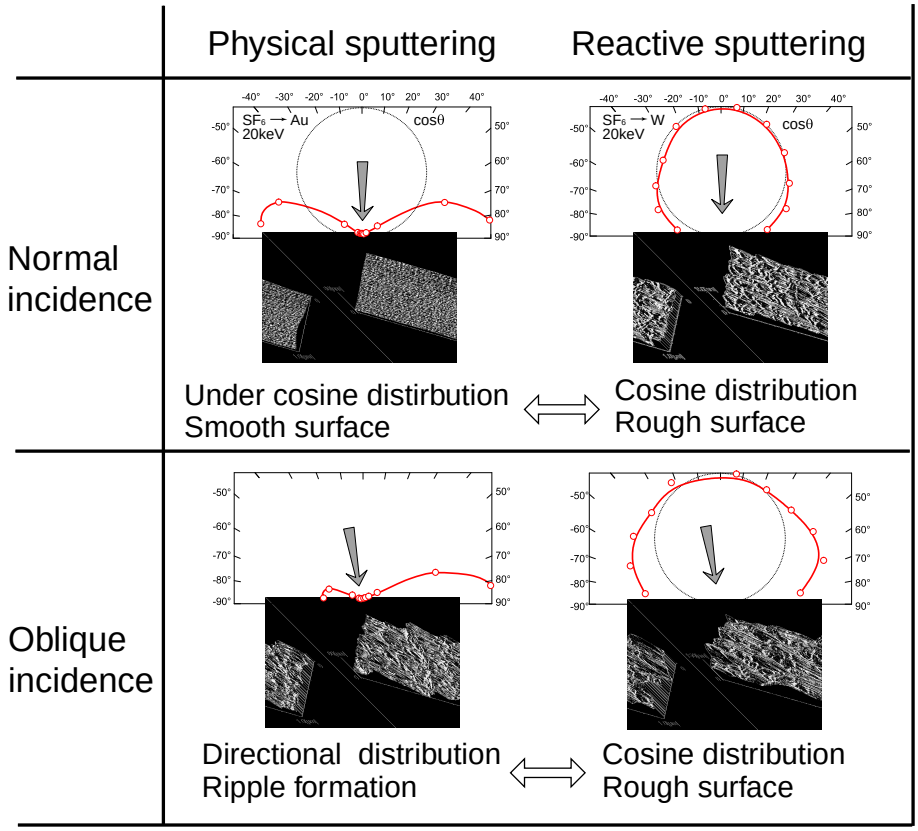

Figure 6.8: Comparison of the surface smoothing effects and angular distribution of sputtered atoms on Au and W surface irradiated with SF_6 cluster ions.

gular distribution of the sputtered atoms was completely different from that with Ar cluster ions. As shown in Fig. 5.7 and 5.8, the angular distribution of Au with SF_6 cluster ions (non-reactive) at normal incidence showed under-cosine distribution, whereas that of W with SF_6 cluster (reactive) followed the isotropic cosine law. In addition, the distribution of sputtered Au changed remarkably at the slightly off-normal incidence of 10°, whereas that of W was almost isotropic. Therefore, a SF_6 cluster ion gives rise to only physical sputtering effects on Au, and gives mainly chemical sputtering effects with some physical sputtering effects on W.

To compare the surface smoothing effects by physical or reactive sputtering, surface morphologies of Au and W irradiated with SF_6 cluster ions were observed with AFM[106]. Fig.6.7 shows AFM images of both Au and W surfaces irradiated with 20keV SF_6 cluster ions at incident angles of 0° and 60°. The ion dose and the average cluster size were 7×10^{15}ions/cm^2 and 2000atoms/cluster, respectively. The initial average roughnesses of the Au and W surfaces were 73Å and 190Å, respectively. AFM images of the Au surface were shown in Fig. 6.7: (a) in the initial condition, and in (b) and (c) after irradiation at incident angles of 0° and 60°, respectively. Fig.6.7(d)-(f) showed the W surface in the initial condition, and after irradiation at incident angles of 0° and 60°, respectively.

In the case of Au, the surface roughness was improved from 73Å to 24Å at normal incidence (Fig.6.7(b)). At incident angle of 60°, the surface roughness was 85Å (Fig.6.7(c)), which was higher than the initial value. There existed a roughening effect at oblique impact with SF_6 cluster ions which was the same as that of Cu with Ar cluster ions at oblique impact. Surprisingly, ripples whose wave vector was parallel to the incident direction were formed at an incident angle of 60°, and were also observed at high angles of Ar cluster impact as shown in Fig. 6.4.

In contrast, the surface roughness of tungsten was not similarly improved by SF_6 cluster ions at normal incidence. The average roughness was slightly reduced from 190Å to 128Å after SF_6 cluster ion irradiation. However, the morphologies of the initial tungsten surface (Fig.6.7(d)) and after irradiation (Fig.6.7(e)) were almost the same. Even when the incident angle was tilted to 60°, the surface roughness showed a slight increase from 190Å to 227Å, and no ripple formation was observed(Fig.6.7(f)).

As shown in Fig. 5.8, the angular distribution of tungsten atoms sputtered by SF_6 cluster ions was isotropic and the oblique impact did not show any marked difference in the angular distribution. This caused poor surface smoothing effects on W by SF_6 cluster ions. However, the angular

distribution contained a small fraction of a physical sputtering effect so that the tungsten surface was slightly smoothed with SF_6 cluster ions.

The relation between the angular distribution of sputtered atoms and the surface smoothing effect with gas cluster ions was summarized in Fig. 6.8. A marked surface smoothing occurs with gas cluster ions when physical sputtering is the dominant process. Since gold is a stable material, physical sputtering is dominant in this case, and results in a smoother surface. Not only the surface smoothing effect, but also ripple formations at glancing angle are intrinsic physical sputtering effects. In the case where chemical reaction is the dominant etching process, the angular distribution is isotropic and cluster ions show little surface smoothing. The physical sputtering (lateral sputtering) of gas cluster ions is significant for surface smoothing as predicted by the molecular dynamics simulations.

6.2 Surface Smoothing Mechanisms

As discussed above, physical sputtering and lateral sputtering effects are responsible for the surface smoothing produced by cluster ions. In the case of monomer ions, the physical sputtering effect can be described based on the binary collision model. In contrast, a cluster ion deposits its energy in the near surface region, and as a consequence, the energy density and collision frequency are too high to describe the impact process with linear cascade theory.

A molecular dynamics simulation describes the precise motion of atoms according to the Newton equation, however it is not suitable to describe stochastic phenomena. In this study, a discrete stochastic model which describes the atomic motion of physical sputtering induced by cluster ions has been proposed. Similar approaches have been used for the study of surface smoothing or roughening with monomer ion irradiation at glancing angles[129]. However to date, there has been no study concerning surface smoothing with cluster ions.

To describe the atomic motion induced by cluster ion impacts, a simple model based on the experimental results with Ar cluster ions was proposed. Monte-Carlo simulation of surface smoothing effect was performed with this model, and the surface smoothing mechanism with cluster ion is discussed in this section.

6.2.1 Monte-Carlo Simulation of Surface Smoothing

Physical Sputtering Model of Cluster Ion Impact

The sputtering effects with Ar cluster ion beams were studied in chapter 4. The following are the characteristics of the physical sputtering effects caused by cluster ions with energies of a few eV/atom.

1. **Lateral Sputtering**
   The angular distribution of the sputtered atoms at normal incidence follows an under-cosine distribution, which is not directional in the plane of the target. The angular distribution of sputtered atoms changes from an isotropic distribution to a directional one at a slight off-normal incidence. Even at an incident angle of 10°, most of the sputtered and ejected atoms are distributed in the forward direction. This lateral motion of atoms due to cluster ion impact is termed 'lateral sputtering'.

2. **Movement of Ejected Atoms**
   From a microscopic point of view, a large crater (a few tens of nanometers in diameter) is formed when an energetic cluster impacts upon a surface. As a result, large numbers of atoms are ejected from the crater, and the majority of them are moved to around the crater, depending on the incident angle. The dislocated atoms form a doughnut shaped rim at normal incidence, and a large mound in the forward direction at oblique incidence.

3. **Sputtering Yield**
   The sputtering yield and volume of the crater increase linearly with the acceleration energy. Both the sputtering yield S and the number of ejected atoms from a crater E are proportional to $\cos\theta$. Although impact of a cluster forms a large crater, the number of sputtered atoms which leave the surface S is very low compared with the number of atoms ejected from the crater E.

From these phenomena, a simple model which describes physical sputtering effects with cluster ions has been proposed. Figures 6.9(i) and (ii) show physical sputtering models at near normal incidence and at an oblique angle of incidence, respectively. At near normal incidence below

a critical angle θ_c ($|\theta| < \theta_c$), a symmetric crater is formed. The critical angle θ_c is defined as the angle where the angular distribution of sputtered atoms changes from an isotropic distribution in the horizontal plane to a directional one. θ_c is estimated to be less than 10°.

In the case of the incident angle below θ_c, the ejected atoms E from a crater move isotropically around the crater. A small fraction of the ejected atoms E leave the target as sputtered atoms S and a large fraction of these ejected atoms E form a rim around the crater. In the following discussions, these dislocated atoms forming the crater rim are represented as D.

From the STM observation of a crater, the sputtering yield by a cluster ion is estimated to be over several thousand atoms/ion assuming that all the atoms in the hole leave the target completely. However, this is inconsistent with the experimental result in Fig. 4.4 ($\leq$60atoms/ion). Therefore, the number of sputtered atoms S is a few % of the ejected atoms E and a large fraction of the ejected atoms E is re-deposited around the crater as dislocated atoms D.

When the incident angle is larger than θ_c ($|\theta| > \theta_c$), the ejected atoms move down the slope as shown in Fig 6.9(ii). In this case, the dislocated atoms D exist only on the downward side, which is the origin of the uni-directional motion at a slope. The STM image of a crater at oblique impact of a cluster confirms this assumption. As the number of ejected atoms E is proportional to $\cos\theta$, both the sputtering yield $S(\theta)$ and the number of dislocated atoms $D(\theta)$ also decrease in proportion to $\cos\theta$.

Monte-Carlo Simulation Method

The Monte-Carlo simulation method for surface smoothing is shown in Fig. 6.10. The target was divided into 256×256 square cells with a height of $h_{i,j}$ ($0 \leq i, j \leq 255$). The number of ejected atoms $E(\theta)$, sputtering yield $S(\theta)$ and the number of dislocated atoms $D(\theta)$ depended on the local incident angle θ. Four neighbors of the point (i, j) along each axis were fitted to a biquadratic function, and the local incident angles of θ_x and θ_y were defined from a derivative of the fitting function at point (i, j). The number of ejected atoms $E(\theta)$, the sputtering yield $S(\theta)$ and the number of dislocated atoms $D(\theta)$ along each axis were obtained from multiplying each value by $\cos\theta_x$ or $\cos\theta_y$.

Each cell was bombarded at random. When an arbitrary point (i, j) with height of $h(i, j)$ was selected, the local incident angles $\theta_x(i, j)$ and

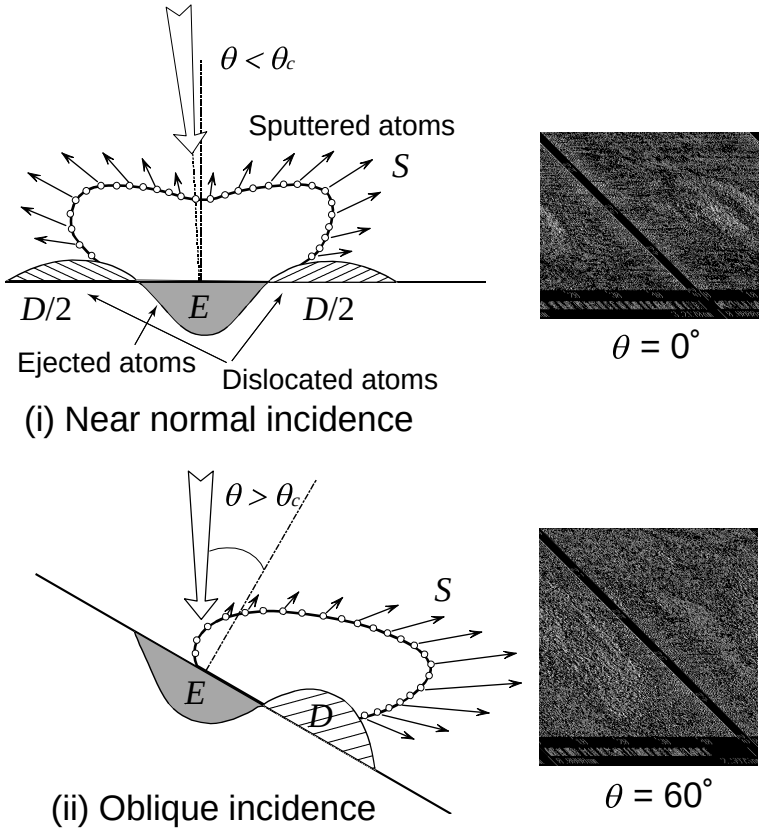

Figure 6.9: The motion of atoms following the impact of a cluster ion at normal and oblique incidence.

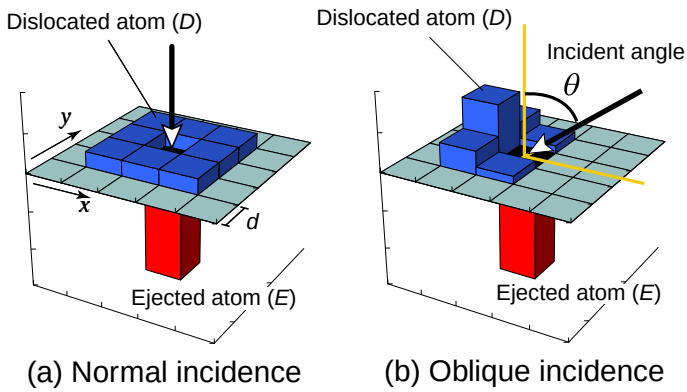

Figure 6.10: The MonteCarlo simulation model for surface smoothing with cluster ions.

$\theta_y(i,j)$ were obtained from the biquadratic fitting function. According to the local incident angles, the number of ejected atoms $E(\theta)$, the sputtering yield $S(\theta)$ and the number of dislocated atoms $D(\theta)$ were defined. After bombardment, the height of the point (i,j) decreased to $h(i,j)$-$E(\theta)$.

If the local incident angle was lower than the critical angle θ_c ($|\theta| < \theta_c$), the same number of dislocated atoms was deposited isotropically on the 8 neighbor cells around the cell (i,j) as shown in Fig.6.10(a). In the case of oblique impact ($|\theta| > \theta_c$), the dislocated atoms were deposited in the forward direction. The number of dislocated atoms on each cell in the forward side was obtained from the partition of the total amount of dislocated atoms by the local incident angle in each axis. This simulation was not dependent on the scale of the cells, however, the width of the cell was defined as 30Å .

The random impacts of the cells were repeated 10^6 to 10^7 times corresponding to an ion dose of 10^{15} to 10^{16}ions/cm^2, respectively. The average roughness, spatial frequency, sputtered depth and images of the surface morphology were obtained from the 2-dimensional height distribution $h(i,j)$. A thermal diffusion process component was not included in this simulation.

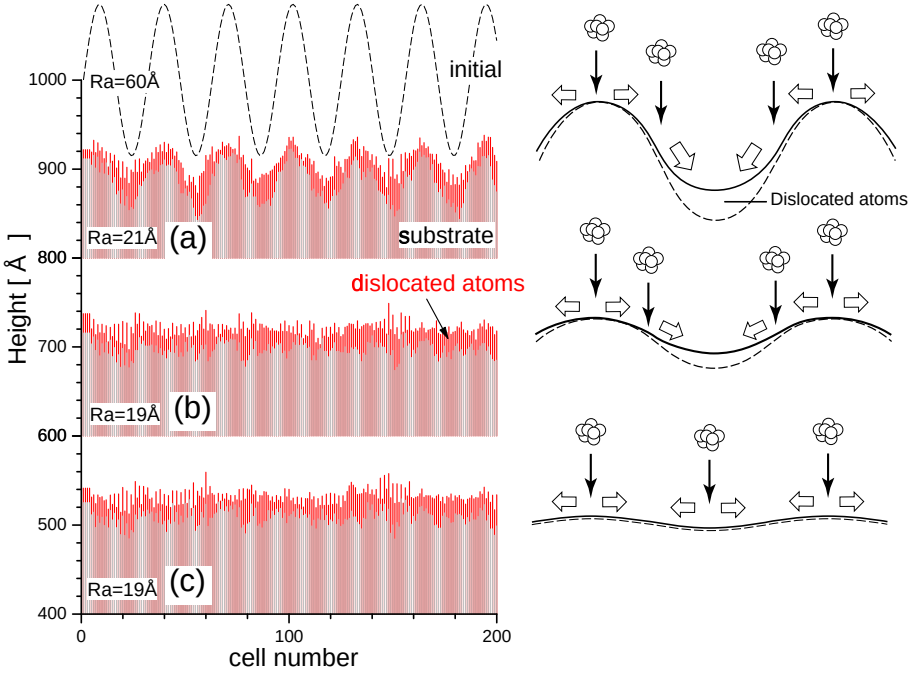

Figure 6.11: Surface smoothing mechanism with cluster ions and the cross-section of the target during sputtering.

6.2.2 Smoothing Mechanism

Smoothing Mechanism

A schematic drawing of the smoothing mechanism with cluster ions and a cross-section during irradiation are shown in Fig. 6.11. The indicated average height of the initial surface was 1000Å, and this height decreased with increasing fluence. The average roughness of the initial surface was set at 60Å. The critical angle θ_c and the number of ejected atoms at normal incidence E_0 were 5° and 600 atoms/impact, respectively. When a cluster ion impacted a surface below the critical angle θ_c, large numbers of atoms were ejected from the crater hole and the dislocated atoms were re-deposited isotropically around the impact point.

In contrast, when a cluster impacted a slope with a high incident angle θ which was greater than θ_c, most of the atoms were dislocated down the slope, and the valley was buried by these dislocated atoms from both side slopes. The dislocated atoms on the target surface were colored black in Fig.6.11, and the filling of the valleys with dislocated

atoms were observed in the upper most figure of the cross-section (a). With further irradiation, the height difference between hill and valley decreased. Once a flat surface was attained, the incident angle of most impinging clusters came within the critical angle θ_c so that an isotropic ejection of the atoms mainly occurred. Therefore, no roughening effect was observed afterwards.

Surface smoothing was accomplished not only by the filling of the valley with dislocated atoms, but also by sputtering to an appropriate depth. From Fig.6.11, the surface was still rough at a sputtered depth of 100Å (Fig.6.11(a)), and a sputtered depth exceeding the bottom of the initial valley was required to obtain a smooth surface. The filling of the valley with dislocated atoms was a transitional state, and subsequently, these transitional dislocated atoms which covered on the valleys were sputtered in the final state. As a result, a flat surface with a very thin layer of dislocated atoms was attained.

In principle, it is unavoidable that a thin damaged layer is formed with cluster ion impacts. In case of a single crystal target, this layer is no longer crystalline and an amorphous layer is generated. However, the damage depth with cluster ion impact at 20keV was less than 100Å and this damaged layer was easily re-crystallized by low temperature annealing. Since the damaged layer becomes thinner with decreasing acceleration energy of the clusters, very thin damaged layers can be maintained with the low-energy cluster ion treatment.

These results suggest that the surface smoothing effect with cluster ions is strongly influenced by the local incident angle. In the following section, the dependence on ion dose, incident angle, critical angle and initial surface morphology are discussed.

Dose and Energy Dependence

Figure 6.12 shows Monte-Carlo simulation results of the dose dependence of the surface roughness at normal incidence. The initial surface prepared for the simulation had a sinusoidal topography with average roughness of 60Å, which corresponded to the experimental case of a Cu surface. The critical angle θ_c was 5°. The number of ejected atoms with a 20keV Ar cluster ion was assumed to be 600atoms/ion, and it was proportional to the acceleration energy.

From Fig.6.12, the average roughness decreased monotonically with the ion dose. This dose dependence showed good agreement with the

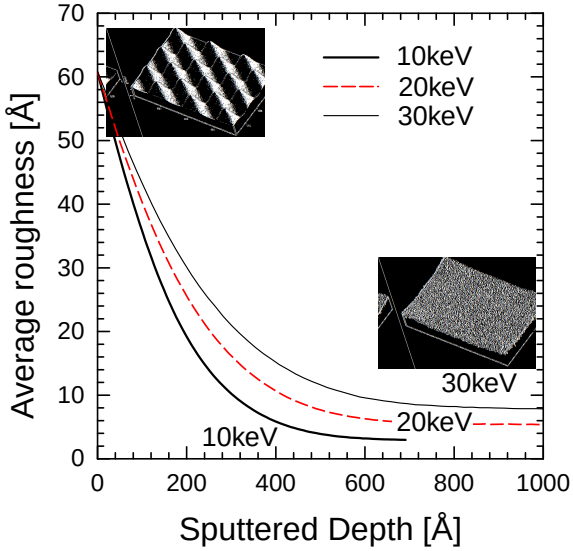

Figure 6.12: Ion dose dependence of the surface roughness with cluster ions at different impact energies. The initial surface roughness was 60Å.

experimental results as shown in Fig.6.2. There was also a saturation value in the high dose region. In the case where the acceleration energy was 30keV, the saturation value was higher than that with 20keV cluster ions. In contrast, the saturation value with 10keV cluster ions was low and the average roughness decreased faster than with 20keV. Since the number of ejected atoms and the crater size becomes larger with the acceleration energy, low energy irradiation is necessary for the final treatment to obtain a very flat surface.

Incident or Critical Angle Dependence

From the incident angle dependence of the surface morphologies shown in Fig.6.4, it is apparent that the surface smoothing with cluster ions was most effective at normal incidence, and the surface roughness increased with incident angle. Fig. 6.13 shows the simulation result of the incident angle dependence of the surface roughness. The incident angle ranged from 0° to 75°. Since the sputtered depth depended on the incident angle, the average roughness was compared at the same sputtered depth. Similar to the case of the experimental results, the surface roughness decreased with increasing sputtered depth at normal and low incident

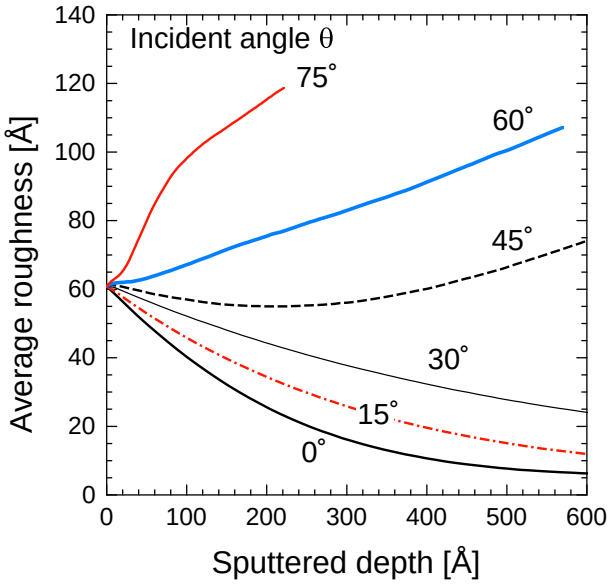

Figure 6.13: Incident angle dependence of the surface roughness.

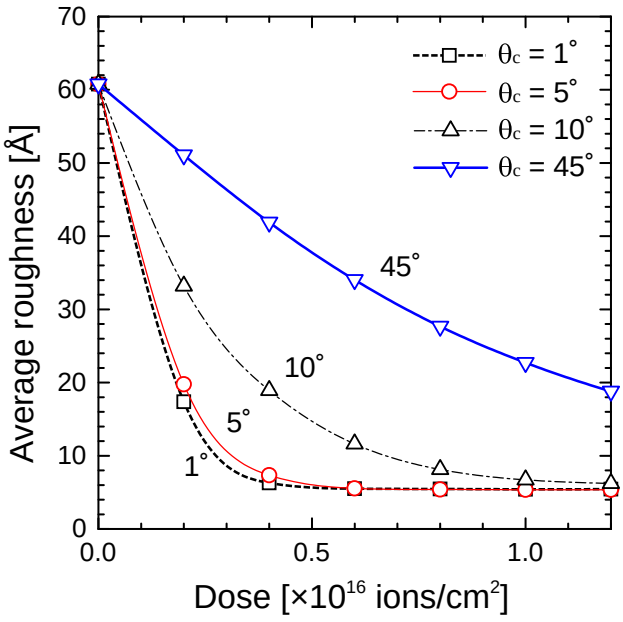

Figure 6.14: Critical angle θ_c dependence of the surface roughness.

angles, whereas there existed a surface roughening mechanism at high incident angles. In the case of oblique impact, a steady state of ripples perpendicular to the incident angle was also observed, which originated from the uni-directional motion of dislocated atoms along the slope.

One of the most unsual sputtering effects in cluster beams compared with monomer ion beams was the dramatic change of angular distribution of sputtered atoms at a slight tilt of the incident angle. From the experimental results, the angular distribution changed from an under-cosine distribution to a directional one at an incident angle below 10°. In this simulation, the transition angle from isotropic distribution to directional one was defined by the critical angle θ_c.

Figure 6.14 shows the critical angle θ_c dependence of the average roughness. The critical angle was varied from 5° to 45°, with ion dose ranging up to 1.2×10^{16}ions/cm^2. When the critical angle was 1°, the average roughness decreased faster and saturated at lower ion doses than those at 45°. The surface smoothing was most effective at θ_c of 1°, and a higher fluence was needed to attain the same average roughness with increasing θ_c. The critical angle θ_c corresponds to the sensitivity of a cluster to perceive the local surface as a slope. In the case of a low critical angle, a valley with very gentle slope was also filled with dislocated atoms and finally the valleys were made plane. On the other hand, even a valley with a very steep slope was not filled in the case of a high critical angle, and this resulted in an insufficient smoothing effect. These critical angles do not exist in monomer ion sputtering, but they are very significant in the smoothing by cluster ions.

Surface Geometry Dependence

From the experimental results on surface smoothing, wider hills and valleys still remained even though those of small size have disappeared. In the case of smoothing of large hills and valleys, it is expected to be difficult to smooth the macroscopic roughness or curvature using cluster ions.

To study the influence of the initial surface morphology, surfaces with various spatial frequencies were prepared. Fig. 6.15 shows the dependence of the average roughness on the surface spatial frequency. The initial surfaces of each target had 1, 3 and 5 pairs of hill-and-valley as shown in Fig. 6.15. As the width of a target was 770nm, the wavelength of the surface with 1, 3 and 5 pairs of hill-and-valley were 770nm, 256nm

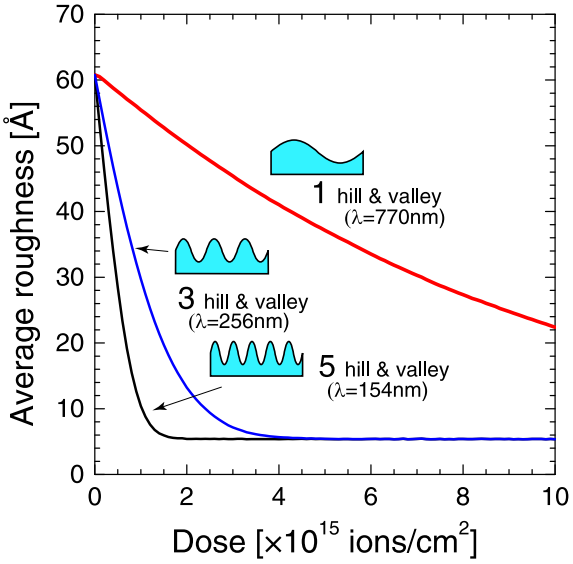

Figure 6.15: Dependence of the surface roughness on the initial surface morphologies.

and 154nm, respectively. The initial average roughness was set to be the same in each case (60Å). The targets were irradiated with cluster ions at normal incidence, and with ion doses ranging up to 1×10^{16}ions/cm^2.

In the case of the surface with high spatial frequency, the decay of the average roughness was rapid and reached the saturation value with a small ion dose. When the surface spatial frequency was low or the size of hill and valley was large, the decay was slower and it needed a greater ion dose to reach the same saturation value as that of the surface with high spatial frequencies. Since the distance of atomic motion induced by one cluster impact was only a few nanometers, it was too short to move the atoms to the bottom of the valley which was a few micrometers in length. The transitional filling of the valley was significant for surface smoothing with cluster ions so that it would be difficult to fill a wide valley. Thus, the hills and valleys with high spatial frequency were smoothed preferentially with low ion dose, and only subsequently were the coarse structures with low spatial frequency smoothed.

From the dependence of the surface smoothing effects on various parameters, such as the incident angle, the critical angle and the initial surface morphology, it is clear that the surface smoothing with cluster

ions is influenced by the local incident angle. This incident angle dependence is intrinsic to the sputtering with cluster ion and is expected to originate from the localization of the energy density in the substrate.

6.3 Applications of Surface Smoothing

From the Monte-Carlo simulations, the surface smoothing mechanism was made clear and it was revealed that the lateral sputtering effect was significant for surface smoothing by cluster ions. Since the surface smoothing with gas cluster ion beams can be carried out at normal incidence and low ion doses, various applications are anticipated. In terms of the sputtering yields, gas cluster ion beams showed very high sputtering yields for diamond and SiC, which are very hard materials and are usually difficult to smooth. In addition, cluster ions showed little selective sputtering effect in compound materials. In this section, a diamond film, SiC and YBCO superconducting films which have rough surfaces in the as-deposited condition were treated with gas cluster ion beams, and the possibilities of using gas cluster ion beam for nano-processing are discussed.

6.3.1 CVD Diamond Films

Introduction

A polycrystalline diamond film deposited by a Chemical Vapor Deposition (CVD) technique[130)] is a promising material. For example, a diamond film is an ideal material for a membrane which supports the mask patterns of X-ray lithography because stability against X-ray radiation, high Young's modulus, high heat conductivity and high transparency are required for this purpose[131)]. In addition to use as a membrane material, CVD diamond films are expected to be applied for the coating of cutting tools, for wide gap semiconductors, for surface acoustic wave (SAW) devices, for cold emitter arrays in flat panel displays (FPD), etc.

However, there are many crystallites with pyramidal structure on an as-deposited CVD diamond film and the surface roughness is high due to this morphology. Even for optimal deposition conditions, the size of the crystallites is about 300nm and the surface roughnesses are between 20 and 40nm for 1 to 2μm thick diamond films[132)]. In the case of other membrane materials, such as CVD deposited SiC and SiN_x, the surface

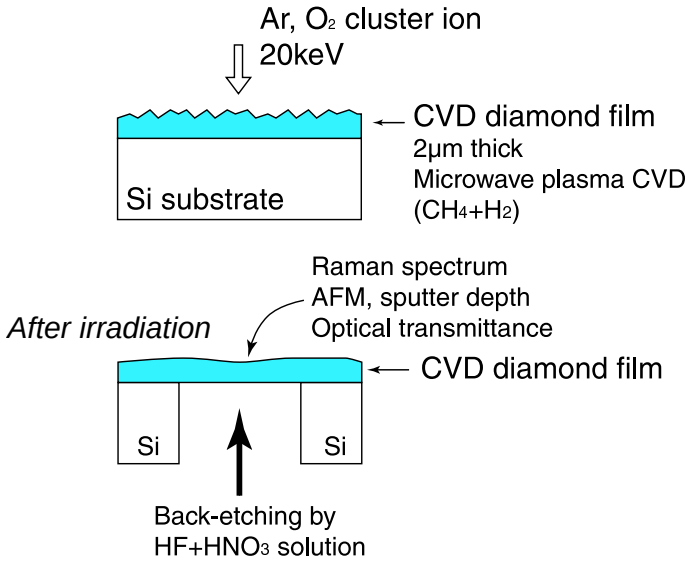

Figure 6.16: Experimental procedure of CVD dimond films irradiated with gas cluster ions.

roughnesses of 2 to 5nm are standard values. So there are requirements to develop new surface smoothing techniques for CVD diamond films.

To date, Chemical Mechanical Polishing (CMP)[133], ion beam modification at grazing angle[134], the etch-back method[135] and plasma etching[136, 137] have been studied for surface smoothing of CVD diamond films. However, there are many problems with these smoothing techniques. For example, the etch-back method induces the contamination by resist materials. Ion beam modification at grazing angle gives a slow etching rate and induces damage in the diamond films. The mechanical polishing technique produces scratching or cracking on the surface and also it is an out-situ wet-process. In addition, surface smoothing of a target with a 3-dimensional structure and weak mechanical strength is difficult by mechanical polishing. Therefore, surface smoothing process in dry-condition with a high etching rate which causes less damage in the substrate is required.

The gas cluster ion beam process has superior characteristics of high-yield sputtering, surface smoothing effect and low damage. Thus, the gas cluster ion beam process is expected to be suitable for the surface smoothing of diamond films[138]. In this study, diamond thin films de-

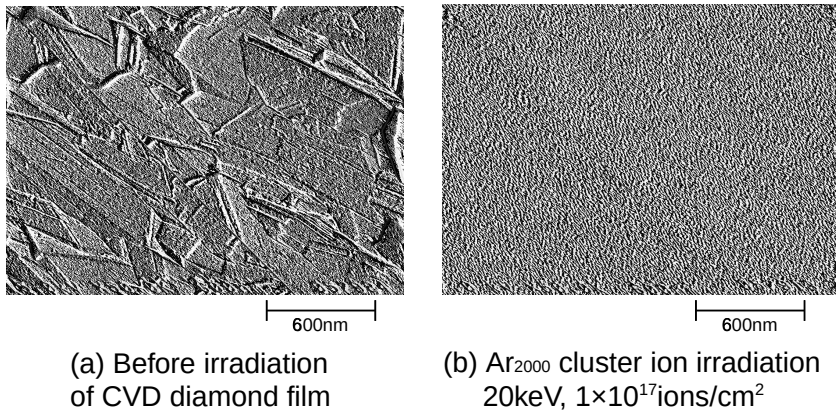

Figure 6.17: SEM images of a CVD diamond surface before and after Ar cluster ion irradiation. The acceleration energy and the ion dose were 20keV and 1×10^{17}ions/cm^2, respectively.

posited on Si substrate by a CVD technique were irradiated with both Ar and O_2 cluster ion beams. Subsequently, the surface roughnesses, the etching depth, transparency of the films and Raman spectra were measured. Finally, the application for the X-ray lithography membrane was discussed[139].

Surface Smoothing of CVD Diamond Films

The experimental procedure for surface smoothing with cluster ions is shown in Fig.6.16. Diamond films with 2μm thickness were deposited on a Si substrates by microwave plasma CVD using a CH_4 and H_2 gas mixture. After deposition, the diamond films were irradiated with cluster ion beams at normal incidence. To measure the optical transmittance of the diamond film, the Si substrate was etched from the reverse side with a HF and HNO_3 solvant. The optical transmittance of the diamond film was measured over the range of wavelength from 400 to 800nm.

Figure 6.17 shows Scanning Electron Microscopy (SEM) images of CVD diamond films before and after the 20keV Ar cluster ion irradiation. The average cluster size and ion dose were 2000atoms/cluster and 1×10^{17} ions/cm^2, respectively. Before irradiation, there were many pyramidal structures which are typical for polycrystalline diamond thin films. The surface roughness of the initial diamond surface was 40nm as measured by AFM. After irradiation, no pyramidal structures were observed

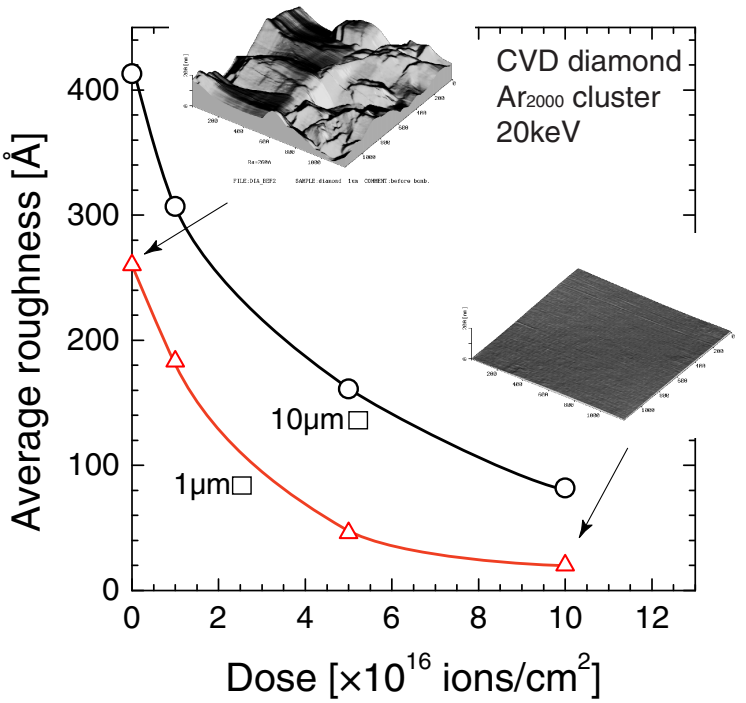

Figure 6.18: Ion dose dependence of average roughness of CVD diamond irradiated with Ar cluster ions. The acceleration energy was 20keV.

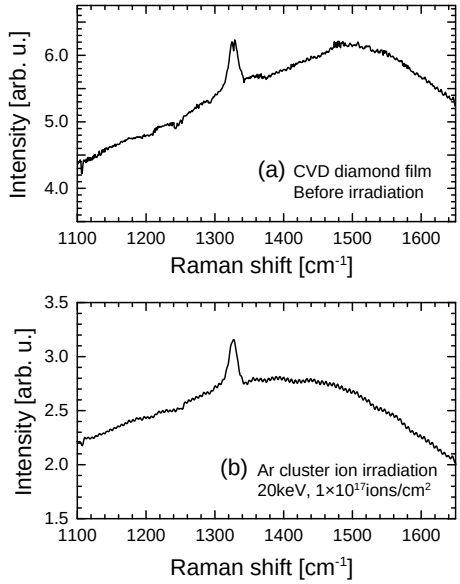

Figure 6.19: Raman spectra of CVD diamond films before and after 20keV Ar cluster ion irradiation.

and a very flat surface with average roughness of 8nm was obtained. In monomer ion irradiation, sputtering anisotropy on the facets of diamond was reported. The sputtering yield from a {100} surface is larger than that from a {111} surface[140], which causes a roughened diamond surface. In the case of cluster ions, there was no influence by the facets or crystallites, which was similar to situation for the Cu surface shown in Fig. 6.1.

Figure 6.18 shows the ion dose dependence of the average roughness of CVD diamond films irradiated with 20keV Ar cluster ions. In addition to the average roughness, AFM images of the diamond surface were included. The scanning areas of AFM were 1μm$\times 1\mu$m and 10μm$\times 10\mu$m. The cluster ion dose ranged up to 1×10^{17}ions/cm^2. The initial average roughness was 40nm (10μm square) and 26nm (1μm square), respectively. The average roughness decreased monotonically with the ion dose and the average roughnesses at an ion dose of 1×10^{17}ions/cm^2 were 8nm (10μm square) and 2nm (1μm square), respectively. These average roughnesses were comparable with the standard roughness of SiC and SiN_x, and they were sufficient for X-ray mask membrane application. The diamond film was etched to 1750Å in depth at a dose of 1×10^{17}ions/cm^2, which cor-

responded to a sputtering yield of 30 atoms/ion.

However, the surface smoothing with cluster ions caused a thin amorphous layer to be formed on the surface so that it was probable that the diamond surface was covered by amorphous carbon or graphite after cluster ion impact. To verify the surface states of the CVD diamond films, Raman spectra were measured. Fig.6.19 shows Raman spectra of CVD diamond films before and after a 20keV Ar cluster ion irradiation. The cluster ion dose and average cluster size were 1×10^{17}ions/cm^2 and 2000atoms/cluster, respectively. There was a sharp peak at 1332cm^{-1} in both spectra which was attributed to diamond. If there was a thick graphite layer on the surface, a broad peak around 1600cm^{-1} would appear, however, there was no marked difference between these spectra. Thus, the diamond surface remained the same after Ar cluster irradiation, and the amorphous layer on the top layer was believed to be very thin.

Reactive Etching of Diamond Films

Diamond undergoes reactive sputtering with oxygen, and reactive ion etching of diamond films with O_2 and H_2 plasmas has been reported[141]. Similarly, the sputtering yield of diamond films with O_2 cluster ions was chemically enhanced (380atoms/ion) and it became 12 times higher than with Ar cluster ions (30atoms/ion) at an acceleration energy of 20keV.

Although the sputtering yield was enhanced by the chemical reactions, the surface smoothing effect with oxygen cluster ion beams was less than with Ar cluster ion beams because of the isotropic distribution of sputtered atoms, in a similar way to how tungsten reacted with SF_6 cluster ions. When a CVD diamond film with an initial average roughness of 1000Å was irradiated with both Ar and oxygen cluster ion beams, the surface roughness of the diamond surface with Ar cluster ion beams decreased from 1000Å to 500Å. In contrast, the surface roughness of diamond films with oxygen cluster ions remained almost the same as the initial roughness.

To obtain a smooth surface, an adequate sputtered depth was required. However, the surface smoothing effect was weak if the chemical reaction was the dominant etching process. Therefore, Ar and O_2 mixed cluster ion beams were introduced for the effective surface smoothing of diamond films[142]. The formation of Ar and O_2 mixed cluster beam was discussed in chapter 3, and the ratio of chemical etching and physical

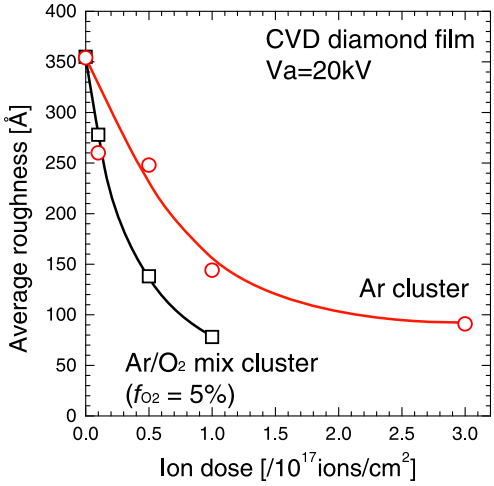

Figure 6.20: Ion dose dependence of the surface roughness irradiated with pure Ar cluter and Ar/O_2 mixed cluster ion beams. The mole fraction of O_2 was 5%.

sputtering can be controlled by the flow fraction of oxygen f_{O_2}.

Figure 6.20 shows the ion dose dependence of the surface roughness of diamond films irradiated with pure Ar and Ar/O_2 mixed cluster ion beams. The flow fraction of oxygen f_{O_2} was 5%. From Fig.6.20, the surface roughness with Ar/O_2 mixed cluster ions fell more rapidly than with pure Ar cluster ions. At an ion dose of 1×10^{17}ions/cm^2, the average roughness was about half that found with pure Ar cluster ions. Therefore, a smooth diamond surface can be obtained with lower ion doses by Ar/O_2 cluster ions. When the flow fraction f_{O_2} was increased, the surface smoothing effect became weaker. A small fraction of oxygen (<5%) was enough for the improvement of the smoothing efficiency.

The optical transmittance of the diamond films is important for the alignment procedure of the X-ray lithography patterns. Fig. 6.21 shows optical transmittance of the CVD diamond films irradiated with Ar/O_2 mixed cluster ion beams with a dose of 1×10^{17}ions/cm^2. The acceleration energy and the flow fraction of oxygen f_{O_2} were 20keV and 5%, respectively. The optical transmittance of diamond films with 2μm thickness, irradiated with mixed clusters was almost the same as the initial curve in the wavelength range from 400 to 800nm. If a graphite layer was formed on the diamond surface, the optical transmittance decreased and

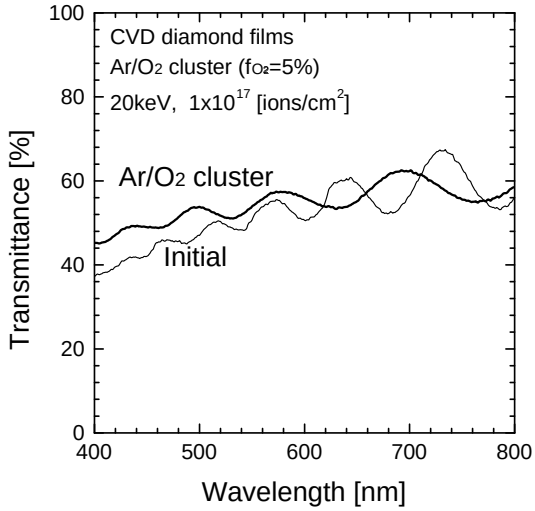

Figure 6.21: Optical transmittance of diamond film irradiated with Ar and O_2 cluster ions. The acceleration energy and ion dose were 20keV and 1×10^{17}ions/cm^2, respectively.

appearance of the sample became dark. From the appearance after back etching of the Si substrate, there was no change in color after irradiation. Since the sputtering yield of diamond with oxygen cluster ions was high, the damaged layer would be etched away even if it were formed on the surface. By using the Ar and O_2 mixed cluster ion beams, very flat diamond surfaces without graphite layers can be obtained with relatively low ion doses.

To demonstrate the capability of the cluster ion beam for the fabrication of the membrane for X-ray lithography mask, Ar and O_2 mixed cluster ion beams were irradiated over a large area (30mm×30mm). The flow fraction of O_2 was 5%. Fig. 6.22 showed a 3-inch wafer on which diamond thin film was deposited with 2μm thickness using plasma CVD. The acceleration energy and ion dose were 20keV and 4×10^{16}ions/cm^2, respectively. The whole area of 30×30mm was smoothed with the cluster ions. The cluster ion current was about 1μA and it took 40hours for the surface smoothing. Although this experimental irradiation time was not practical, we are now developing high current ($\sim$ 100μA) cluster ion beam equipment and it will eventually be possible to treat a 30mm×30mm area, which is the size required for an X-ray lithography mask, in approximately 20 minutes.

Figure 6.22: CVD diamond films of 30×30mm area irradiated with 20keV Ar/O_2 mixed cluster ions (f_{O_2}=5%). After irradiation, the Si substrate was etched from the reverse side.

From these results, the gas cluster ion beam technique can be expected to be very useful for surface smoothing of diamond films and for other applications in industrial fields.

6.3.2 SiC Surface Treatment

SiC is a promising material for power electronic devices. Several properties of SiC are compared with those of Si and GaAs in Table 6.1. Relative to Si, the energy gap of SiC is 3 times higher, breakdown voltage is 10 times as high and heat conductivity is 3 times higher. Therefore, these superior characteristics provide a potential solution for requirements such as power electronic devices, high stability against X-ray radiation or operation at high temperatures.

Table 6.1: Properties of SiC, Si and GaAs.

Property	SiC	Si	GaAs
Energy Bandgap (eV)	$3 \sim 3.3$	1.12	1.43
Electron mobility ($cm^2/V{\cdot}s$)	$450 \sim 1000$	1400	8500
Electron saturated velocity (cm/s)	$2 \sim 2.7 \times 10^7$	1.0×10^7	1.0×10^7
Breakdown electric field (V/cm)	$2.2 \sim 2.4 \times 10^6$	2.5×10^5	3×10^5
Heat conductivity (W/cm·°C)	$3\sim 3.8$	1.5	0.5
Melting point (°C)	~ 1800	1420	1238

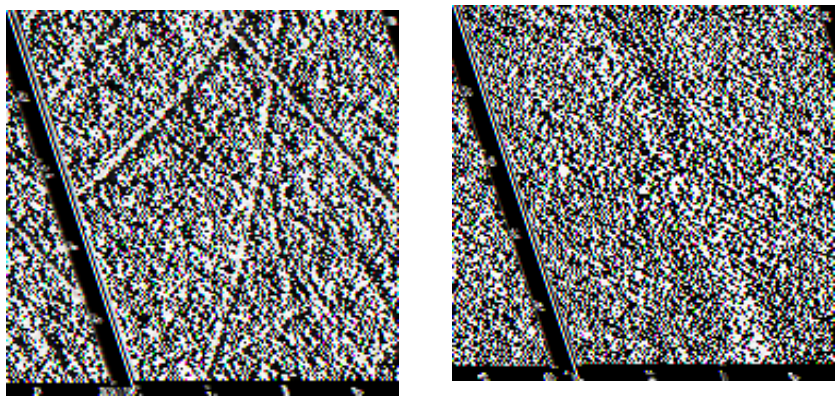

Figure 6.23: AFM images of 1inch 6H-SiC substrate (Cree Research, Inc.) irradiated with 20keV Ar cluster ions. The ion dose was 1×10^{17}ions/cm^2. (a) Before irradiation (Ra=7.5Å), (b) After Ar cluster ion irradiation (Ra=5.6Å)

Single crystals of SiC are grown by the sublimation of SiC powder. There are many polytypes in a SiC crystal such as 4H-SiC, 6H-SiC, 3C-SiC and so on, and the resulting crystal structure depends on the substrate and growth temperature. Today, 6H-SiC and 4H-SiC wafers, 2 inches in diameter, are commercially available. However, the SiC surfaces must be mechanically polished, and this induces the formation of scratches as shown in Fig. 6.23(a). In addition to the defects inside the SiC wafer, these defects on the surfaces make it difficult to fabricate semiconductor devices on presently available SiC wafers.

To remove the scratches produced by mechanical polishing on SiC surface, SiC wafers were irradiated with Ar cluster ion beams. Fig. 6.23 shows AFM images of a 1 inch 6H-SiC wafer (Cree Research, Inc.) (a) before irradiation and (b) after 20keV Ar cluster ion irradiation. The ion energy and dose were 20keV and 1×10^{17}ions/cm^2, respectively. The incident angle of the cluster ions was 0°. Before irradiation, there were many scratches on the surface caused by the mechanical polishing. The average roughness of the initial 6H-SiC substrate, measured with AFM, was 7.5Å. In contrast, no line or scratch was observed after Ar cluster ion irradiation and a very flat surface was obtained. The average roughness

of this surface was 5.6Å. As discussed in connection with the Monte-Carlo simulations, surface smoothing with cluster ions was more suitable for small size structures, which caused the removal of small scratches from the initial surface.

In addition to a monolithic SiC substrate, CVD SiC thin films were deposited on Si substrates and were irradiated with Ar cluster ion beams. The average cluster size and the acceleration energy were 2000atoms/cluster and 20keV, respectively. The initial roughness of the SiC thin films was 150Å, and the average roughness decreased with the ion dose in the same way as on Cu or diamond films. At an ion dose of 5×10^{16}ions/cm^2, the surface roughness was improved from 150Å to 12Å. Although SiC is a compound material, no influence of selective sputtering was observed with cluster ion beams. Similar to the diamond films, SiC is a very hard material and it is difficult to smoothen. With the use of the cluster ion beam technique, very hard materials such as SiC and diamond can be smoothed.

6.3.3 YBCO Superconducting Films

For the fabrication of High Temperature Superconductor (HTS) thin film devices, especially for multi-layer integrated circuits, a smooth HTS surface is crucial for the reliability and yield of the fabrication processes. In the formation of HTS integrated circuits, up to six levels of masking with epitaxial film growth are required. Therefore, the surface roughness of the first HTS layer is critical to the reproducibility and yield of the HTS junctions. In HTS thin film epitaxial depositions, the substrate is usually kept at a high temperature, resulting in the formation of islands or mesas which produce rough surfaces. Therefore, high temperature superconductor such as $Y_1Ba_2Cu_3O_7$ (YBCO) films were prepared and surface smoothing of these YBCO films by Ar cluster ion beams was performed[143].

YBCO thin films, 900nm thick, were produced by laser ablation on $LaAlO_3$. These YBCO films were irradiated with 20keV Ar cluster beams. The average cluster size was 2000 atoms/cluster. Fig. 6.24 shows AFM images of YBCO films before and after irradiation. Before irradiation (a), islands or mesas were formed on the substrate due to the variation of growth speed along the various crystalline directions[143]. Additional debris and impurities presented during the deposition process roughened the surface. After cluster ion irradiation to a dose of

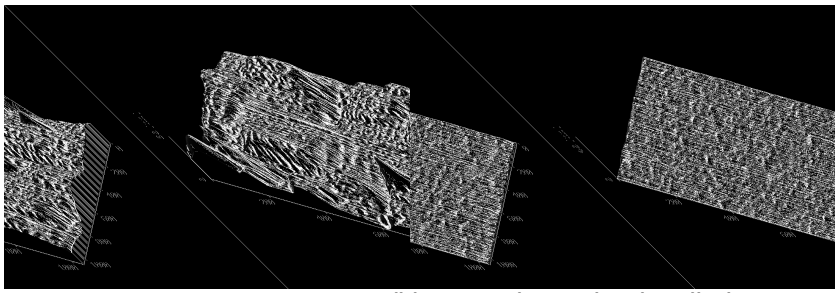

Figure 6.24: AFM images of YBCO thin films irradiated with Ar cluster ions. The acceleration energy and ion dose were 20keV and 2×10^{16}ions/cm^2, respectively.

2×10^{16}ions/cm^2, the YBCO surface was smoothed significantly. The sputtered depth of YBCO film was 220nm. The small hillocks were totally removed and the average roughness after cluster irradiation was 12Å in a 1μm$\times1\mu$m area. Although the $Y_1Ba_2Cu_3O_7$ involves 13 atoms per unit cell of four different elements, and is very complicated as compared to the simple mono-element and binary compounds, an Ar cluster beam could smooth the YBCO surface without inducing selective sputtering.

For the fabrication of the HTS multilayer devices, epitaxial growth on the surface treated with a cluster ion beam is necessary. To verify the capability of the epitaxial growth, after annealing, a second YBCO layer was deposited on the surface by laser ablation and homo-epitaxial YBCO films were obtained. The crystalline re-growth was verified by the RBS channeling method[143)]. Although the newly deposited film was single crystal, the surface was rough, as expected. If it is necessary to fabricate structures on top of this new layer, surface smoothing with a cluster beam will be required again for the second layer. Thus, smoothed multilayer systems can be constructed. This process is expected to be important for improving the yield and reliability of HTS junction IC devices, as well as for passive stripline delay lines, antennas and filters that will use HTS film.

6.4 Summary

In this chapter, the surface smoothing effects of cluster ion beams were studied. The physically sputtered atoms with cluster ion impact showed the lateral sputtering effects. These physical sputtering phenomena were modeled and a smoothing mechanism was discussed. Finally, several applications of the surface smoothing with cluster ions were proposed. The following are summaries of this chapter:

1. The surface smoothing effect with cluster ions was much higher than with monomer ions at the same ion dose, and it was not influenced by grains or facets present before treatment. The surface roughness decreased monotonically with ion dose at normal incidence, and there was no roughening mechanism.

2. The surface roughness increased with the incident angle. The surface smoothing with cluster ions was most effective at normal incidence. When the incident angle was over 45°, surface roughening appeared, which were caused by ripple formation whose wave vector was parallel to the trajectory.

3. When chemical reactions were introduced by reactive cluster ion impacts, the surface smoothing effect was not significant. This corresponded to the isotropic angular distribution of sputtered atoms. The anisotropic angular distribution called 'lateral sputtering' is responsible for surface smoothing with cluster ions.

4. When a cluster ion impacts upon a slope, atoms ejected from the crater move downward and the valley is filled by the dislocated atoms. The surface is initially made smooth by this effect. The dislocated atoms filling the valley are eventually removed with increasing dose, and finally, very smooth surfaces with a thin amorphous layer can be obtained.

5. Structures with high spatial frequencies are preferentially smoothed at first but large patterns need high fluences to be smoothed. The saturation value of the surface roughness at high fluences decreases with a reduction of the acceleration energy.

6. CVD diamond films were smoothed by Ar cluster ion irradiation, and the surface roughness of 2nm, which was sufficient for application of a membrane as an X-ray lithography mask, was obtained.

The surface roughness of diamond films improved at lower ion dose by use of Ar/O_2 mixed cluster ion beams. Diamond films of large area could be smoothed with cluster ion beams, and cluster beam techniques can be applicable for the fabrication of X-ray lithography membranes.

7. Compound materials such as SiC and YBCO superconducting films were smoothed without roughening due to selective sputtering.

Chapter 7

Conclusions

In this study, we have presented the gas cluster ion beam as a 'nano-processing' tool. Cluster ions deposit their kinetic energy on the surface of a target, which causes multiple collisions and non-linear effects between the cluster and target atoms. However, the impact processes of cluster ions remain unknown and it is important for practical applications to clarify the intrinsic phenomena caused by cluster ion impact. To explore these non-linear effects associated with cluster ions, fundamental phenomena with cluster ions such as sputtering, surface smoothing and etching have been studied. In addition, the properties of cluster beams such as their formation, ionization, mass distribution and detection have been investigated. The following are summaries of this study.

In chapter 2, theoretical descriptions of cluster beam formation via supersonic expansion were discussed. The high current gas cluster ion beam equipment was developed, and cluster ion current densities of several μA/cm^2 were obtained. These will be sufficient for processing in the practical applications.

In chapter 3, gas cluster beam formation and properties of cluster beams were studied with a time of flight mass spectrometer having high mass resolution ($m/\Delta m$=1500). Since a large cluster ion had huge mass and its velocity was much lower than that of a monomer ion at the same energy, the secondary electron yield decreased. As a result, the detection probability of a large cluster ion using a micro channel plate (MCP) became low. A high acceleration voltage which gave ion velocity of over 2000m/s was necessary in order to detect large cluster ions with an MCP.

Both cluster beam intensity and the average cluster size increased with the source gas pressure, and neutral cluster formation started from

1500Torr. Neutral clusters grew not only by monomer attachment but also by cluster-cluster aggregations.

With increasing cluster size, both collisional and ionization cross-sections became large, which resulted in a short mean free path and high ionization efficiency by electron bombardment. Although a cluster ion collided frequently with residual gas atoms, the impact energy with the residual gas was compensated by the cohesive force of the cluster. The ionization efficiency of a cluster with size n atoms increased in proportion to $n^{\frac{2}{3}}$, such that ionization efficiency of clusters with 2000 atoms reached 50% when the electron emission current was 260mA. Since clusters were ionized preferentially, the cluster ion current saturated with increasing the electron emission current due to the lack of neutral clusters. An intense neutral beam is required to obtain a high cluster ion current.

In addition to the inert gas clusters, reactive and complex gas clusters were generated by co-mixing of He or Ar gases with the reactive gas. In the case of O_2 mixing with Ar, not only Ar and O_2 clusters, but also $Ar_m(O_2)_n$ complex clusters were generated. The ratio of composition of the complex cluster could be changed by the flow ratio of Ar to O_2. With increasing fraction of O_2, the mole fraction n of O_2 in the complex cluster $(Ar_m(O_2)_n)$ also increased.

Since the ionization of neutral clusters was carried out by electron bombardment, a large fraction of multiply charged cluster ions was observed when the ionization energy of the electrons exceeded 40eV. The multiply charged large cluster ions were more stable than small cluster ions because the Coulomb repulsion force between the charges was compensated by the cohesive force associated with large clusters.

In chapter 4, sputtering phenomena by Ar cluster ion beams were discussed in terms of the sputtering yield, a single track by a cluster impact and angular distributions of the sputtered atoms. A dense energy deposition in a local area caused multiple collisions between target and cluster atoms. As a result, non-linear effects, such as, crater formation, shock-wave formation and high sputtering yield, were observed.

The damage depth with cluster ions was much shallower than that with monomer ions with the same total acceleration energy. Since the nuclear stopping power of a cluster is high, the kinetic energy of the cluster ion was deposited on the surface region of the target. This resulted in enhancement of both the sputtering yields for various materials and the secondary ion yields.

Sputtering yields with Ar cluster ions increased linearly with accel-

eration energy, and there was a threshold energy for sputtering at the acceleration energy of 6keV. From a microscopic point of view with STM observations, the crater diameter increased with the cube root of the acceleration voltage in the range from 20keV to 150keV. Since the shape of the damaged area by cluster impact was hemispherical in this range of energy, the volume of the damaged area increased in proportion to the acceleration energy. Also, the sputtering yield with cluster ions decreased in proportion to $\cos\theta$ with increasing incident angle θ.

As to the angular distribution of sputtered atoms with cluster ions, it showed an under-cosine distribution at normal incidence. Although the distribution resembled that found with low-energy monomer ions, laterally distributed atoms originated from the edges of the impact craters. This indicated that the sputtering process with cluster ions was completely different from that of low-energy monomer ions. The angular distribution changed from an under-cosine distribution to a uni-directional one at a slightly off-normal incidence. This showed that the angular distribution of sputtered atoms was very sensitive to the incident angle near 0°.

In chapter 5, properties of reactive cluster ions and their interactions with the target atoms were studied. Subsequently, applications for the fabrication of fine structures were discussed. When an SF_6 cluster ion impacted upon a target, dissociation of SF_6 molecules occurred in addition to the fragmentation of the SF_6 cluster ions. As a consequence, fluorine atoms reacted with Si and W atoms, and volatile materials such as SiF_4 and WF_6 were generated. The sputtering yields of Si and W were chemically enhanced by SF_6 cluster ions, and these volatile materials left the surface isotropically.

The etching ratio of Si to SiO_2 increased with decreasing energy per atom in a cluster. At a total acceleration energy below 10keV, chemical etching was the dominant process. A Si trench with hole 0.5μm in diameter was etched anisotropically with a reactive cluster ion beam, and no charging up or erosion under the mask were observed. Many of the problems which remaining in plasma source etching can be resolved with reactive cluster ion beams.

In chapter 6, surface smoothing effects with cluster ions were discussed. Very smooth surfaces with average roughnesses below a few nanometers could be obtained with cluster ion irradiation at normal incidence. There was no roughening mechanism with increasing ion dose. However, the surfaces were roughened at oblique incidence and ripple

formation parallel to the incident direction was observed.

From comparisons between the surface smoothing effects of physical and reactive sputtering, respectively, it has been demonstrated that lateral sputtering is significant for the surface smoothing with cluster ions. When the chemical reaction was dominant and the angular distribution of sputtered atoms was isotropic, no marked surface smoothing effects were observed.

Sputtering phenomena with cluster ions were modeled and a Monte-Carlo simulation was carried out. When a cluster impacted upon a slope, large numbers of ejected atoms moved down the slope, and consequently, the valley became filled with dislocated atoms. Once the surface became flat, there was no subsequent roughening mechanism. Since the angular distribution changed even at a small incident angles, a cluster was very sensitive to the angle of the slope. Thus, a gentle slope was smoothed with cluster ions so that the average roughness was improved.

As practical applications of the surface smoothing with cluster ions, surface smoothing of CVD diamond films, SiC and YBCO films, where smooth surfaces are difficult to attain, was demonstrated with gas cluster ion beams. CVD diamond films, with 30mm×30mm in size, were successfully smoothed with cluster ions which can be used for the X-ray lithography masks. Although YBCO film contains many elements, there was no selective sputtering effect with cluster ion sputtering.

From these results, it is clear that the gas cluster ion beam technique is to be very useful for nano-processing. In addition to the applications demonstrated in chapter 6, there are many industrial fields in which the gas cluster ion beam processes can be applied. In this study, the properties of the cluster beam and the physical and chemical phenomena in a cluster ion impact were clarified. These results will contribute to understanding and to development of the cluster beam processes.

References

[1] L.T.Canham, Appl. Phys. Lett., **57**, 1046 (1990).

[2] H.W.Kroto, J.R.Heath, S.C.O'Brien and R.E.Smally, Nature, **318**, 162 (1985).

[3] W.Kratschmer, L.D.Lamb, K.Fostiropoulos and D.R.Huffman, Nature, **347**, 354 (1990).

[4] S.Iijima, Nature, **354**, 56 (1991).

[5] D.Ugarte, Nature, **359**, 707 (1992).

[6] A.F.Hebard, M.J.Rosseinsky, R.C.Haddon, D.W.Murphy, S.H.Glarum, T.T.M.Palstra, A.P.Ramirez and A.R.Kortan, Nature, **350**, 600 (1991).

[7] R.Beuhler and L.Friedman, Chem. Rev., **86**, 521 (1986).

[8] G.Galileo, *Unterrendungen und Demonstrationen Uber Zwei neue Wissenszweige*, (1638).

[9] I.Newton, *Principia*, (1686).

[10] T.Geherels, *'Collisions with Comets and Asteroids'*, Scientific American, March (1996).

[11] N.Rostocker, Meteoritics, **1**, 1 (1953).

[12] K.L.Merkle and W.Jäger, Philos. Mag. A, **44**, 741 (1981)

[13] M.W.Matthew, R.J.Beuhler, M.Ledbetter and L.Friedman, Nucl. Instr and Meth. B, **14**, 448 (1986).

[14] D.Takeuchi, *Non-linear Processes in Cluster Ion Implantation on Solid Surfaces*, Ph. D thesis, Kyoto University (1997).

[15] C.L.Cleveland and U.Landman, Science, **257**, 355 (1992).

[16] I.Yamada, Proc. 14th Symp. on Ion Sources and Ion Assisted Technology, Tokyo, 227 (1991).

[17] I.Yamada, Radiation Effects and defects in Solids, **124**, 69 (1992).

[18] I.Yamada and G.H.Takaoka, Jpn. J. Appl. Phys., **32**, 2121 (1993).

[19] I.Yamada, J.Matsuo, E.C.Jones, D.Takeuchi, T.Aoki, K.Goto and T.Sugii, Proc. of Mat. Res. Soc. Symp., **438**, 343 (1997).

[20] I.Yamada and J.Matsuo, Proc. of Mat. Res. Soc. Symp., **396**, 149 (1996).

[21] I.Yamada, J.Matsuo, Z.Insepov, D.Takeuchi, M.Akizuki and N.Toyoda, J. Vac. Sci. Technol. A, **14**, 781 (1996).

[22] M.Akizuki, J.Matsuo, M.Harada, S.Ogasawara, A.Doi, K.Yoneda, T.Yamaguchi, G.H.Takaoka, C.E.Ascheron and I.Yamada, Nucl. Instr. and Meth. B, **99**, 225 (1995).

[23] K.Goto, J.Matsuo, Y.Tada, T.Tanaka, Y.Momiyama, T.Sugii and I.Yamda, IEDM Tech. Dig., 471 (1997).

[24] Z.Insepov and I.Yamada, Nucl. Instr. and Meth. B, **99**, 248 (1995).

[25] T.G.Dietz, M.A.Duncan, D.E.Powers and R.E.Smalley, J. Chem. Phys., **74**, 6511 (1981).

[26] J.F.Frichtenicht, Rev. Sci. Instrum., **45**, 51 (1974).

[27] E.S.Marmar, J.L.Cecchi and S.A.Cohen, Rev. Sci. Instrum., **46**, 1149 (1975).

[28] H.Schaber and T.P.Martin, Surf. Sci., **156**, 64 (1985).

[29] E.W.Becker, K.Bier and W.Henkes, Z.Phys., **146**, 333 (1956).

[30] O.Hagena, Surf. Sci., **106**, 101 (1981).

[31] L.D.Landau and E.M.Lifshitz, *Fluid Mechanics,* Pergamon Press, (1959).

[32] H.Ashkenas and F.S.Sherman, *Rarefied Gasdynamics,* **II**, 1181 (1979).

[33] H.Haberland, *Clusters of Atoms and Molecules,* Springer-Verlag, Berlin (1994).

[34] O.F.Hagena and W.Obert, J. Chem. Phys., **56**, 1793 (1972).

[35] E.Ashkenas and F.S.Sherman, *Rare Gas Dynamics 2*, ed. J.H.de Leeuw, Academic Press (1965).

[36] J.Matsuo, H.Abe, G.H.Takaoka and I.Yamada, Nucl. Instr. and Meth. B, **99**, 244 (1995).

[37] K.Walter, U.Böesl and E.Schlag, Int. J. Mass Spectrom. Ion. Proc., **71**, 255 (1986).

[38] W.Paul and H.Steinwedel, Naturforsch, **8A**, 448 (1953).

[39] J.F.O'Hanlon, *A User's Guide to Vacuum Technology*, John Wiley & Sons Inc. (1980).

[40] W.C.Wiley and I.H.McLaren, Rev. Sci. Instrum., **26**, 1150 (1955).

[41] V.I.Karataev, B.A.Mamyrin and D.V.Shmikk, Soviet Phys. Tech. Phys., **16**, 1177 (1972).

[42] R.B.Opscal, K.G.Owens and J.P.Reilly, Anal. Chem., **57**, 1884 (1985).

[43] D.M.Lubman and R.M.Jordan, Rev. Sci. Instrum., **56**, 373 (1985).

[44] K.Sattler, J.Mühlbach, E.Rechnagel and A.Reyes-Flotte, J. Phys. E, **13**, 673 (1980).

[45] U.Böesl, H.J.Neusser, R.Weinkauf and E.W.Schlag, J. Phys. Chem., **86**, 4857 (1982).

[46] T.P.Martin and H.Schaber, Rev. Sci. Instrum., **60**, 347 (1989).

[47] C.M.Lederer and V.S.Shireley, *Table of Isotopes 7th ed.*, John Wiley & Sons. Inc., New York (1978).

[48] E.V.Alonso, R.A.Baragiola, J.Ferrón, M.M.Jakas and A.Oliva-Florio, Phys. Rev. Rev. B, **22**, 22 (1980).

[49] N.Toyoda, M.Saitoh, N.Hagiwara, J.Matsuo and I.Yamada, Proceedings of the 12th international conference on Ion Implantation Technology, to be published.

[50] U.Zimmerman, N.Malinowski, U.Naher, S.Frank and T.P.Martin, Z. Phys. D, **31**, 85 (1994).

[51] F.Thum and W.O.Hofer, Surf. Sci., **90**, 331 (1979).

[52] R.F.K.Herzog, W.P.Poschenrieder and J.Franzen, Radiat. Effects, **18**, 199 (1973).

[53] O.Echt, K.Sattler and E.Rechnagel, Phys. Rev. Lett., **47**, 1121 (1981).

[54] O.Echt, O.Kandler, T.Leisner, W.Miehle and E.Rechnagel, **86**, 2411 (1990).

[55] G.Gantefor, G.Broker, E.Holub-Krappe and A.Ding, J. Chem. Phys., **91**, 7972 (1989).

[56] M.Akizuki, J.Matsuo, M.Harada, S.Ogasawara, A.Doi and I.Yamada, Mater. Sci. Eng. A, **217/218**, 78 (1995).

[57] W.Qin, R.P.Howson, M.Akizuki, J.Matsuo, G.H.Takaoka and I.Yamada, Mater. Chem. and Phys., **54**, 258 (1998).

[58] E.Valente and L.Bartell, J. Chem. Phys., **79**, 2683 (1983).

[59] D.Margreiter, G.Walder, Z.Herman and T.D.Märk, Chem. Phys. Lett., **167**, 341 (1990).

[60] A.Nakajima, K.Hoshino, T.Naganuma, Y.Sone and K.Kaya, J. Chme. Phys., **95**, 7061 (1991).

[61] O.F.Hagena, *Molecular Beams and Low Density Gas Dynamics,* ed. P.E.Wegener, Marcel Dekker Inc., New York (1974).

[62] N.E.Levinger, D.Ray, M.L.Alexander and W.C.Lineberger, J. Chem. Phys., **89**, 5654 (1988).

[63] T.Nagata, J.Hirokawa and T.Kondow, Chem. Phys. Lett., **89**, 176 (1991).

[64] K.Hiraoka, J. Chem. Phys., **89**, 3190 (1988).

[65] M.M.Kappes, P.Radi, M.Schar, C.Yeretzion and E.Schumacher, Z. Phys. D, **3**, 115 (1986).

[66] K.Sattler, J.Mühlbach, O.Echt, P.Pfau and E.Rechnagel, Phys. Rev. Lett., **47**, 160 (1981).

[67] J.G.Gay and B.J.Berne, Phys. Rev. Lett., **49**, 194 (1982).

[68] P.Scheier, A.Stamatovic and T.D.Märk, Chem. Phys. Lett., **144**, 119 (1988).

[69] D.Kreisle, O.Echt, M.Knapp, E.Rechnagel, K.Leiter, T.D.Märk, J.J.Saenz, and J.M.Soler, Phys. Rev. Lett., **56**, 1551 (1986).

[70] P.Scheier and T.D.Märk, J. Chem. Phys., **86**, 3056 (1987).

[71] M.Lezius, P.Scheier, A.Stamatovic and T.D.Mark, J. Chem. Phys., **91**, 3240 (1989).

[72] P.Scheier, G.Walder, A.Stamatovic and T.D.Mark, J. Chem. Phys., **90**, 4091 (1989).

[73] P.Scheier, A.Stamatovic and T.D.Mark, J. Chem. Phys., **88**, 4289 (1988).

[74] C.Brechignac, M.Broyer, P.Cahuzac, G.Delacretaz, P.Labastie and L.Wöste, Chem. Phys. Lett., **133**, 45 (1987).

[75] P.Sigmund, Phys. Rev., **184**, 383 (1969).

[76] P.Sigmund, Nucl. Instr. and Meht. B, **27**, 1 (1987).

[77] H.H.Anderson and H.L.Bay, J. Appl. Phys., **46**, 2416 (1975).

[78] J.Matsuo, N.Toyoda, M.Akizuki, I.Yamada, Nucl. Instr. and Meth. B, **121**, 459 (1997).

[79] K.Kanaya, K.Houjou, K.Koga and F.Toki, Jpn. J. Appl. Phys., **12**, 1297 (1973).

[80] N.Laegreid and G.K.Wehner, J. Appl. Phys., **32**, 365 (1961).

[81] R.C.Bradley, Phys. Rev., **93**, 719 (1954).

[82] D.A.Thompson and S.S.Johar, Appl. Phys. Lett., **34**, 342 (1975).

[83] D.J.Oostra, R.P. van Ingen, A.Haring, A.E. de Vries and F.W.Saris, Phys. Rev. Lett., **61**, 1392 (1988).

[84] J.P.Biersack and L.G.Haggmark, Nucl. Instr. and Meth., **174**, 257 (1980).

[85] Z.Insepov and I.Yamada, Nucl. Instr. and Meth. B, **121**, 498 (1995).

[86] H.H.Andersen and H.L.Bay, *Sputtering by Particle Bombardment I*, ed. R.Behrisch, Springer-Verlag, Berlin (1981).

[87] N.Matsunami, Y.Yamamura, Y.Ichikawa, N.Itoh, Y.Kazumata, S.Miyagawa, K.Morita, R.Shimizu and H.Tawara, Atomic Data and Nuclear Data Tables, **31**, 1 (1984).

[88] D.Takeuchi, K.Fukushima, J.Matsuo and I.Yamada, Nucl. Instr. and Meth. B, **121**, 493 (1997).

[89] V.I.Shulga and P.Sigmund, Nucl. Instr. and Meth. B, **47**, 236 (1990).

[90] T.Aoki, T.Seki, J.Matsuo, Z.Insepov and I.Yamada, Mat. Chem. and Phys., **54**, 139 (1998).

[91] G.K.Wehner, J. Appl. Phys, **30**, 1762 (1959).

[92] F.R.Vossen, J. Vac. Sci. Technol., **1**, 875 (1974).

[93] N.Toyoda, H.Kitani, N.Hagiwara, T.Aoki, J.Matsuo and I.Yamada, Mat. Chem. and Phys., **54**, 262 (1998).

[94] W.Zhenxia, L.Wenyun, W.Chuanshan and W.Wenmin, Vacuum, **47**, 1465 (1996).

[95] Z.Insepov, M.Sosnowski and I.Yamada, Trans. Matter. Res. Soc. Jpn., **17**, 111 (1994).

[96] T.Aoki, J.Matsuo, Z.Insepov and I.Yamada, Nucl. Instr. and Meth. B, **121**, 49 (1997).

[97] I.I.Glass, *Shock Waves & Man*, tr. K.Takayama, Maruzen, Tokyo (1987).

[98] *Handbook of Chemistry and Physics*, ed. R.C.Weast, CRC Press, Inc., Florida (1986).

[99] S.R.Coon, W.F.Calaway and M.J.Pellin, Surf. Sci., **298**, 161 (1993).

[100] H.Dammak, A.Dunlop, D.Lesueur, A.Brunelle, S.Della-Negra and Y. Le Beyec, Phys. Rev. Lett., **74**, 1135 (1995).

[101] U.Gerlach-Meyer, J.W.Coburn and E.Kay, Surf. Sci., **103**, 177 (1981).

[102] G.Carter and J.S.Colligon, *Ion Bombardment of Solids*, Heineman Educational Book Ltd., London (1988).

[103] D.J.Oostra, A.Haring, A.E. de Vries, F.H.M.Sanders and G.N.A. van Veen, Nucl. Instr. and Meth. B, **13**, 556 (1986).

[104] B.Chapman, *Grow Discharge Processes, Sputtering and Plasma Etching*, John Wiley and Sons, New York (1988).

[105] J.L.Vossen, J. Appl. Phys., **47**, 544 (1976).

[106] N.Toyoda, H.Kitani, N.Hagiwara, J.Matsuo and I.Yamada, Mat. Chem. and Phys., **54**, 106 (1998).

[107] N.Toyoda, H.Kitani, J.Matsuo and I.Yamada, Nucl. Instr. and Meth. B, **121**, 484 (1997).

[108] H.Gokan, M.Itoh and S.Esho, J. Vac. Sci. and Technol. B, **2**, 3 (1984).

[109] J.W.Coburn and H.F.Winters, Nucl. Instr. and Meth. B, **27**, 243 (1987).

[110] D.R.Wood and D.V.Morgan, J. Electrochem. Soc., **122**, 773 (1975).

[111] Z.Liau and T.T.Sheng, Appl. Phys. Lett., **32**, 716 (1978).

[112] S.Rusponi, C.Boragno and U.Valbusa, Phys. Rev. Lett., **78**, 2795 (1997).

[113] E.Chason, T.M.Mayer, B.K.Kellerman, D.T.McIlroy and A.J.Howard, Phys. Rev. Lett., **72**, 3040 (1994).

[114] G.Carter and V.Vishnyakov, Phys. Rev. B, **54**, 17647 (1996).

[115] G.Carter, V.Vishnyakov, Yu.V.Martynenko and M.J.Nobes, J. Appl. Phys. **78**, 3559 (1995).

[116] E-H. Cirlin, J.J.Vajo, R.E.Doty and T.C.Hasenberg, J. Vac. Technol. A, **9**, 1395 (1991).

[117] S.W.MacLaren, J.E.Baker, N.L.Finnergan and C.M.Loxton, J. Vac. Technol. A, **10**, 468 (1992).

[118] T.M.Mayer, E.Chason and A.J.Haward, J. Appl. Phys., **76**, 1633 (1994).

[119] K.Oyoshi, S.Hishita, K.Wada, S.Suehara and T.Aizawa, Appl. Surf. Sci., **100**, 374 (1996).

[120] F.A.Stevie, P.M.Kahara, D.S.Simons and P.Chi, J.Vac.Technol. A, **6**, 76 (1988).

[121] Eun-Hee Cirlin, Thin Solid Films, **220**, 197 (1992).

[122] R.M.Bradley, Eun-Hee Cirlin, Appl. Phys. Lett., **68**, 3722 (1996).

[123] T.A.Winningham, Z.Zou, K.Douglas and N.A.Clark, J. Vac. Technol. A, **16**, 1178 (1998).

[124] R.Bradley and J.Harper, J. Vac. Sci. Technol. A, **6**, 2390 (1988).

[125] G.Carter and V.Vishnyakov, Phys. Rev. Lett., **54**, 17647 (1996).

[126] R.M.Bradley, Phys. Rev. Lett., **54**, 6149 (1996).

[127] G.Carter, Appl. Phys. Lett., **71**, 3066 (1997).

[128] H.Kitani, N.Toyoda, J.Matsuo and I.Yamada, Nucl. Instr. and Meth. B, **121**, 489 (1997).

[129] R.Cuerno, H.A.Makse, S.Tomassone, S.T.Harrington and H.E.Stanley, Phys. Rev. Lett., **75**, 4464 (1995).

[130] S.Matsuomoto, Y.Sato, M.Kamo and N.Setaka, Jpn. J. Appl. Phys., **21**, L183 (1982).

[131] M.F.Ravet and F.Rousseaux, Diamond and Relat. Mater., **5**, 812 (1996).

[132] L.Shäfer, A.Bluhm, C.P.Klages, B.Löchel, L.M.Buchmann and H.L.Huber, Diamond and Relat. Mater., **2**, 1191 (1993).

[133] H.Tokura, C.F.Yang and M.Yoshikawa, Thin Solid Film, **212**, 49 (1992).

[134] S.Ilias, G.Sené, P.Möller, V.Stambouli, J.Pascallon, D.Boucheir, A.Gicquel, A.Tardieu, E.Anger and M.F.Ravet, Diamond and Relat. Mater., **5**, 835 (1996).

[135] S.Kiyohara, I.Miyamoto, T.Masaki and S.Honda, Nucl. Instr. and Meth. B, **121**, 191 (1997).

[136] H.Buchkremer-Hermanns, C.Long and H.Weiss, Diamond and Relat. Mater., **5**, 845 (1996).

[137] R.E.Rawles, S.F.Komarov, R.Gat, W.G.Morris, J.B.Hudson and M.P.D'Evelyn, Diamond and Relat. Mater., **6**, 791 (1997).

[138] A.Yoshida, M.Deguchi, M.Kitabatake, T.Hirao, J.Matsuo, N. Toyoda and I.Yamada, Nucl. Instr. and Meth. B, **112**, 248 (1996).

[139] A.Nishiyama, M.Adachi, N.Toyoda, N.Hagiwara, J.Matsuo and I.Yamada, Proceeding of the 15th International Conference on Application of Accelerators in Research and Industry, November 1998, Denton TX, to be published.

[140] C.L.Cheng, H.C.Chang, J.C.Lin and K.J.Song, Phys. Rev. Lett., **78**, 3713 (1997).

[141] G.S.Sandhu and W.K.Chu, Appl. Phys. Lett., **55**, 437 (1989).

[142] N.Toyoda, N.Hagiwara, J.Matsuo and I.Yamada, Nucl. Instr. and Meth. B, **148**, 639 (1999).

[143] W.K.Chu, Y.P.Li, J.R.Liu, J.Z.Wu, S.N.Tidrow, J.Matsuo, N.Toyoda and I.Yamada, Appl. Phys. Lett., **72**, 246 (1998).

List of Figures

List of Tables

List of Publications

Full length papers

1. N.Toyoda, H. Kitani, J.Matsuo and I.Yamada,
"Reactive Sputtering by SF_6 Cluster Ion Beams"
Nucl. Instr. and Meth. in Phys. Res. B, **121**, 484 (1997).

2. N.Toyoda, H.Kitani, N.Hagiwara, J.Matsuo and I.Yamada,
"Surface smoothing effects with reactive cluster ion beams",
Mat. Chem. and Phys., **54**, 106 (1998).

3. N.Toyoda, H.Kitani, N.Hagiwara, T.Aoki, J.Matsuo and I.Yamada,
"Angular distributions of the particles sputtered with Ar cluster ions",
Mat. Chem. and Phys., **54**, 262 (1998).

4. N.Toyoda, N.Hagiwara, J.Matsuo and I.Yamada, "Surface treatment of diamond films with Ar and O_2 cluster ion beams", Nucl. Instr. and Meth. B, **148**, 639 (1999).

5. H.Kitani, N.Toyoda, J.Matsuo and I.Yamada, "Incident angle dependence of the sputtering effect of Ar cluster ion bombardment", Nucl. Instr. and Meth. in Phys. Res. B, **121**, 489 (1997).

6. I.Yamada, J.Matsuo, Z.Insepov, D.Takeuchi, M.Akizuki and N.Toyoda, "Surface processing by gas cluster ion beams at the atomic(molecular) level", J. Vac. Sci. Technol. A, **14**, 781 (1996).

7. J.Matsuo, N.Toyoda and I.Yamada, "Nanofabrication technology by gas cluster ion beams", J. Vac. Sci. Technol. B, **14**, 3951 (1996).

8. A.Yoshida, M.Deguchi, M.Kitabatake, T.Hirao, J.Matsuo, N.Toyoda and I.Yamada, "Atomic Level Smoothing of CVD Diamond Films by Gas Cluster Ion Beams Etching", Nucl. Instr. and Meth. in Phys. Res. B, **112**, 248 (1996).

9. J.Matsuo, N.Toyoda, M.Akizuki and I.Yamada, "Sputtering of elemental metals by Ar cluster ions", Nucl. Instr. and Meth. in Phys. Res. B, **121**, 459 (1997).

10. I. Yamada, J. Matsuo, N.Toyoda, T. Aoki and Z. Insepov, "A New Sputter Etching Technology by Gas-Cluster Ion Beam", J. Surf. Sci. Soc. of Japan, **18**, 743 (1997). [in Japanese]

11. W.K. Chu, Y.P. Li, J.R. Liu, J.Z. Wu, S.C. Tidrow, N.Toyoda, J. Matsuo and I. Yamada, "Smoothing of $YBa_2Cu_3O_{7-\delta}$ films by ion cluster beam bombardment, Appl. Phys. Lett., **72**, 246 (1998).

12. I. Yamada, J. Matsuo, N.Toyoda, T. Aoki, E. C. Jones and Z. Insepov, "Non-linear processes in the gas cluster ion beam modification of solid surfaces", Mater. Sci. Eng. A, **253**, 249 (1998).

13. J. Matsuo, E. Minami, M. Saito, N.Toyoda, H. Katsumata and I. Yamada, "High Intensity Oxygen Cluster Ion Beam Generation and its Application to Cluster Ion Assisted Deposition", The European Phys. J. D to be published.

Proceedings

1. N.Toyoda, T. Kaneko, T. Yoshizawa, M. Akizuki, J. Matsuo, G. H. Takaoka and I. Yamada, "Development of semiconductor surface treatment technology by gas cluster ion beam", Papers of the Institute of Electronics, Information and Communication Engineers of Japan, Vol. 94, No. 367, pp.113 (1994) [in Japanese].

2. D. Takeuchi, A. Kitai, N.Toyoda, J. Matsuo, G. H. Takaoka and I. Yamada, "Shallow implantation formed by 200kV Ar gas cluster ion beams", Papers of the Institute of Electronics, Information and Communication Engineers of Japan, Vol. 94, No. 366, pp.97 (1994) [in Japanese].

3. J. Matsuo, D. Takeuchi, N.Toyoda and I. Yamada, "Nano space fabrication technology by cluster ion beam", Abstracts of Japan MRS Symposium, December 8th, 1995, Kanagawa Science Park.

4. A. Yoshida, M. Deguchi, T. Hirao, J. Matsuo, N.Toyoda, T. Yamaguchi, G. H. Takaoka and I. Yamada, "Atomic Level Smoothing of CVD Diamond Films by Gas Cluster Ion Beam Etching", Abstracts of E-MRS 1995 Spring Meeting, Abstract No. C-J.III/P10, May 22nd-26th, 1995, Strasbourg, France.

5. N.Toyoda, H. Kitani, J. Matsuo and I. Yamada, "Etching by Reactive Cluster Ion Beams", Papers of the Institute of Electronics, Information and Communication Engineers of Japan, Vol. 95, No. 400, pp.69 (1995) [in Japanese].

6. D. Takeuchi, N.Toyoda, N. Shimada, J. Matsuo and I. Yamada, "Shallow junction formation by polyatomic cluster ion implantation", Papers of the Institute of Electronics, Information and Communication Engineers of Japan, Vol. 95, No. 400, pp.83 (1995) [in Japanese].

7. N.Toyoda, H. Kitani, J. Matsuo and I. Yamada, "Smoothing of SiC Surface by Gas Cluster Ion Beams", Papers of the Institute of Electronics, Information and Communication Engineers of Japan, Vol. 96, No. 395, pp.95 (1996) [in Japanese].

8. N.Toyoda, H. Kitani, J. Matsuo G. H. Takaoka and I. Yamada, "Fabrication of Nano-structure by Cluster Ion Beams", Proceeding of the 6th Symposium of Intelligent Materials, March 21th, 1997, pp.55. [in Japanese].

9. N.Toyoda, J. Matsuo and I. Yamada, "The sputtering effects of cluster ion beams", AIP conf. Proc. **392**, 483(1997) in Fourteenth International Conference on Application of Accelerators in Research and Industry, Denton, TX, USA.

10. N.Toyoda, J. Matsuo and I. Yamada, "Surface Processing by Gas Cluster Ion Beams", Proceedings of the Eleventh International Conference on Ion Implantation Technology, Austin TX, 808 (1997).

11. N.Toyoda, M. Saito, N. Hagiwara, J. Matsuo and I. Yamada, "Cluster size measurement of large Ar cluster ions with Time of Flight",

Proceedings of the Twelfth International Conference on Ion Implantation Technology, June 1998, Kyoto, to be published.

12. N. Hagiwara, N.Toyoda, J. Matsuo and I. Yamada, "Monte Carlo Simulation of Surface Smoothing Effect by Cluster Ions", Proceedings of the Twelfth International Conference on Ion Implantation Technology, June 1998, Kyoto, to be published.

13. M. Saito, N.Toyoda, N. Hagiwara, J. Matsuo and I. Yamada, "Formation of Complex Clusters in Ar/O_2 Cluster Beams", Proceedings of the Twelfth International Conference on Ion Implantation Technology, June 1998, Kyoto, to be published.

14. I. Yamada, J. Matsuo, N.Toyoda and T. Aoki, "Applications of Cluster Ion Implantation in Microelectronics Devices", Proceeding of the Fifteenth International Conference on Application of Accelerators in Research and Industry, November 1998, Denton, TX, USA, to be published.

15. J. Matsuo, N.Toyoda, M. Saito, T. Aoki, T. Seki and I. Yamada, "Novel Analysis Techniques using Cluster Ion Beams", Proceeding of the Fifteenth International Conference on Application of Accelerators in Research and Industry, November 1998, Denton, TX, USA, to be published.

16. A. Nishiyama, M. Adachi, N.Toyoda, N. Hagiwara, J. Matsuo and I. Yamada, "Surface Smoothing of CVD-Diamond Membrane for X-ray Lithography by Gas Cluster Ion Beam", Proceeding of the Fifteenth International Conference on Application of Accelerators in Research and Industry, November 1998, Denton TX, to be published.

International conference

1. N.Toyoda, H.Kitani, J.Matsuo and I.Yamada,
"Reactive sputtering by SF_6 cluster ion beams"
Materials Synthesis and Modification by Ion and/or Laser Beams Joint Symposium with the 3rd Ion Engineering Conference, Chiba, May 1996.

2. N.Toyoda, H.Kitani, J.Matsuo and I.Yamada,
   "The sputtering effects of cluster ion beams"
   The 15th International Conference on the Application of Accelerators In Research and Industry, Denton TX, Nov. 1996.

3. N.Toyoda, H.Kitani, J.Matsuo and I.Yamada,
   "Etching products of Si with SF_6 cluster ion beams"
   Symposium H of the 4th IUMRS International Conference in Asia, Chiba, Sep. 1997.

4. N.Toyoda, M.Saito, N.Hagiwara, J.Matsuo and I.Yamada,
   "Cluster size measurement of large Ar cluster ions with Time of Flight"
   The 12th International Conference on Ion Implantation Technology, Kyoto, June 1998.

5. N.Toyoda, N.Hagiwara, J.Matsuo and I.Yamada,
   "Surface treatment of diamond films with Ar and O_2 clsuter ion beams"
   The 11th International Conference on Ion Beam Modification of Materials, Amsterdam, the Netherlands, Aug. 1998.

Awards

1. Young scientist award in Materials Synthesis and Modification by Ion and/or Laser Beams Joint Symposium with the 3rd Ion Engineering Conference, Chiba, May 1996.

2. Student award in 12th International Conference on Ion Implantation Technology, Kyoto, June 1998.

3. Best poster award in 12th International Conference on Ion Implantation Technology, Kyoto, June 1998.